# Joint inversion of receiver functions and surface wave dispersion to resolve the depth dependent shear wave velocity structure of the Botswana crust

Sietse Vos

June 2023

**Abstract**

In this study, I jointly inverted receiver functions with surface wave dispersion data to resolve the one-dimensional shear wave velocity structure below the seismic stations of the Botswana Seismic Network. This was done to improve our understanding of the Precambrian crust of Botswana. A joint inversion allows for better constraints on the velocity structure than either data set alone could and was done using a trans-dimensional Bayesian approach. The one-dimensional models showed four main features. Many models showed evidence for a low velocity sedimentary layer overlying the crystalline basement. I also often found a well resolved discontinuity at around 11 kilometers depth. I have interpreted this discontinuity as the Conrad discontinuity marking the transition from a felsic upper crust to an intermediate middle crust. At a depth of approximately 35 kilometers most models show a discontinuity where the shear wave velocity jumps to a higher value of between the 4.2 km/s and 4.5 km/s. This high velocity layer is interpreted as the consequence of mafic underplating during one of the magmatic events that affected southern Africa. I have interpreted the Moho where the shear wave velocity exceeds 4.2 km/s. In Botswana, the crustal thickness varies quite strongly between 33 and 52 kilometers. The thin crust in north- northeast Botswana is probably related to recent rifting in the Okavango Rift Zone and the thick crust near the boundary between the Zimbabwe craton and the Magondi belt is probably related to intrusion of the Okavango dyke swarm.

## 1 Introduction

Botswana is geologically a rather diverse region. The Precambrian basement of the country is characterized by an amalgamation of Archean cratons and Proterozoic orogenic belts (Begg et al., 2009). This makes this region interesting to study to get a better understanding of how tectonics worked when the Earth was still relatively young. It can give us more insight in potential differences in tectonics between the Archean and the Proterozoic as is argued by Durrheim and Mooney (1994). Unfortunately, investigating the Precambrian basement is difficult as most of the region is covered by the thick layer of Karoo sediments from the Kalahari desert (Singletary et al., 2003). This makes geophysical methods the primary way of studying the Precambrian basement. In this study, a seismological approach has been chosen. A large number of studies have been done on the crust of Botswana using seismology. For example: Adams and Nyblade (2011), Fadel et al. (2020) and Malory et al. (2022) used surface wave data to investigate the shear wave velocity structure of the crust and/or upper mantle. Fadel et al. (2018) used receiver functions to resolve crustal thicknesses and Vp/Vs ratios at the stations of the Botswana Seismic Network (Botswana Geoscience Institute, 2001). Kgaswane et al. (2009) jointly inverted both data types to create one-dimensional shear wave velocity models below stations of the Africa Array, the Global Seismic Network, the South Africa National Seismic Network, the Southern Africa Seismic Experiment and the Kimberley array. Here, I investigate the crustal structure of Botswana at 21 seismic stations across Botswana by using a joint inversion of receiver functions and surface wave dispersion. This was done with a trans-dimensional Bayesian approach which allows to make estimates of the uncertainties in the model (Bodin et al., 2012). The advantage of using a joint inversion is that it allows to better constrain the velocity structure than either data type alone could. The used stations are from the Botswana Seismic Network (Botswana Geoscience Institute, 2001). This is a nationwide network of 21 seismometers distributed approximately equally across the country (figure 1). This network was installed between 2013 and 2015 (Utrecht-University, 2017). The network was transferred to the Botswana Geoscience Institute in 2018. The goal of this study is to create one-dimensional shear wave velocity models of the Botswana crust in order to enhance our understanding of the tectonics in the region. I hope to improve on the study done by Fadel et al. (2018), who used receiver functions from the same network to create a nationwide crustal thickness and Vp/Vs model.

In the following section, I give an overview of the different tectonic terrains in Botswana. In the subsequent sections I explain the utilized method after which the inversion results are presented and discussed.

## 2 Tectonic setting

Botswana can be divided in several different tectonic terrains of varying age, ranging from Archean to Phanerozoic. The map in figure 1 shows the major tectonic units of the Precambrian basement in the country. This map was based on the research by Chisenga et al. (2020), who mapped the terrain boundaries based on aeromagnetic and gravity data. Alongside the interpretation of the tectonic units, the location of the 21 stations that were used in this study are also plotted on the map as black triangles.

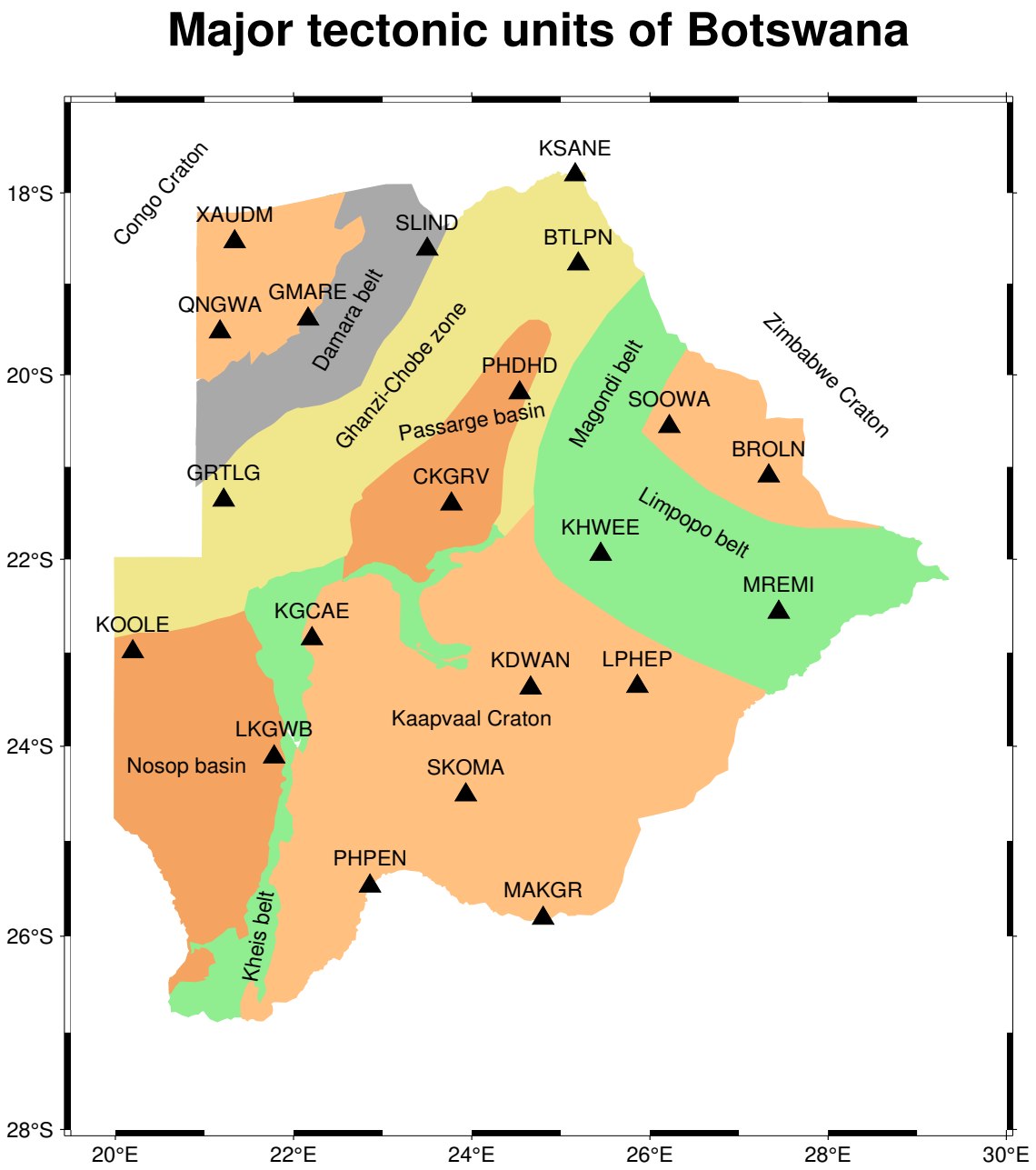


Figure 1: Tectonic overview map of Botswana. This map is based on the results of Chisenga et al. (2020). On the map, the Kaapvaal, Zimbabwe and Congo cratons are colored light orange. The Limpopo belt, Magondi belt, Xade complex, Okwa block and Kheis belt are indicated in green. The Nosop and Passarge basins are indicated in brown. The Ghanzi-Chobe zone is indicated in khaki and the Damara belt in gray.

## 2.1 Archean cratons and Paleoproterozoic Limpopo belt

The southern part of Botswana holds the northern part of the Kaapvaal craton. In Botswana, most of this craton is covered by sediments, except in the very south where station MAKGR is located. Just south of the Botswana border, there are two major intrusions: the Bushveld and Ventersdorp complexes (Hatton, 1995) and on the southern border of Botswana the Molopo farm intrusion (Prendergast, 2012) is located near station PHPEN. The Kaapvaal craton is one of the oldest continental crustal fragments on Earth (Jacobs et al., 2008). This terrain formed from about 3.5-2.5 Ga in the Archean by the amalgamation of different distinct terrains as well as from magmatic events and accretion (Jacobs et al., 2008). A good overview of the formation of the Kaapvaal craton is given by de Wit et al. (1992). They argue that the initial Archean shield formed due to stacking of buoyant, MgO- and water-rich oceanic crust. This stacking induced subsidence due to loading and possibly melting of the lower crust generating large volumes of Trondhjemite-Tonalite melts being the source of the Granite-Greenstone belts found in the craton. After the stabilization of the shield around 3.1 Ga the craton experienced a period of extension which allowed for the deposition of volcanic and sedimentary rocks (de Wit et al., 1992). In the Paleoproterozoic, the Kaapvaal craton collided with the Zimbabwe craton and the Limpopo belt that now together form the Kalahari craton (de Wit et al., 1992; Khoza, Jones, Muller, Evans, Webb, et al., 2013; Kroener et al., 2018).

The Zimbabwe craton is located in the northeastern part of Botswana. The Zimbabwe craton is part of the Archean nucleus of the Kalahari craton. Kampunzu et al. (2003) and Zhai et al. (2006) show that, based on geochemical data, there is evidence for the previous existence of an active margin along the southwestern edge of the craton. Along this active margin, an oceanic part of the Limpopo belt could have subducted below the older Zimbabwe craton. It is important to note that this part of the Zimbabwe craton is crosscut by the Karoo age Okavango dyke swarm (Chisenga et al., 2020). This potentially strongly influenced the structure of the craton. Magmatic underplating can thicken and intrude the crust with mafic mantle material (Thybo and Artemieva, 2013).

The Limpopo is located to the southwest of the Zimbabwe craton in eastern Botswana and sutures together the Zimbabwe craton with the Kaapvaal craton. This belt consists of high grade metamorphic rocks and has experienced multiple large tectonic events (Kroener et al., 2018), although there is no consensus (yet) on the exact tectonic history of this belt. Several different models are proposed. Khoza, Jones, Muller, Evans, Webb, et al. (2013) proposed a model where the Limpopo belt is the result from convergence between the Kaapvaal and Zimbabwe cratons. The Limpopo belt would then have formed from events that are related to subduction and continental collision followed by a period of transpression in a time from approximately 2.7 Ga until 1.9 Ga . They inferred this model based on magnetotelluric data with previous metamorphic studies. However, others have proposed that the Limpopo belt was an amalgamation of several different initially unrelated separate terrains (Khoza, Jones, Muller, Evans, Webb, et al., 2013).

Although the location of the southeastern boundary of the Congo craton is still disputed. Khoza, Jones, Muller, Evans, Miensopust, et al. (2013) and Fadel et al. (2018) argue that the southern boundary of the Congo craton extends into north Botswana beneath the Damara belt shown figure 1.

## 2.2 Paleo- and Mesoproterozoic belts

From the south to the north of Botswana, the Kheis-Okwa-Magondi belt is located. These blocks separate the Kalahari craton (which consists of the Zimbabwe and Kaapvaal cratons and the Limpopo belt) from the rest of the country. This Paleoproterozoic composite belt consists of the Kheis belt in the south, the Okwa block and Xade complex in central Botswana and the Magondi belt in the northeast of Botswana (Fadel et al., 2018). Towards the west, these are bounded by the Kalahari Suture Zone (Haddon, 2005). The Kheis belt is a poorly exposed Paleoproterozoic belt that separates the Kaapvaal craton from the Rehoboth province. From the limited exposures it has been found that this is an east-vergent fold and thrust belt that has been thrust onto the Archean Kaapvaal craton (Jacobs et al., 2008). The Okwa block and the Xade complex are completely covered with Kalahari sediments but can be traced in the subsurface by their high magnetic signature (Chisenga et al., 2020).

In northern Botswana, between the Zimbabwe craton and the Ghanzi-Chobe zone, the Magondi belt is located. This Paleoproterozoic belt formed during the Magondi orogeny (Treloar, 1988). The geochronological data that are available indicate that this belt formed between 2.0 and 1.8 Ga in the Proterozoic (Majaule et al., 2001; Treloar, 1988). The southern part of the Magondi belt (the Botswana part) is dominated by thin skinned tectonics and relatively low grade (greenschist) metamorphism and is overlain by mostly Karoo age (180 Ma) sediments in Botswana (Treloar, 1988).

### 2.3 Meso- and Neoproterozoic belts

In the northwest of the country, the Ghanzi-Chobe zone and the Damara belt are located. The Ghanzi-Chobe zone is a Meso- Neoproterozoic region that is characterised by sedimentary and volcanic rocks (Modie, 2000). This belt formed as a consequence of rifting in the Mesoproterozoic due to continental collision in the Namaque-Natal mobile belt approximately 1106 Ma (Modie, 2000). This event triggered volcanism that formed the Kgwebe formation and basin formation that allowed the sedimentary deposits to form. Later, during the Pan-African orogeny (650 Ma), the fold and thrust belt formed that is now recognized as the Ghanzi-Chobe zone (Modie, 2000). The Ghanzi-Chobe zone is crosscut by the Karoo age Okavango dyke swarm and the incipient Okavango Rift Zone. The Ghanzi-Chobe zone also holds the deep Passarge basin (Chisenga et al., 2020).

The Damara belt is a Neoproterozoic belt that formed during the Pan-Africa orogeny and encompasses several distinct lithologies (Key and Ayres, 2000). The area is characterized by elongated, southwest-northeast striking bands of meta-igneous and metasedimentary rocks (Chisenga et al., 2020; Singletary et al., 2003). The northwestern part of the Damara belt is possibly underlain by an extension of the Congo craton (Fadel et al., 2018; Khoza, Jones, Muller, Evans, Miensopust, et al., 2013) as is also shown in figure 1.

Botswana also has two deep sedimentary basins: the Passarge basin in central Botswana and the Nosop basin in the southwest. In some locations, these basins are up to 15 kilometers deep (Pretorius, 1984).

### 2.4 Okavango Rift Zone

In the northern part of the country the Okavango Rift Zone (ORZ) is located. This is an incipient rift system and an extension of the East African Rift (Fadel et al., 2020; Pastier et al., 2017; Yu, Gao, et al., 2015). Fadel et al. (2020) show that a low velocity zone below the crust has a connection with a low velocity zone in the upper mantle that is associated with the East African Rift. They also argue that this low velocity zone connects to a low velocity zone in central Botswana, which might have been responsible for the 2017 earthquake due to upward migration of fluids (Paulssen et al., 2022).

## 3 Receiver functions and phase velocity data

The 21 seismic stations in Botswana shown in figure 1 have been used before for a surface wave study by Fadel et al. (2020). Their study gives a smoothed out image of the shear wave velocity of the Botswana crust and upper mantle (up to 200 kilometers depth). In this study, I add receiver functions to these data and jointly invert them to create one-dimensional shear wave velocity models of the crust below each of these stations. Since receiver functions are sensitive to seismic discontinuities this allows to add more detail in the structure.

In the following section, I first explain receiver functions and surface wave dispersion. After this, the trans-dimensional Bayesian inversion procedure is discussed.

### 3.1 Receiver functions

A plane P-wave incident on a seismic discontinuity is partially converted to an SV-wave. Since S-waves are generally slower than P-waves, the two signals and subsequent reverberations are recorded at later times. The amplitude and the timing of the different phases depend on the angle of incidence and thus on the slowness of the ray. These signals contain information about discontinuity depth and about Vp/Vs. Unfortunately, this information is often hidden by source effects and the effects of the propagation through the mantle. This means that we have to extract the receiver functions from the raw seismograms. Figure 2 illustrates the ray theoretical arrivals for a plane incident P-wave in a simple crust over half space model. This figure illustrates the arrivals in the ZRT coordinate system; this coordinate system has its horizontal axes parallel (R-axis) and perpendicular (T-axis) to the horizontal components of the travelling ray. The vertical (Z-axis) component is perpendicular to the Earth's surface. In this coordinate system, no SH-waves are generated if the layers are horizontal, homogeneous and isotropic.

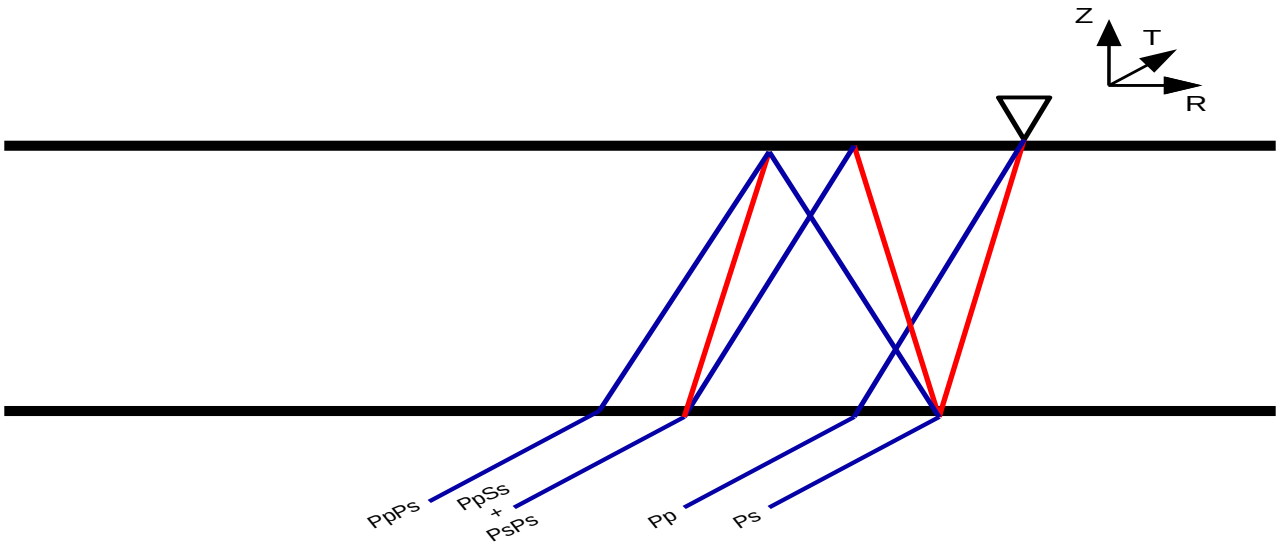


Figure 2: Cartoon of ray theoretical arrivals for a plane incident P-wave in a simple single layer crust model. Blue rays represent P-waves and red rays represent S-waves. The coordinate system shows the radial, transverse and vertical directions. The different phases are the direct P-wave (Pp), the first P- to S-wave conversion (Ps) and the PsPs, PpSs and PpPs reverberations.

The ground response can be written as a convolution between the source-time function, the instrument response and the near receiver Earth structure response(Langston, 1979; Owens et al., 1984).

$$D_Z(t) = S(t) * I(t) * E_Z(t) \tag{1}$$
$$D_R(t) = S(t) * I(t) * E_R(t) \tag{2}$$
$$D_T(t) = S(t) * I(t) * E_T(t) \tag{3}$$

Where $S(t)$ is the source time function, $I(t)$ is the instrument impulse response and $E_Z(t)$, $E_R(t)$, $E_T(t)$ are the vertical, radial and transverse near receiver Earth responses. It is observed that the vertical near receiver Earth response of steeply incident P-waves mostly is a first P-arrival with only minor later arrivals (Owens et al., 1984). This implies that $E_Z(t) \approx \delta(t)$ and means that we can rewrite this component as:

$$D_Z(t) \approx S(t) * I(t) \tag{4}$$

We can now see that it is possible to extract the two horizontal receiver functions by deconvolving the vertical component from the horizontal components. By doing this in the frequency domain, this process turns into relatively straightforward spectral division as shown in equations 5 and 6.

$$RF_R(\omega) = \frac{D_R(\omega)}{D_Z(\omega)} \tag{5}$$
$$RF_T(\omega) = \frac{D_T(\omega)}{D_Z(\omega)} \tag{6}$$

$RF_R(\omega)$ and $RF_T(\omega)$ are the radial and transverse receiver functions in the frequency domain, $D_R(\omega)$ and $D_T(\omega)$ are radial and transverse ground responses in the frequency domain and $D_Z(\omega)$ is the vertical ground response in the frequency domain. Unfortunately, deconvolution can be unstable and therefore needs to be stabilized.

In this study I use the method of Langston (1979). This method uses a water level stabilized deconvolution that fills up any spectral troughs up to a percentage of the maximum amplitude on the vertical component and applies a Gaussian filter to remove any high frequency components that were not present in the original signal. The used equation is slightly

altered from the original in Langston (1979) as I added a normalization factor $q$ that ensures that the impulse response of the Gaussian always has a peak amplitude of 1. These equations look as follows:

$$RF_R(\omega) = \frac{D_R(\omega)D_Z^*(\omega)}{max[D_Z(\omega)D_Z^*(\omega), \quad c \times max(D_Z(\omega)D_Z^*(\omega))]} q e^{-\frac{\omega^2}{4a^2}} \tag{7}$$

$$RF_T(\omega) = \frac{D_T(\omega)D_Z^*(\omega)}{max[D_Z(\omega)D_Z^*(\omega), \quad c \times max(D_Z(\omega)D_Z^*(\omega))]} q e^{-\frac{\omega^2}{4a^2}} \tag{8}$$

$RF_R(\omega)$ and $RF_T(\omega)$ are the frequency domain versions of the radial and transverse receiver functions, of which the latter one should be 0. $D_Z(\omega)$, $D_R(\omega)$ and $D_T(\omega)$ are the frequency domain versions of the ground response in the vertical, radial and transverse directions. $D_Z^*(\omega)$ is the complex conjugate of the vertical component. $c$ is the waterlevel (0.001 in this study), $q$ is the normalization factor and $a$ is the width of the Gaussian filter (0.2 Hz in this study).

After calculation, the receiver functions were subjected to two quality checks. First, the signal-to-noise ratio was calculated. This was done by using the same definition as Fadel et al. (2018) did where the signal-to-noise ratio was simply defined as the ratio between the maximum amplitude on the radial receiver function and the maximum amplitude on the transverse receiver function.

$$SNR = \frac{max(RF_R(t))}{max(RF_T(t))} \tag{9}$$

Only receiver functions with a signal-to-noise ratio larger than 3.0 were accepted. After this process, the remaining receiver functions were inspected visually. Receiver functions with weak or deformed P-wave arrivals or receiver functions with large amplitudes on the transverse component or before the first P-arrival are discarded.

To improve the signal-to-noise ratio receiver functions were binned and stacked based on slowness. The slowness binning was done because the timing and amplitude of the phases in a receiver function depend on the slowness of the ray. To determine the bin size, two synthetic receiver functions with different slownesses were generated and stacked. The difference between the stacked receiver function and the generated receiver functions were calculated with a simple $L_2$-norm criterion. The bin size was chosen such that the maximum difference between the stack and the synthetic receiver functions was approximately 0.05, this resulted in a bin size of 0.4s/°. Because structure can vary as a function of back azimuth it sometimes was necessary to bin based on back azimuth as well. This was only done when necessary. Whether it was necessary or not was determined visually by looking at the variation in receiver functions as a function of the back azimuth. The amount of receiver functions in a single stack varied between 1 and 8.

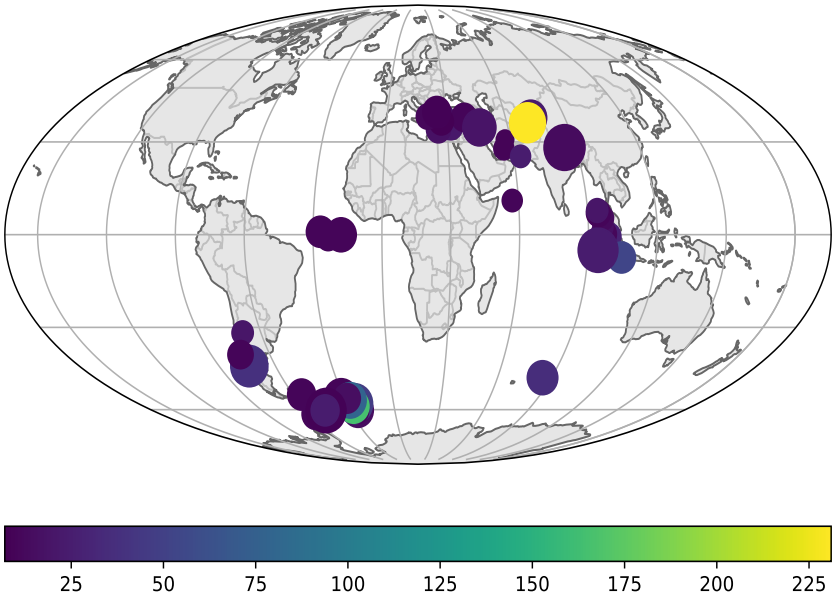


Figure 3: World map showing the distribution of events used for the receiver functions. The color indicates depth in kilometer and the size indicates magnitude.

In this study, I used teleseismic earthquakes to obtain the receiver functions. I used events from between 01-01-2013 and 25-08-2022, with an epicentral distance between 40° and 80° and a magnitude between 6.0 and 8.0. Figure 3 shows the distribution of the events and in section 5 tables of the used events per model are given. Most events originate either from the northeast (back azimuth between approximately 0° and 90°) or from the southwest (back azimuth between approximately 200° and 240°). Before calculating receiver functions, the raw seismograms were first windowed between -5 seconds and 35 seconds with respect to the onset of the first P-wave. The data were decimated to a sampling rate of 5 Hz and bandpass filtered with corner frequencies of 0.031 Hz and 2.0 Hz (80% of the signal length and 80% of the Nyquist frequency). The data were demeaned, detrended and tapered with a Hann window. All processing was done with the ObsPy (Beyreuther et al., 2010), rf ("rf: Receiver function calculation in seismology", 2020) and SciPy packages. Lastly, the data were rotated to the ZRT coordinate system, which is the same coordinate system as is shown in figure 2.

Figure 4 shows the receiver functions that were selected for station KHWEE in the Limpopo belt. The receiver functions are fairly well correlated with each other. There are two distinct groups of receiver functions. One with a back azimuth of approximately 10° and one with a back azimuth of approximately 210°.

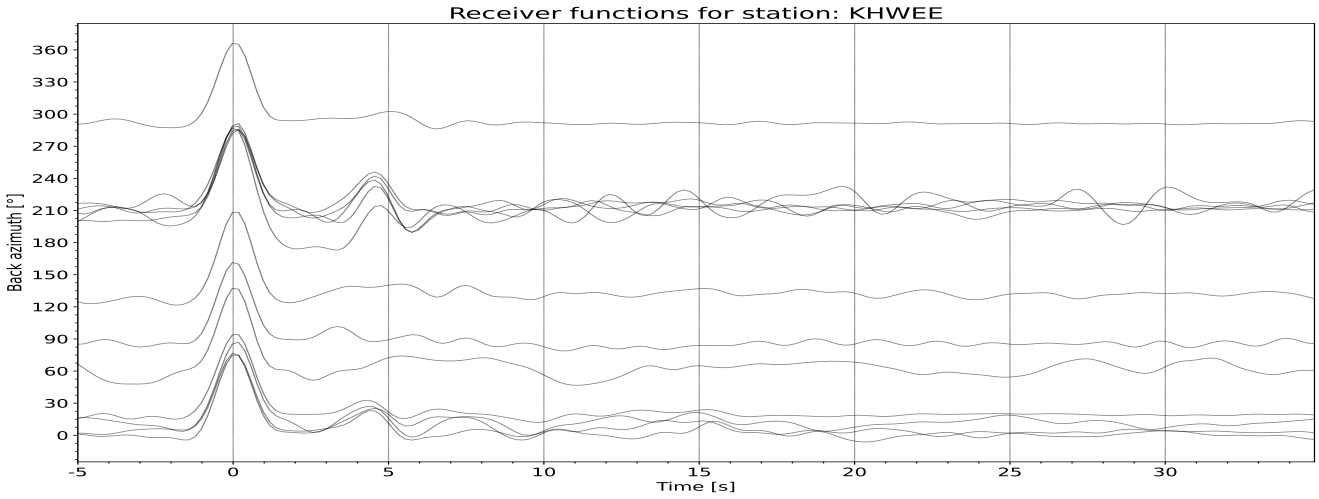


Figure 4: Receiver functions at station KHWEE as a function of back azimuth. Especially the receiver functions with a back azimuth of about 210° show a prominent peak at about 4 seconds after the first arrival.

## 3.2 Surface wave dispersion

Wave dispersion is a consequence of the fact that the depth sensitivity of a surface wave depends on its frequency. Lower frequency waves are sensitive to larger depths and thus in general faster than higher frequency waves. As a consequence, different frequency surface waves have different travel times through the medium. By measuring the difference in travel time of surface waves at different frequencies between two seismic stations it is possible to estimate the wave velocity between two stations as a function of frequency.

All the Rayleigh wave dispersion data in this study are from Fadel et al. (2020). This study combined ambient noise tomography with Helmholtz tomography. The phase- and group velocity maps are defined on a grid with a 1° by 1° cell size. For the joint inversion, the Rayleigh wave phase velocity curve that is closest to the station where the receiver functions were measured were used. Figure 5 shows the phase velocity curve that was used (with the receiver functions) at station KHWEE. The phase velocities from periods between 3-35 seconds were computed using ambient noise tomography and phase velocities from periods between 30-120 seconds were computed with Helmholtz tomography using teleseismic earthquakes (Fadel et al., 2020).

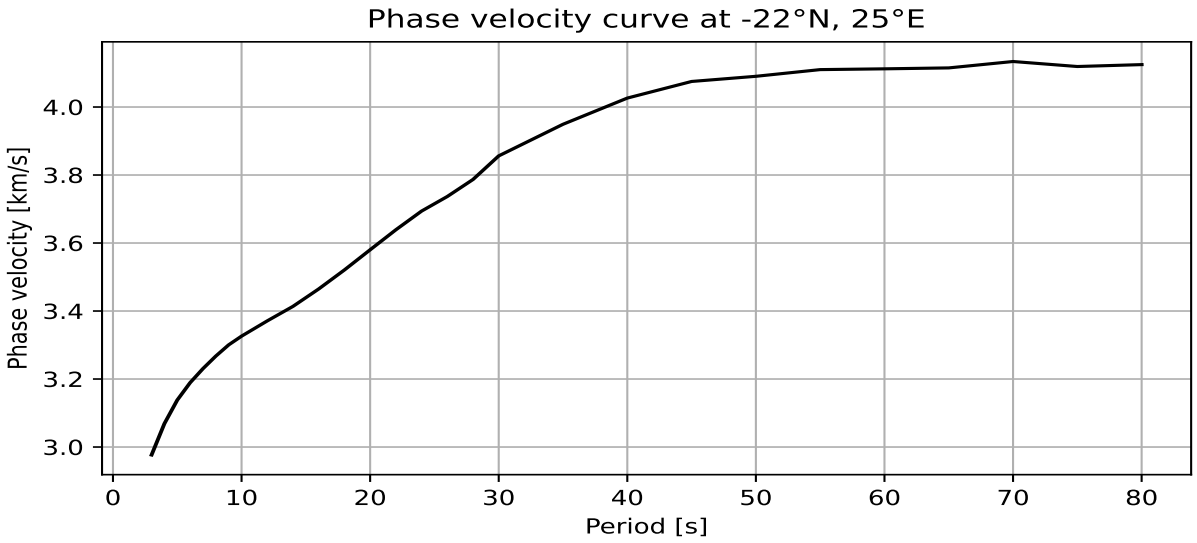


Figure 5: Rayleigh wave phase velocity curve from Fadel et al. (2020) close to station KHWEE.

# 4 Inversion method

In order to jointly invert the receiver functions and surface waves, a Bayesian, trans-dimensional approach to the inverse problem is used (Bodin et al., 2012). Using a Bayesian framework means that the results can be represented as an ensemble of Earth models within a probability distribution. The advantage of this approach is that it allows for a relatively straightforward way to quantify the model uncertainty. The algorithm allows to solve for the layer velocities, the amount of layers, the Vp/Vs ratio and the noise parameters.

## 4.1 Bayes theorem

In this context Bayes theorem can be written as (Bodin et al., 2012):

$$p(\mathbf{m}|\mathbf{d}) \propto p(\mathbf{m})p(\mathbf{d}|\mathbf{m}) \tag{10}$$

In this equation $p(\mathbf{m}|\mathbf{d})$ is the posterior probability, i.e. the probability that we obtain model $\mathbf{m}$ with given data $\mathbf{d}$. $p(\mathbf{m})$ is the prior distribution, which is what we (think we) know about the structure of the Earth. $p(\mathbf{d}|\mathbf{m})$ is the likelihood, i.e. the probability that we observe data $\mathbf{d}$ given a model $\mathbf{m}$. The likelihood is given by the following equation (Bodin et al., 2012):

$$p(\mathbf{d_{obs}}|\mathbf{m}) = \frac{1}{\sqrt{(2\pi)^n|\mathbf{C}_e|}} e^{\frac{-\Phi(\mathbf{m})}{2}} \tag{11}$$

In equation 11 $\Phi(\mathbf{m})$ is the Mahalanobis distance (Mahalanobis, 1936), which is given by:

$$\Phi(\mathbf{m}) = (g(\mathbf{m}) - \mathbf{d}_{obs})^T \mathbf{C}_e^{-1} (g(\mathbf{m}) - \mathbf{d}_{obs}) \tag{12}$$

With $g(\mathbf{m})$ being the synthetic data vector, $\mathbf{d}_{obs}$ being the observed data vector and $\mathbf{C}_e^{-1}$ is the inverse of the covariance matrix. This expression is similar to the expression of the euclidean distance between two vectors, but this equation also takes the noise correlation into account by splitting $\mathbf{C}_e$ in a variance and correlation part as is shown in equation 13. The likelihood is used to compute the acceptance probability of a model. This is explained in Gallagher et al. (2009) and in the appendix of Bodin et al. (2012).

## 4.2 Parameterization

The velocity depth model is parameterized by means of a one dimensional voronoi representation. The amount of voronoi nuclei is variable, therefore, the amount of crustal layers and thus the model dimension is variable. Each voronoi nucleus is defined by a depth and a velocity value and discontinuities are placed equidistant between two nuclei (Bodin et al., 2012).

Vp/Vs is parameterized as a constant value over the entire domain. This means that the Vp/Vs that is solved for is the average Vp/Vs value of the entire model. The disadvantage of this approach is that differences between layers are potentially large (especially if there are low Vs sedimentary layers present) and one average value might not be representative of the range of Vp/Vs values.

Noise is parameterized by splitting it into a standard deviation and a correlation. This means that the covariance matrix can be written as (Bodin et al., 2012):

$$\mathbf{C}_e = \mathbf{s}^T \mathbf{R} \mathbf{s} \tag{13}$$

In this equation, $\mathbf{C}_e$ is the covariance matrix, $\mathbf{s}$ is the vector of standard deviations and $\mathbf{R}$ is the correlation matrix. If we assume that the noise is constant along the entire data series, this can be rewritten to:

$$\mathbf{C}_e = \sigma^2 \mathbf{R} \tag{14}$$

In this equation $\sigma^2$ is the noise variance. $\mathbf{R}$ is a toeplitz matrix given by:

$$\begin{pmatrix} 1 & c_1 & \dots & c_{n-1} \\ c_1 & 1 & \dots & c_{n-2} \\ \vdots & & \ddots & \\ c_{n-1} & c_{n-2} & \dots & 1 \end{pmatrix} \tag{15}$$

$c_i$ is the correlation between samples that are $i$ samples apart. In this study, it is assumed that the noise correlation for the receiver functions follows a Gaussian distribution. That means that $c_i$ can be written as:

$$c_i = r^{i^2} \tag{16}$$

Where $r$ is the noise correlation between two adjacent samples. In order to calculate the likelihood (equation 11), both the determinant and the inverse of the covariance matrix are required. Because the Gaussian correlation law is used as expressed in equation 16, there are no analytical expressions for both the inverse and the determinant of $\mathbf{C}_e$ (Bodin et al., 2012). For that reason, $r$ is estimated before the inversion based on the Gaussian width and the sampling rate of the receiver function and kept at a constant value of 0.96 during the inversion. $r$ for the surface waves was set to 0. This is justified by the fact that surface wave dispersion measurements are based on separate measurements at different frequencies. These are in theory uncorrelated so the noise correlation should be 0 (Bodin et al., 2012).

## 4.3 Model-space sampling

The amount of layers is unknown and therefore, the dimension of the model is unknown beforehand. In order to effectively sample the parameter space, a reversible jump Markov chain Monte Carlo (rj-McMC) algorithm is used (Bodin et al., 2012). With this algorithm, this initial model is chosen randomly within the boundaries of the prior distribution.

Every iteration, the model is perturbed according to a proposal distribution that was defined beforehand. This model is used to calculate the response of an isotropic stack of horizontal layers. This response is used to calculate the synthetic receiver functions and phase velocity, which in turn is used to compute the likelihood with equation 11. The likelihood, prior distribution and proposal distribution are used to compute the acceptance ratios (Bodin et al., 2012) which determines whether the model in the chain is accepted or not. If the model is accepted, a new iteration starts with the perturbed model as a starting point. If the model is rejected, a new iteration starts with the old model as a starting point. This process goes on until a set amount of iterations is reached (1.8 or 2.3 million in this study). All of the accepted models together form the Markov chain. In this study, I used 50 Markov chains as this already resulted in statistically significant results. Increasing the amount of chains would likely not increase the quality of the models but would significantly increase the computational load.

Iteration is carried out in two different phases, a burn-in phase and an exploration phase. All the models from the burn-in phase are discarded. The models from the exploration phase are sub-sampled after the inversion to create the posterior distribution. I used a burn-in to exploration ratio of 2:1 to ensure that the Markov chains have converged while creating the posterior distribution. In this study, chains with a likelihood that deviates more than 5% from the median likelihood are not considered for the calculation of the posterior. Of the remaining chains, 100,000 models are sub-sampled from which the posterior distribution is calculated.

### 4.3.1 Proposal distribution

The proposal distribution determines how the model is perturbed. Each iteration, the parameter to be perturbed is chosen randomly (i.e. velocity of a single voronoi nucleus, depth of a single voronoi nucleus, birth/death of a layer, noise

or Vp/Vs). The chosen parameter is randomly perturbed according to a Gaussian distribution centered at the current value of the parameter. The proposal distributions have the form of (Bodin et al., 2012):

$$q(a_i'|a_i) = \frac{1}{\theta\sqrt{2\pi}} e^{-\frac{(a_i'-a_i)^2}{2\theta^2}} \tag{17}$$

Where $a_i$ is the current model parameter, $a_i'$ is the perturbed model parameter and $\theta$ is the standard deviation. The standard deviations used in this study are given in table 1.

| | |
|---|---|
| **Vs**: | 0.015 km/s |
| **Depth**: | 0.015 km |
| **Layer birth/death**: | 0.015 |
| $\sigma_{\mathbf{RF}}$: | 0.005 $s^{-1}$ |
| $\sigma_{\mathbf{SWD}}$: | 0.005 km/s |
| **Vp/Vs**: | 0.005 |

Table 1: Proposal distribution used in this study. The values in this table are the standard deviations of the Gaussian that defines the proposal distribution.

As the chain progresses through parameter space, the acceptance rate of the models will naturally drop. In order to prevent the chain from getting stuck in a local minimum, the proposal standard deviations can be altered dynamically in order to force the acceptance rate up (Dreiling & Tilmann, 2019). In this study, I set the target acceptance rate between 40-45% (Bodin et al., 2012). However, a minimum standard deviation of 0.001 has been implemented by Dreiling and Tilmann (2019). This was done because the proposal width for the layer birth/death would quickly drop to very small numbers in the order of $10^{-10}$ km/s in order to keep the acceptance rate high. This would cause the model dimension to barely change anymore and potentially result in numerical problems (we need to divide by the standard deviation in equation 17). Therefore, the actual acceptance rate is lower than what is prescribed.

## 4.4 BayHunter

The algorithm described in the previous sections is implemented in python by Dreiling and Tilmann (2019) in the form of the software package BayHunter (GitHub link: https://github.com/jenndrei/BayHunter). As input, the code requires the data and the prior distribution. The prior is shown in table 2

| | |
|---|---|
| **Vs**: | 1 - 5 km/s |
| **Vp/Vs**: | 1.65 - 2.0 |
| **# of layers**: | 1 - 15 |
| $\mathbf{r}_{\mathbf{RF}}$: | 0.96 |
| $\mathbf{r}_{\mathbf{SWD}}$: | 0 |
| $\sigma_{\mathbf{RF}}$: | $10^{-5}$ - 0.05 $s^{-1}$ |
| $\sigma_{\mathbf{SWD}}$: | $10^{-5}$ - 0.1 km/s |

Table 2: Prior distribution used in this study. **Vs** is the shear wave velocity range, **Vp/Vs** is the Vp/Vs range, **# of Layers** represents the amount of layers and **r** and $\sigma$ are the noise parameters with subscript 'RF' for receiver functions and 'SWD' for surface wave dispersion.

For inversions with only one receiver function, the upper limit of $\sigma_{\mathbf{RF}}$ was raised to 0.1. For station SLIND, $\mathbf{r}_{\mathbf{RF}}$ was lowered to 0.93. For some of the stations the Vp/Vs ratio settled on the lower boundary. Lowering this boundary to 1.55 sometimes helped to converge to a value within the boundaries; although for some stations, the model was still settling on the lower boundary. Aside from this fact, Botswana is covered by a thick layer of sand, which potentially has a very high Vp/Vs. This can potentially influence the model results. This was (probably) the reason that we were unable to resolve Vp/Vs for several stations. However, as noted by Dreiling et al. (2020), since the used data types are mostly sensitive to Vs and not so much to Vp, the effect of Vp/Vs to the Vs depth structure should be limited.

I also tried to address this problem by fixing the Vp/Vs in the top layer to a reference value. Unfortunately, this did not have the desired effect on the modelling, therefore, this feature was not used in the final results. Nevertheless, this feature may be useful in future studies where a low shear wave velocity top layer is present.

In the next section, I will show the modeling results and discuss them in the context of crustal structure.

# 5 Results

In this section, I will start by showing the full results of a single inversion for station SKOMA. After this, I discuss the velocity models per station and for each main tectonic terrain in figure 1 discuss the results in the context of the crustal structure of the area. The velocity models were made by creating a single posterior distribution from all inversions simultaneously. This approach is similar to averaging the different inversions. The models from the individual inversions are presented in appendix B.

In these discussions, I focus on three main features in the velocity models; a discontinuity at approximately 10 kilometers depth, one at approximately 35-40 kilometers depth and one at approximately 50 kilometers depth. These discontinuities are placed based on three velocity thresholds. I use 3.8 km/s for the upper discontinuity, this is based on a P-wave velocity increase from 6.1 to 6.7 km/s at the Conrad discontinuity (Abdelwahed et al., 2013) and the assumption of a Poisson upper crust ($Vp/Vs = \sqrt{3}$). Unfortunately, this often resulted in an ambiguous result. The threshold was often crossed multiple times and the threshold is often within one standard deviation from the mean for very large depth ranges. Therefore, this discontinuity was often hand picked at a realistic depth based on visual inspection of the velocity models. For the middle discontinuity, I use a velocity of 4.2 km/s, this is based on the isotropic upper mantle shear wave velocity from PREM (Dziewonski & Anderson, 1981). This discontinuity is therefore interpreted as the Moho. For the final discontinuity, I use a velocity threshold of 4.5 km/s as this is the velocity that is generally exceeded at the deepest discontinuity before stabilizing at approximately 4.6 km/s. The discontinuities were analysed by looking at all the models in the posterior distribution and looking at where the velocity threshold was exceeded.

For each station, I make a comparison to Fadel et al. (2018) and, if applicable, to Kgaswane et al. (2009), Youssof et al. (2013) and Yu, Liu, et al. (2015). Tables with information about the events used for receiver function calculation are given in appendix A.

## 5.1 Kaapvaal craton

### 5.1.1 SKOMA

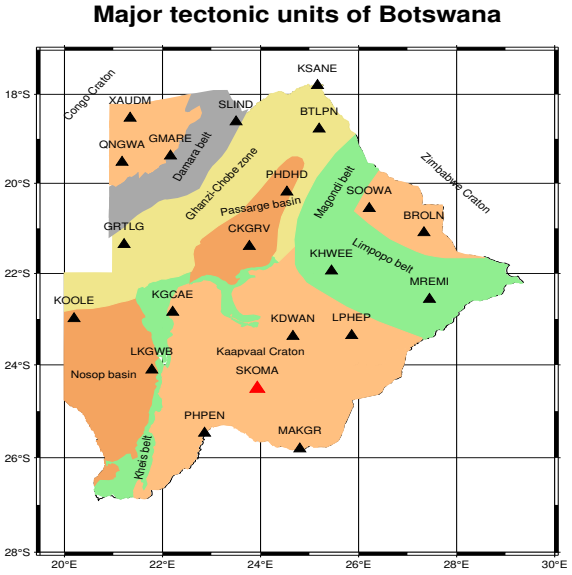


Figure 6: Tectonic map indicating station SKOMA in red.

Station SKOMA is located in the northern Kaapvaal craton. The receiver functions for this station were of good quality and did not vary much with back azimuth. Two different inversions were carried out for this station, one with a receiver function stack with an average slowness of 5.5 $s/°$ with back azimuth of 52.9° (table 3); and one with an average slowness of 7.7 $s/°$ and with back azimuth ranging between 214.8° and 216.6° (table 4). The results are shown in figures 7, 8 and 9 respectively.

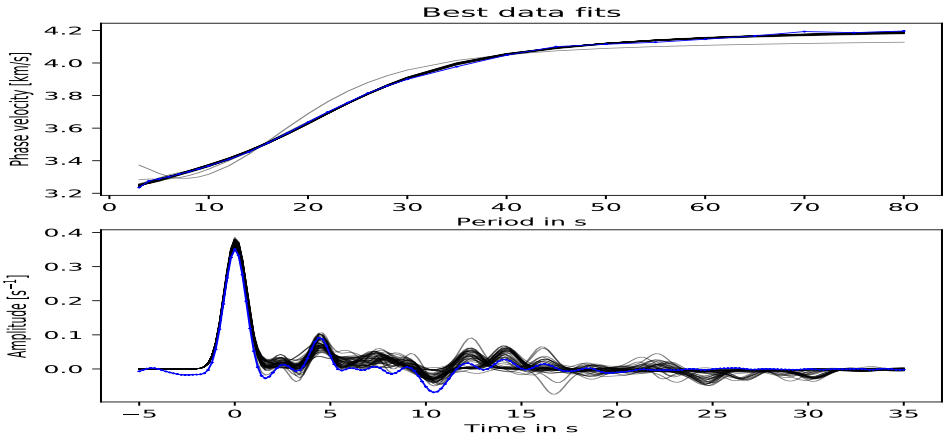


(a) Data fit of the the best fitting model of each Markov chain. The data is given in blue and the models in black. The upper panel gives the phase velocity fit and the lower panel gives the receiver function fit.

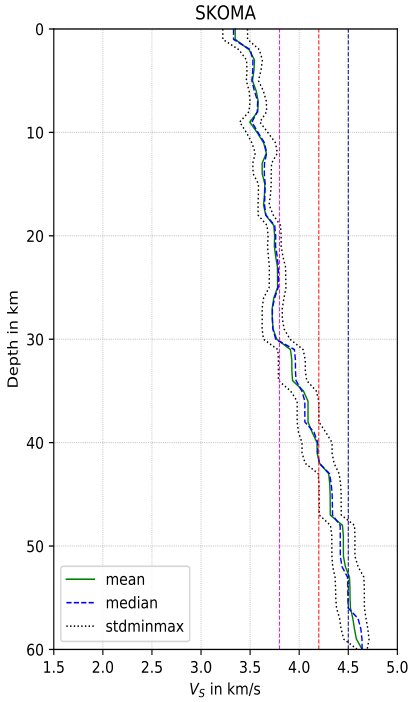


(b) Mean and median velocity models of inversion 1 for station SKOMA. The green line gives the mean velocity, the blue dashed line gives the median velocity and the dotted black lines give the standard deviation of the model.

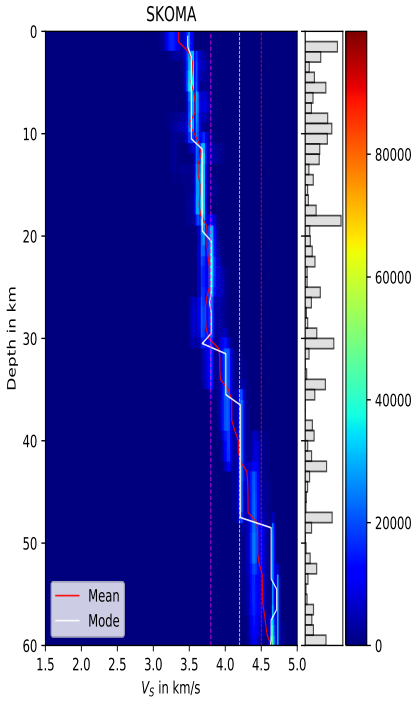


(c) The mode and mean models of one inversion for station SKOMA. The white line gives the mode velocity and the red line gives the mean velocity. The colors indicate the amount of models that predict a velocity at a specific depth and the histogram on the right gives the amount of models that predict an interface at a specific depth.

Figure 7: 1D velocity models of one inversion for station SKOMA, the receiver function is a stack of the events given in table 3 (2 events). Figure 7a shows the data fit, figure 7b shows the mean and median models as well as the standard deviation. Figure 7c shows the mode and mean models in the posterior Vs distribution and the interface depth. The vertical lines in both panels give the 3.8 km/s, 4.2 km/s and 4.5 km/s thresholds.

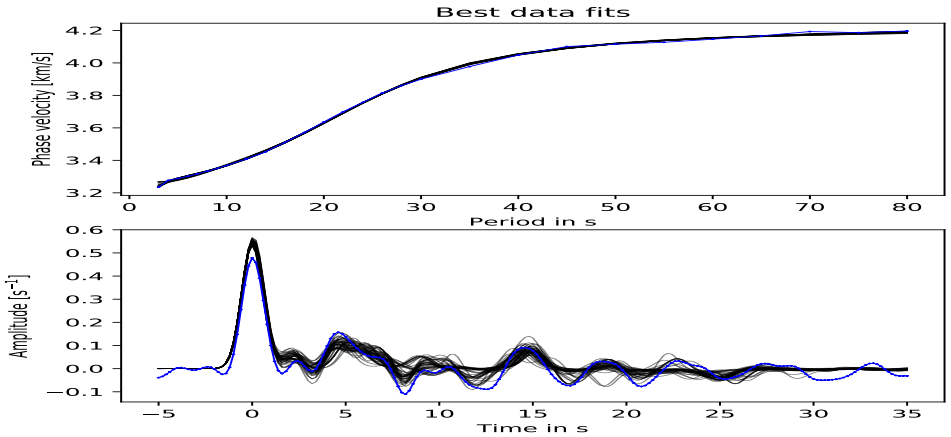


(a) Data fit of the the best fitting model of each Markov chain. The data is given in blue and the models in black. The upper panel gives the phase velocity fit and the lower panel gives the receiver function fit.

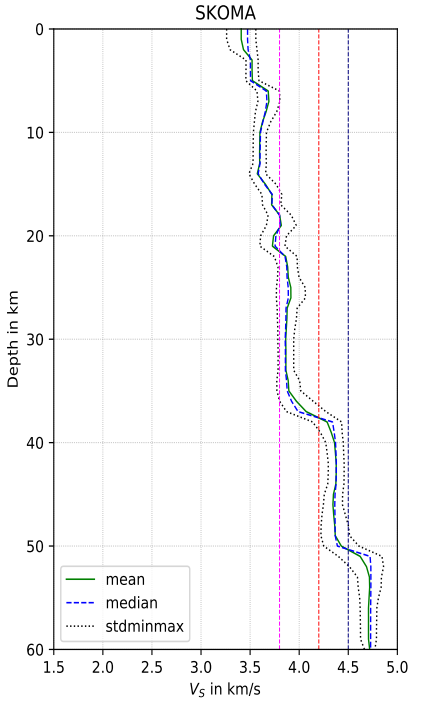


(b) Mean and median velocity models of inversion 1 for station SKOMA. The green line gives the mean velocity, the blue dashed line gives the median velocity and the dotted black lines give the standard deviation of the model.

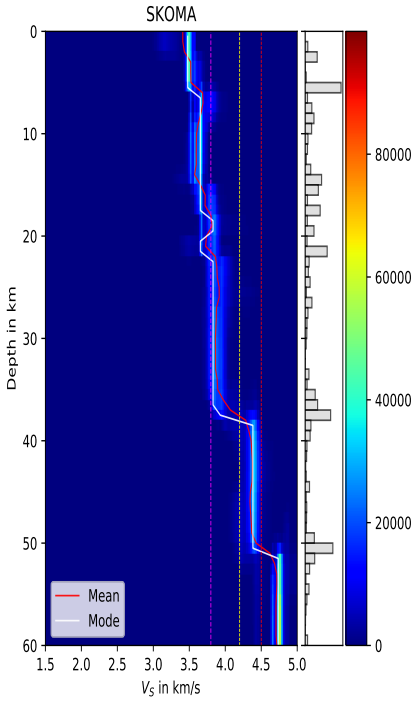


(c) The mode and mean models of one inversion for station SKOMA. The white line gives the mode velocity and the red line gives the mean velocity. The colors indicate the amount of models that predict a velocity at a specific depth and the histogram on the right gives the amount of models that predict an interface at a specific depth.

Figure 8: 1D velocity models of one inversion for station SKOMA, the receiver function is a stack of the events given in table 4 (3 events). Figure 8a shows the data fit, figure 8b shows the mean and median models as well as the standard deviation. Figure 8c shows the mode and mean models in the posterior Vs distribution and the interface depth. The vertical lines in both panels give the 3.8 km/s, 4.2 km/s and 4.5 km/s thresholds.

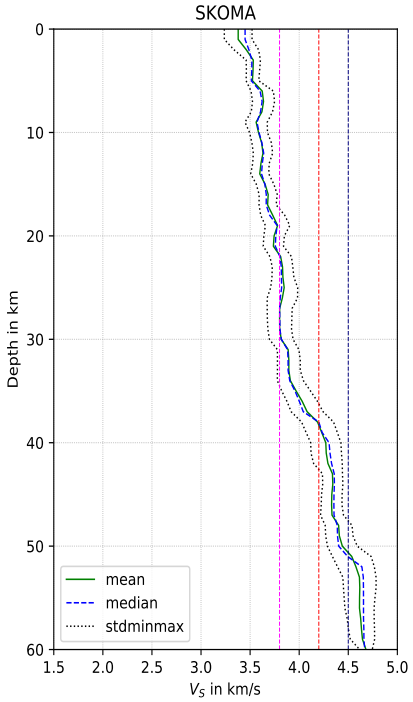


(a) Mean and median velocity models of the combined for station SKOMA. The green line gives the mean velocity, the blue dashed line gives the median velocity and the dotted black lines give the standard deviation of the model.

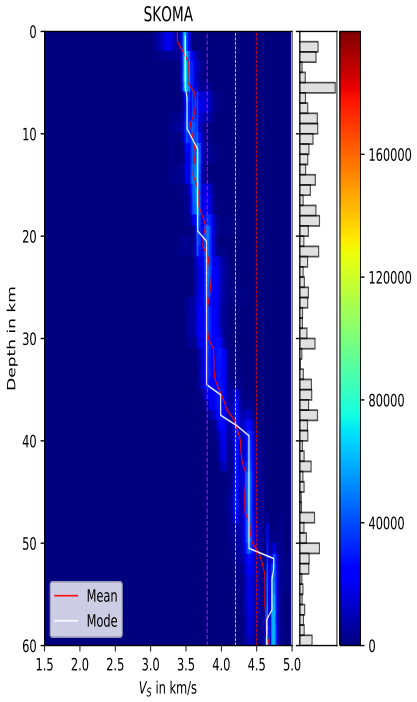


(b) The mode and mean models of the combined inversions for station SKOMA. The white line gives the mode velocity and the red line gives the mean velocity. The colors indicate the amount of models that predict a velocity at a specific depth and the histogram on the right gives the amount of models that predict an interface at a specific depth.

Figure 9: 1D velocity models of the combined inversions for station SKOMA. The left panel shows the mean and median models as well as the standard deviation. The right panel shows the mode and mean models in the posterior Vs distribution and the interface depth. The vertical lines in both panels give the 3.8 km/s, 4.2 km/s and 4.5 km/s thresholds.

Figures 7a and 8a show a very good fit for both the receiver functions and phase velocities. Especially the phase velocities were fitted very well. The receiver function fit was good as well, most features were modeled well, especially earlier in the receiver function. At later times, the receiver function fit becomes worse. This is something that was seen for most of the stations.

The velocity models from figures 7 and 8 look fairly different, nevertheless, the velocity thresholds of 3.8 km/s, 4.2 km/s and 4.5 km/s are exceeded at similar depths in both models. The difference between the two models can be explained by poorly resolved discontinuities in figure 7 making localizing interfaces difficult. This is expressed in the 'messy' histogram from figure 7c. Figure 9 shows the combined effects of both inversions and appears to be a smoothed out version of figure 8.

Figures 8 and 9 show three well defined discontinuities. One at 6 kilometers, one at 37 kilometers and one at 51 kilometers. Based on analysis of both inversions, I found a crustal thickness of around 38 kilometers, which is slightly deeper than what Fadel et al. (2018) found (36 kilometers).

From this point onward, I only show the combined results from the inversions for each station (similar to figure 9). The individual inversion results are shown in appendix B.

### 5.1.2 KGCAE

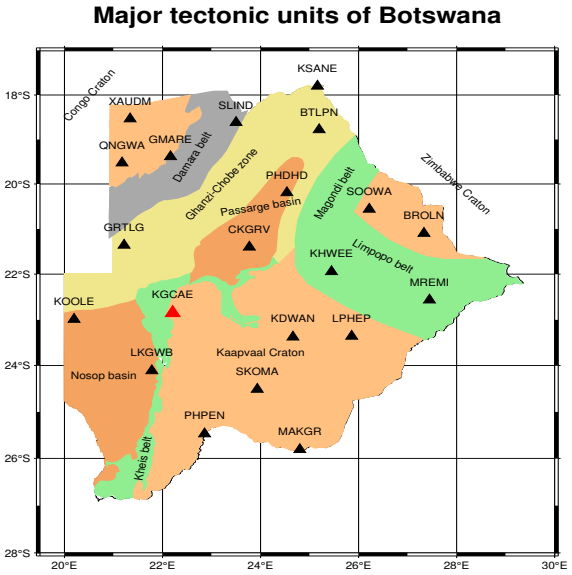


Figure 10: Tectonic map indicating station KGCAE in red.

Station KGCAE is located in the northwestern corner of Kaapvaal craton. The receiver functions for this station were of good quality and did not vary much with back azimuth. Two different inversions were carried out for this stations, one with a receiver function stack with an average slowness of 5.5 $s/^\circ$ with back azimuths ranging between 53.0° and 239.9° (table 5); and one with an average slowness of 7.5 $s/^\circ$ with back azimuths ranging between 133° and 216.4° (table 6). The combined inversion results are shown in figure 11.

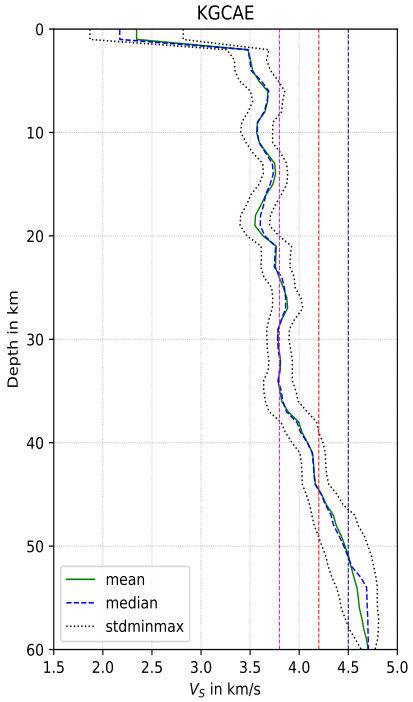


(a) Similar to figure 9a the mean and median velocity models with standard deviation for station KGCAE.

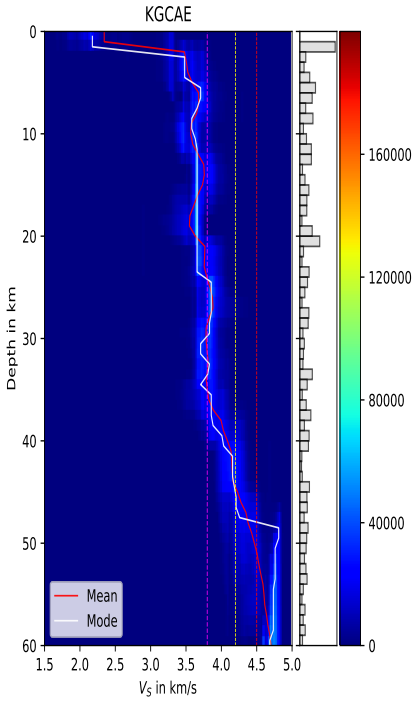


(b) Similar to figure 9b the mean and mode velocity models within the posterior Vs distribution for station KGCAE.

Figure 11: 1D velocity models of the inversions for station KGCAE. The vertical lines in both panels give the 3.8 km/s, 4.2 km/s and 4.5 km/s thresholds. The used events are given in tables 5 and 6 (11 events)

The most defining feature in figure 11 is the low velocity zone in the upper 2 kilometers. This is probably related to the sedimentary overburden that covers most of Botswana. The three discontinuities talked about before are not as well pronounced in these models. But there are still discontinuities visible at approximately 13 kilometers and 38 kilometers.

For this station, I found a crustal thickness of approximately 45 kilometers, this is comparable to the 44 kilometers that Fadel et al. (2018) found.

### 5.1.3 KDWAN

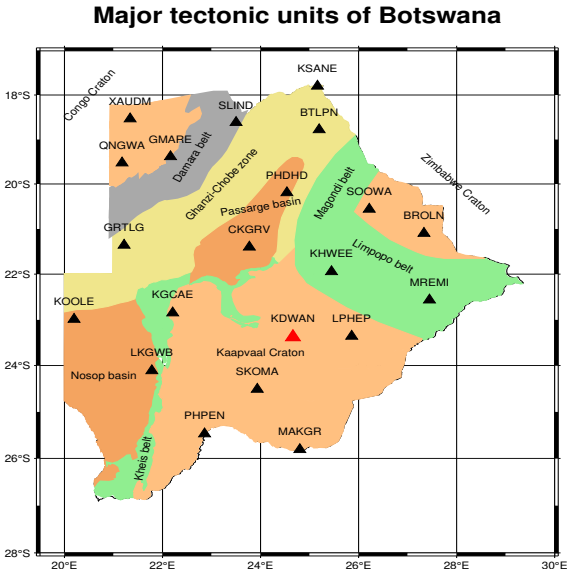


Figure 12: Tectonic map indicating station KDWAN in red.

Station KDWAN is located northeast of station SKOMA on the Kaapvaal craton. The receiver functions for this station were of sufficient quality, but did show some back azimuth variation. Therefore, receiver functions were binned on back azimuth for this station. This station is also on top of a large fault (Meghraoui & Grp, 2016), which may influence the results by adding complexity. Two different inversions were carried out for this stations, one with a receiver function stack with an average slowness of 5.8 $s/^\circ$ with back azimuth ranging between 37.0° and 82.6° (table 7); and one with an average slowness of 7.5 $s/^\circ$ with back azimuth ranging between 210.2° and 217.1° (table 8). The combined inversion results are shown in figure 13.

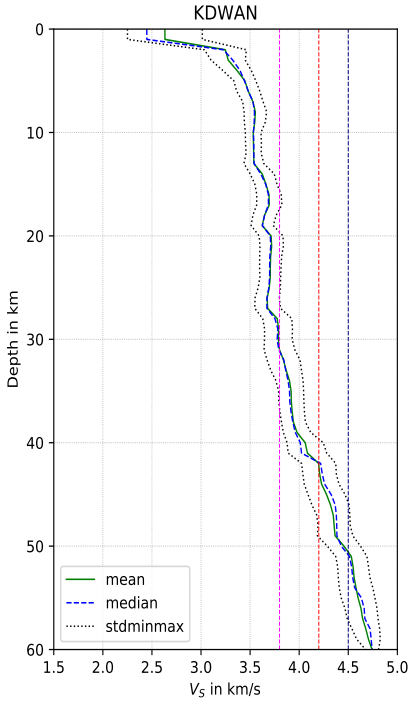


(a) Similar to figure 9a the mean and median velocity models with standard deviation for station KDWAN.

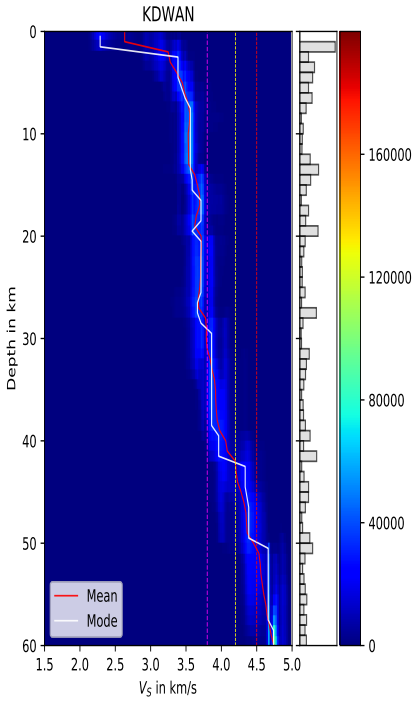


(b) Similar to figure 9b the mean and mode velocity models within the posterior Vs distribution for station KDWAN.

Figure 13: 1D velocity models of the inversions for station KDWAN. The vertical lines in both panels give the 3.8 km/s, 4.2 km/s and 4.5 km/s thresholds. The used events are given in tables 7 and 8 (7 events)

Just like station KGCAE, station KDWAN also has a low velocity sedimentary layer at the top. Other consistent features are a discontinuity at approximately 12-13 kilometers and one at approximately 40 kilometers. There appears to be a small increase in velocity at around 50 kilometers depth but this feature is not as clear as for station SKOMA in figure 8b.

For this station, I found a crustal thickness of approximately 42 kilometers, which is somewhat thicker than the 39 kilometers that Fadel et al. (2018) found.

### 5.1.4 PHPEN

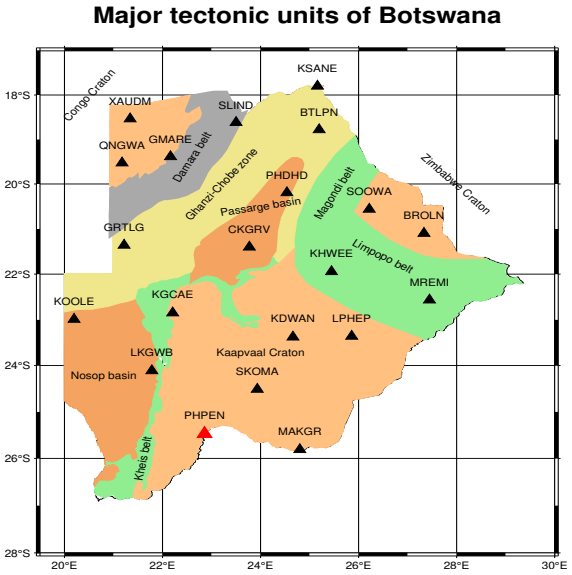


Figure 14: Tectonic map indicating station PHPEN in red.

Station PHPEN is located on the southern border of Botswana on the Kaapvaal craton. The receiver functions for this station were of relatively good quality, but did show some back azimuth variation. Therefore, receiver functions were binned on back azimuth for this station. Three different inversions were carried out for this stations, one with a receiver function stack with an average slowness of 5.5 s/° with back azimuth ranging between 227.7° and 240.2° (table 9), one with an average slowness of 6.7 s/° with back azimuth ranging between 211.6° and 220.4° (table 10); and one with an average slowness of 7.8 s/° with back azimuth between 213.3° and 217.8° (table 11). The combined inversion results are shown in figure 15.

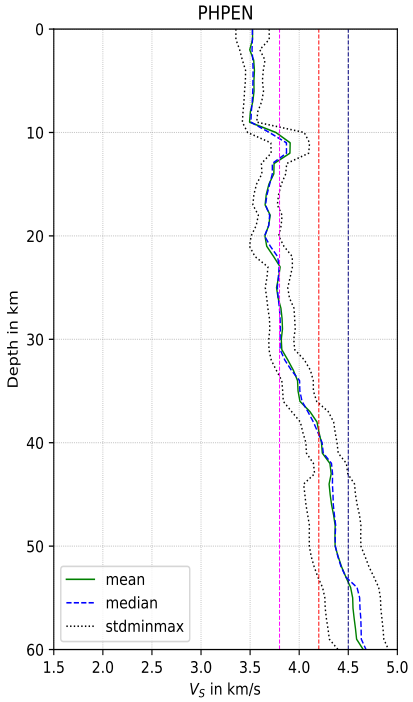


(a) Similar to figure 9a the mean and median velocity models with standard deviation for station PHPEN.

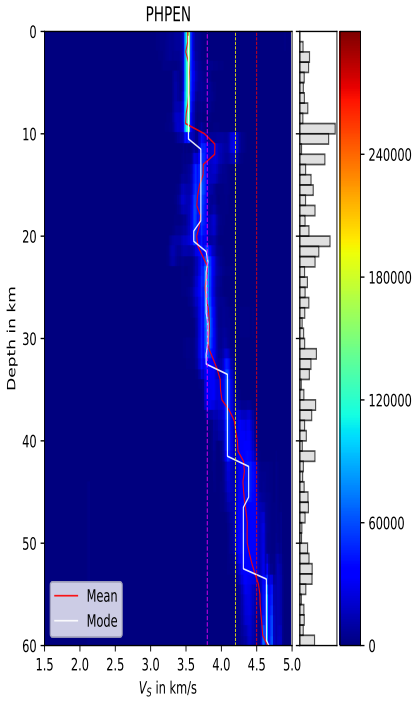


(b) Similar to figure 9b the mean and mode velocity models within the posterior Vs distribution for station PHPEN.

Figure 15: 1D velocity models of the inversions for station PHPEN. The vertical lines in both panels give the 3.8 km/s, 4.2 km/s and 4.5 km/s thresholds. The used events are given in tables 9, 10 and 11 (9 events)

The most defining feature of the crust beneath this station is the strong discontinuity at approximately 10 kilometers depth. In figure 15, there appears to be a low velocity zone between 12 and 20 kilometers. I think that this is not a real feature but caused by an overestimation of the velocity jump at the discontinuity at 10 kilometers depth. The deeper discontinuities for this station are not very clear and the variability between the models is fairly large. This expresses itself as a relatively large standard deviation in figure 15a.

I found a crustal thickness of approximately 39 kilometers for this station, which is similar to what Fadel et al. (2018) found (39 kilometers).

### 5.1.5 LPHEP

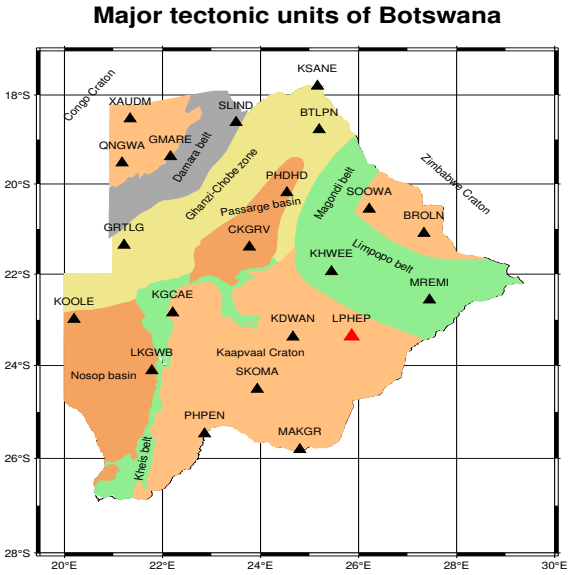


Figure 16: Tectonic map indicating station LPHEP in red.

Station LPHEP is located northeast of station SKOMA in the Kaapvaal craton close to the boundary with the Limpopo belt. The receiver functions for this station were of good quality. Two different inversions were carried out for this stations, one with a receiver function stack with an average slowness of 6.7 $s/^\circ$ with back azimuth ranging between 0° and 211° (table 12); and one with an average slowness of 7.5 $s/^\circ$ with back azimuth ranging between 210.3° and 216.4° (table 13). The combined inversion results are shown in figure 17.

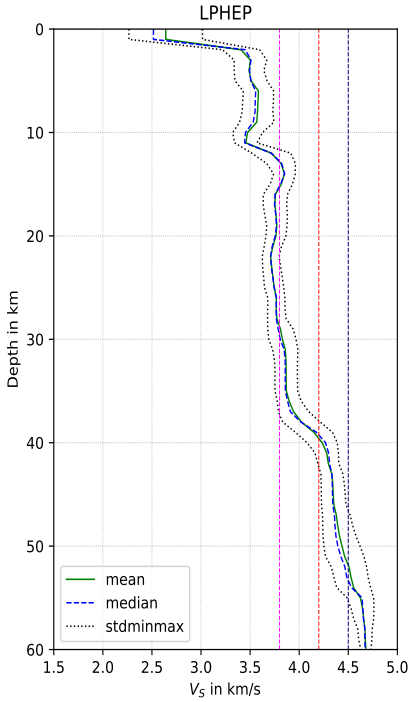


(a) Similar to figure 9a the mean and median velocity models with standard deviation for station LPHEP.

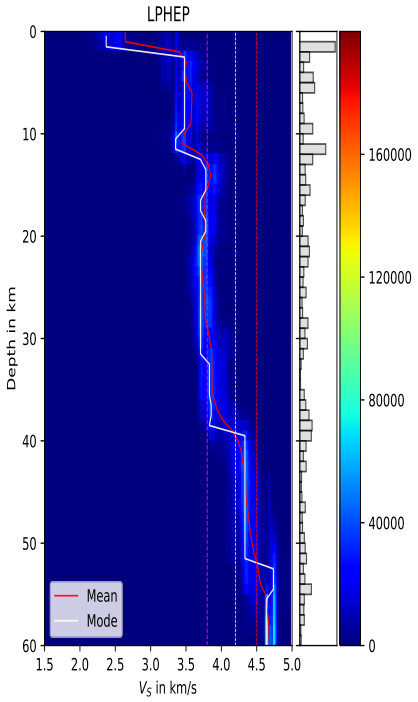


(b) Similar to figure 9b the mean and mode velocity models within the posterior Vs distribution for station LPHEP.

Figure 17: 1D velocity models of the inversions for station PHPEN. The vertical lines in both panels give the 3.8 km/s, 4.2 km/s and 4.5 km/s thresholds. The used events are given in tables 12 and 13 (11 events)

The models for station LPHEP (figure 17) contain a low velocity upper layer, a discontinuity at 11-12 kilometers, a discontinuity at 39-40 kilometers and an increased rate of velocity increase at approximately 50 kilometers. While not being a true discontinuity, something definitely happens at 50 kilometers depth.

I found a crustal thickness of around 39 kilometers, which is comparable to the 39 kilometers found by Fadel et al. (2018). Station LPHEP is close to stations SA63 (southeast of LPHEP) and SA64 (northeast of LPHEP) used by Kgaswane et al. (2009), Youssof et al. (2013) and Yu, Liu, et al. (2015) (only SA64). For station SA63, Kgaswane et al. (2009) and Youssof et al. (2013) found a crustal thickness of 43 kilometers, which is somewhat thicker than what I found for station LPHEP. For station SA64 Kgaswane et al. (2009) found a crustal thickness of 40.5 kilometers, Youssof et al. (2013) found a crustal thickness of 41 kilometers and Yu, Liu, et al. (2015) found a crustal thickness of 41.5 kilometers which is slightly thicker compared to my results.

### 5.1.6 MAKGR

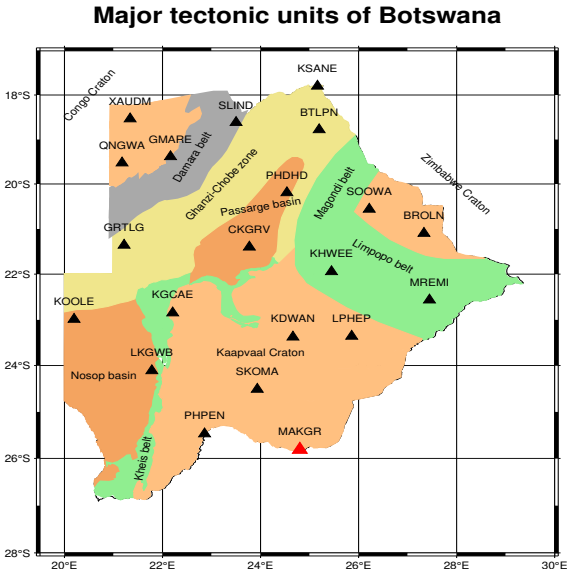


Figure 18: Tectonic map indicating station MAKGR in red.

Station MAKGR is located on the southern border of Botswana in the Kaapvaal craton, east of station PHPEN. The receiver functions for this station were of good quality. Three different inversions were carried out for this stations, one with a receiver function stack with an average slowness of 5.5 s/° with back azimuth ranging between 52° and 227° (table 14), one with an average slowness of 6.7 s/° with back azimuth ranging between 2° and 220° (table 15); and one with an average slowness of 7.7 s/° with back azimuth ranging between 210.1° and 217.5° (table 16). The combined inversion results are shown in figure 19.

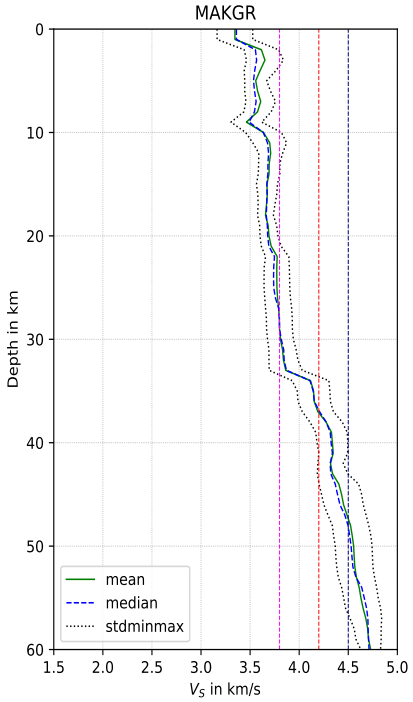


(a) Similar to figure 9a the mean and median velocity models with standard deviation for station MAKGR.

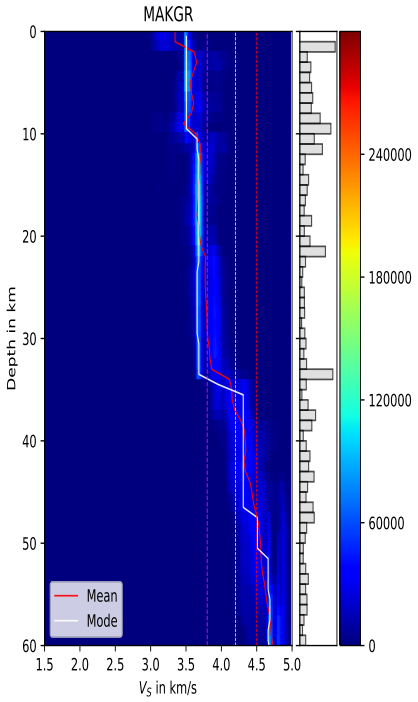


(b) Similar to figure 9b the mean and mode velocity models within the posterior Vs distribution for station MAKGR.

Figure 19: 1D velocity models of the inversions for station MAKGR. The vertical lines in both panels give the 3.8 km/s, 4.2 km/s and 4.5 km/s thresholds. The used events are given in tables 14, 15 and 16 (18 events)

The models for station MAKGR (figure 19) show a pronounced discontinuity at approximately 10 kilometers and one at around 36 kilometers.

For this station, I found a crustal thickness of around 37 kilometers, which is slightly shallower than what Fadel et al. (2018) found (38.0 kilometers). Close to this station, station SA38 is located. Kgaswane et al. (2009) found a crustal of 38 kilometers for this station and Youssof et al. (2013) found a crustal thickness of 39.5 kilometers which are both slightly deeper than what I found.

## 5.2 Discussion Kaapvaal craton

The models in the Kaapvaal craton all show similar structure as seen in figures 9, 11, 13, 15, 17 and 19. Especially the lower crustal structure is similar across the entire Botswana part of the Kaapvaal craton.

The northern stations (LPHEP, KDWAN and KGCAE) show a low velocity uppermost layer. This layer is interpreted as a layer of sedimentary rocks. The 3.8 km/s threshold is often crossed twice (within the standard deviation). Once at approximately 10-15 kilometers and once at 20-25 kilometers, which makes interpretation difficult. This discontinuity could be correlated to the Conrad discontinuity (Yang et al., 2021) which is observed globally in continental crust at depths of approximately between 10 and 20 kilometers (Abdelwahed et al., 2013). Given this depth range, the upper discontinuity is preferred as the interpreted Conrad discontinuity.

The lower crust in the Kaapvaal craton is characterized by two discontinuities. One at around 35-40 kilometers and one at around 50 kilometers. The 35 kilometer discontinuity is stronger at most stations. The velocity jumps to approximately 4.4 km/s at the 35 kilometer discontinuity and to approximately 4.6 km/s at the 50 kilometer discontinuity. In this study, I use a shear wave velocity of 4.2 km/s as a threshold for mantle velocities. That means that, in general, the shallower discontinuity is interpreted as the Moho. Around the entire Botswana part of the Kaapvaal craton, the crust is approximately 37 ($\pm$2 km) kilometers thick. This is similar to what is found by Fadel et al. (2018) and Youssof et al. (2013) based on receiver functions alone.

The lowermost discontinuity is often not a sharp discontinuity, it often is a zone where the velocity increase is stronger compared to the more or less constant velocity of the layer above. I interpret this layer as mafic material that has un-

derplated (Thybo and Artemieva, 2013) the Archean craton during one of the numerous magmatic events that affected the area. It is unclear whether the stations in southernmost Botswana (PHPEN and MAKGR) have this deepest discontinuity. I think they do as most models show a sharper increase in shear wave velocity around these depths than in the layer above and below. What is puzzling is the lack of mafic lower crustal xenoliths around this region (Fadel et al., 2018; Schmitz and Bowring, 2003). The xenoliths from Schmitz and Bowring (2003) were all Precambrian in age so a possible explanation could be that this magmatic underplating is younger. This is supported by the outpour of the mafic Karoo lavas in southern Africa around 180 Ma.

## 5.3 Limpopo belt

### 5.3.1 KHWEE

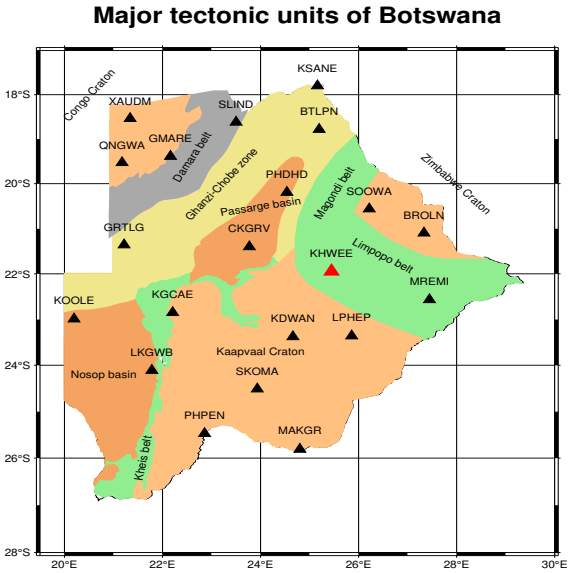


Figure 20: Tectonic map indicating station KHWEE in red.

Station KHWEE is located in the western part of the Limpopo belt. The receiver functions for this station were of very high quality. Three different inversions were carried out for this station, one with a receiver function with a slowness of 6.8 s/° with back azimuth of 12° (table 17), one with an average slowness of 7.0 s/° with back azimuth ranging between 0.3° and 19.5° (table 18); and one with an average slowness of 7.5 s/° with back azimuth ranging between 133.7° and 216.6° (table 19). The combined inversion results are shown in figure 21.

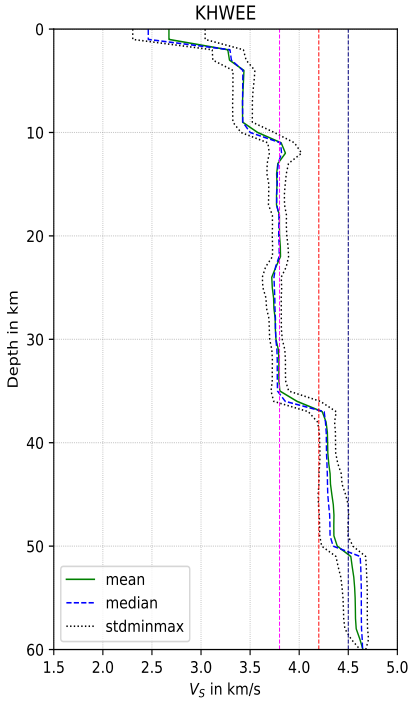


(a) Similar to figure 9a the mean and median velocity models with standard deviation for station KHWEE.

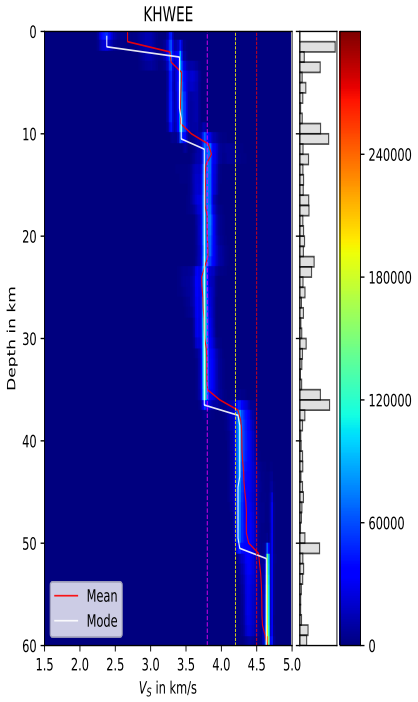


(b) Similar to figure 9b the mean and mode velocity models within the posterior Vs distribution for station KHWEE.

Figure 21: 1D velocity models of the inversions for station KHWEE. The vertical lines in both panels give the 3.8 km/s, 4.2 km/s and 4.5 km/s thresholds. The used events are given in tables 17, 17 and 19 (10 events)

The upper 40 kilometers of the models shown in figure 21 are all very consistent. All of the models show three well defined discontinuities in this part of the domain. At approximately 2 kilometers depth, there is a large discontinuity that is likely related to the sedimentary overburden. All models have a discontinuity at 10 kilometers and one at approximately 36 kilometers. There is also a smaller discontinuity at approximately 50 kilometers depth.

For this station, I found a crustal thickness of approximately 36 kilometers, which is significantly thinner than the 40 kilometers that was found by Fadel et al. (2018).

### 5.3.2 MREMI

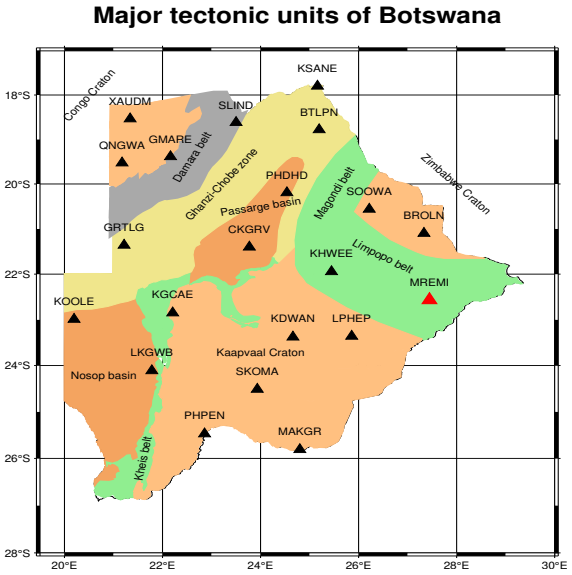


Figure 22: Tectonic map indicating station MREMI in red.

Station MREMI is located in the eastern part of the Limpopo belt. The receiver functions for this station were of middling quality. For this station, the receiver functions showed back azimuth dependence, therefore, the receiver functions were binned based on back azimuth as well as on slowness. Three different inversions were carried out for this stations, one with a receiver function stack with a slowness of 5.8 s/° with back azimuth ranging between 35.7° and 76.6° (table 20), one with an average slowness of 6.8 s/° with back azimuth ranging between 359.0° and 10.4° (table 21); and one with an average slowness of 7.4 s/° with back azimuth ranging between 211.9° and 217.2° (table 22). The combined inversion results are shown in figure 23.

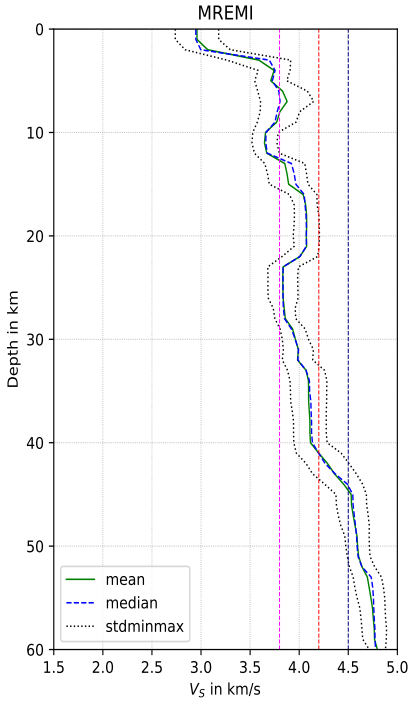


(a) Similar to figure 9a the mean and median velocity models with standard deviation for station MREMI.

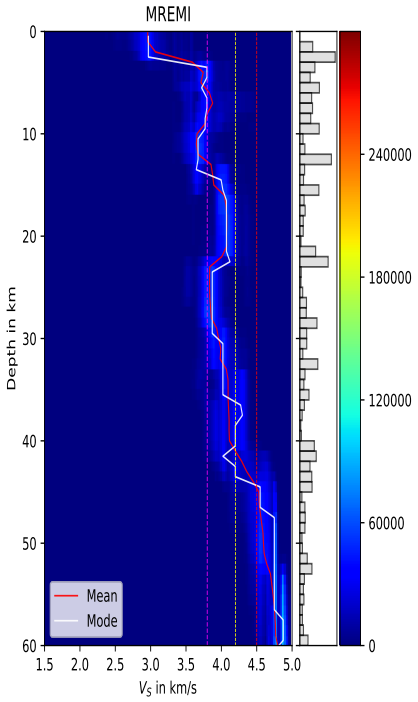


(b) Similar to figure 9b the mean and mode velocity models within the posterior Vs distribution for station MREMI.

Figure 23: 1D velocity models of the inversions for station MREMI. The vertical lines in both panels give the 3.8 km/s, 4.2 km/s and 4.5 km/s thresholds. The used events are given in tables 20, 21 and 22 (9 events)

Most features below station MREMI are fairly consistent across all the models. There is a low velocity upper layer, a discontinuity at 12-15 kilometers and a discontinuity at 40-43 kilometers. The 3.8 km/s threshold is crossed multiple times, the most consistent crossing is the discontinuity at approximately 12 kilometers. The 4.2 km/s and 4.5 km/s thresholds are exceeded at the 40-43 kilometer discontinuity.

For this station, I found a crustal thickness of around 42 kilometers, which is the same as the 42 kilometers found by Fadel et al. (2018). This station is very close to the SA65 and B1665 stations. For station SA65, Kgaswane et al. (2009) found a crustal thickness of 40.5 kilometers, Youssof et al. (2013) found 43 kilometers and Yu, Gao, et al. (2015) found 42.7 kilometers for station SA65 and 42.6 kilometers for station B1665.

## 5.4 Discussion Limpopo belt

The models that are obtained for station KHWEE (figures 21) in the Limpopo belt are the best resolved models that I obtained in this study. There are four very clear discontinuities that were fairly consistent over all the the individual inversions for this station. The upper discontinuity is interpreted as the bottom of the layer of sediments on top of the basement. The discontinuity at approximately 10 kilometers can be interpreted as the Conrad discontinuity (Yang et al., 2021) from a felsic upper crust to an intermediate composition middle crust.

In the lower half of the model domain, like in the Kaapvaal craton, we see a double discontinuity structure of one discontinuity at 36 kilometers and one at 51 kilometers. Because the upper one of these exceeds the 4.2 km/s threshold, we interpret that one as the Moho. I think that the lower high velocity layer is a consequence of mafic underplating during intrusion of the Okavango dyke swarm. This is similar to the interpretation that Gore et al. (2009) and Delph and Porter (2015) make. Station MREMI shows a very different structure from what we have seen for station KHWEE. However, these models are not as well resolved as the models for station KHWEE. There are three things that are visible in all models from station MREMI: a low velocity uppermost layer, a low velocity zone in the mid-crust (although the exact depth and width varies) and the Moho at approximately 42 kilometers. The low velocity upper layer is probably related to the sedimentary overburden. An interesting feature in figure 23 is the low velocity zone between (approximately) 20-30 kilometers is also found for station SA64 (relatively close to MREMI) by Kgaswane et al. (2009). The Moho being at 42 kilometers means that there is a significant thickening in the Limpopo belt from west to east in Botswana.

## 5.5 Zimbabwe craton

### 5.5.1 BROLN

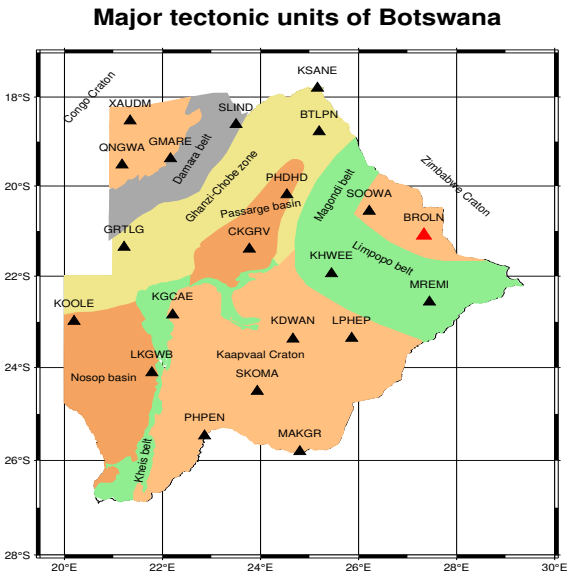


Figure 24: Tectonic map indicating station BROLN in red.

Station BROLN is located in the northwestern part of Botswana on the Zimbabwe craton. The receiver functions for this station were of high quality. Two different inversions were carried out for this stations, one with a receiver function stack with a slowness of 6.2 s/° with back azimuth ranging between 35.7° and 210.4° (table 23) and one with an average slowness of 7.3 s/° with back azimuth ranging between 353.9° and 285.4° (table 24). The combined inversion results are given in figure 25.

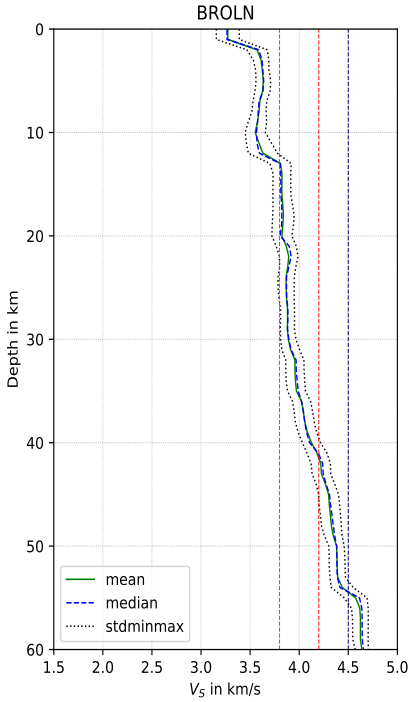


(a) Similar to figure 9a the mean and median velocity models with standard deviation for station BROLN.

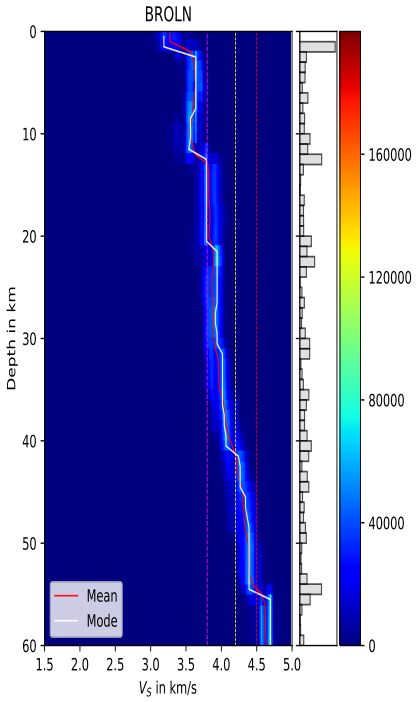


(b) Similar to figure 9b the mean and mode velocity models within the posterior Vs distribution for station BROLN.

Figure 25: 1D velocity models of the inversions for station BROLN. The vertical lines in both panels give the 3.8 km/s, 4.2 km/s and 4.5 km/s thresholds. The used events are given in tables 23 and 24 (13 events)

The most noticeable thing about the models in figure 25 is the smoothness of the models. All of the models show a discontinuity in the upper 2 kilometers, one at 12 kilometers and one at approximately 55 kilometers. Although the deepest one was not consistent across all inversions.

For this station, I found a crustal thickness of around 41 kilometers. This is close to the 40 kilometers that Fadel et al. (2018) found. This station is very close to station SA71. For this station, Kgaswane et al. (2009) found a crustal thickness of 43.0 kilometers and Youssof et al. (2013) found a crustal thickness of 40.5 kilometers. The model found by Kgaswane et al. (2009) is also very smooth, except for their Moho, which is sharp.

### 5.5.2 SOOWA

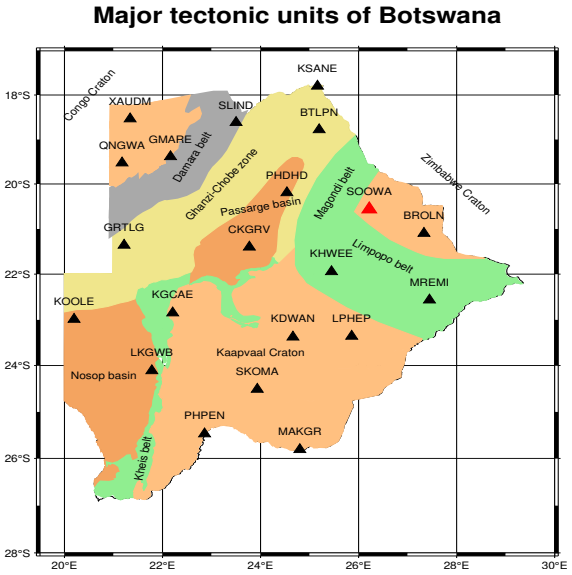


Figure 26: Tectonic map indicating station SOOWA in red.

Station SOOWA is located in the northeastern part of Botswana on the Zimbabwe craton. The receiver functions for this station were of middling quality. For this station, the receiver functions showed back azimuth dependence, therefore, the receiver functions were binned based on back azimuth as well as on slowness. Three different inversions were carried out for this station, one with a receiver function stack with a slowness of 5.9 s/° with back azimuth ranging between 52.4° and 77.7° (table 25), one with an average slowness of 7.3 s/° with and back azimuth ranging between 212.0° and 216.2° (table 26); and one with an average slowness of 7.7 s/° with back azimuth ranging between 288.1° and 289.8° (table 27). The combined inversion results are shown in figure 27.

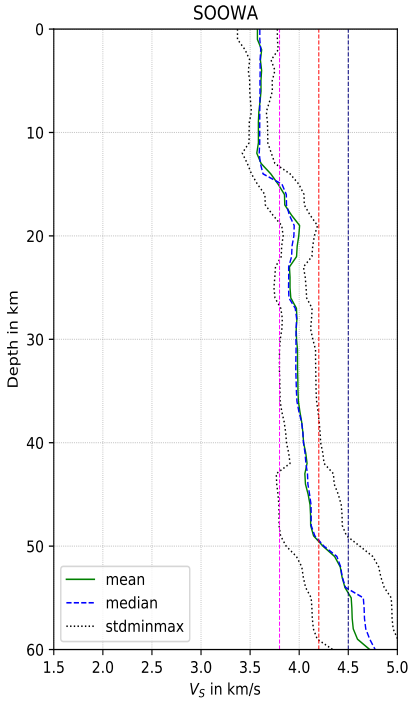


(a) Similar to figure 9a the mean and median velocity models with standard deviation for station SOOWA.

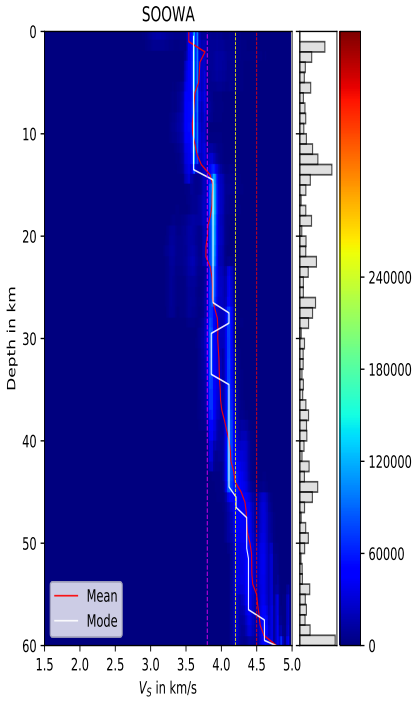


(b) Similar to figure 9b the mean and mode velocity models within the posterior Vs distribution for station SOOWA.

Figure 27: 1D velocity models of the inversions for station SOOWA. The vertical lines in both panels give the 3.8 km/s, 4.2 km/s and 4.5 km/s thresholds. The used events are given in tables 25, 26 and 27 (8 events)

Just as the models from station BROLN, the models from station SOOWA show a high degree of smoothness. All of the models from this station show a discontinuity at approximately 14 kilometers and one between 50 and 55 kilometers. Below 40 kilometers, the uncertainty becomes large, which is expressed by the large standard deviation in figure 27a. This is caused by a large variability between inversions at these depths.

For this station, I found a crustal thickness of 49 kilometers. This is comparable to the 49 kilometers found by Fadel et al. (2018).

## 5.6 Discussion Zimbabwe craton

One thing that stood out in the receiver functions for this terrain was that the Moho Ps conversion appeared to be relatively weak. This implies that the velocity contrast between crust and mantle is smaller than in the Kaapvaal craton. This could be explained by mafic intrusions from the Okavango dyke swarm that cross cut through this part of the Zimbabwe craton. This could cause the lower crust in this area to be more mafic due to underplating and thus explain the weak Moho conversion. This was also found and interpreted as such by Delph and Porter (2015) from the Okavango dyke swarm intrusion event. At both stations BROLN and SOOWA (figures 25 and 27) a well resolved discontinuity appears at 12 and 14 kilometers respectively. Similar to our interpretation in the Kaapvaal craton and the Limpopo belt, this discontinuity is probably related to the Conrad discontinuity.

The crustal thickness in the southwestern part of the Zimbabwe craton varies significantly. The crust below station SOOWA is about 8 kilometers thicker than the crust below station BROLN. The thick crust could be related to the intrustion of the Okavango dyke swarm by the means of underplating, but if this were the case, a thick crust below station BROLN is also expected. Since this is not the case, the more likely explanation is the fact that station SOOWA is very close to the boundary with the Magondi belt. Nguuri et al. (2001) explain this thick crust with post-Archean reworking near the edges of the Zimbabwe craton..

## 5.7 Nosop basin

### 5.7.1 LKGWB

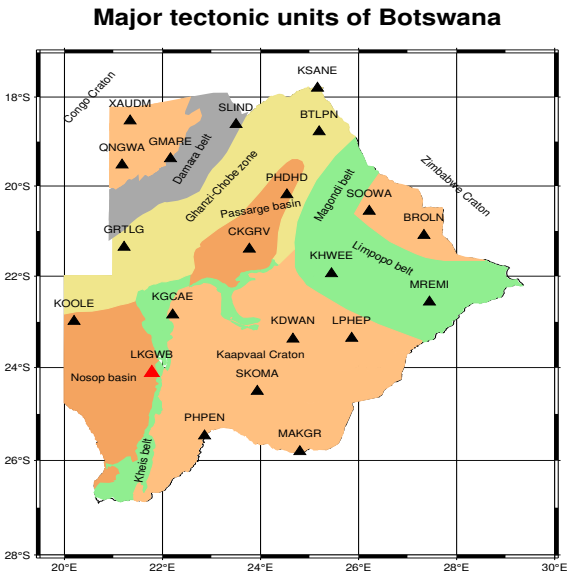


Figure 28: Tectonic map indicating station LKGWB in red.

Station LKGWB is located in the eastern part of the Nosop basin on the boundary with the Kheis belt. The receiver functions for this station were of middling quality. For this station, the receiver functions showed back azimuth dependence, therefore, the receiver functions were binned based on back azimuth as well as on slowness. This unfortunately had as a side effect that two inversions were carried out with just a single receiver function. Three different inversions were carried out for this stations, two with receiver functions with a slowness of 5.6 s/° with back azimuth of 75.7° and 227.8° (tables 28 and 29), and one with an average slowness of 7.8 s/° with back azimuth ranging between 210.8° and 212.3° (table 30). The combined inversion results are shown in figure 29.

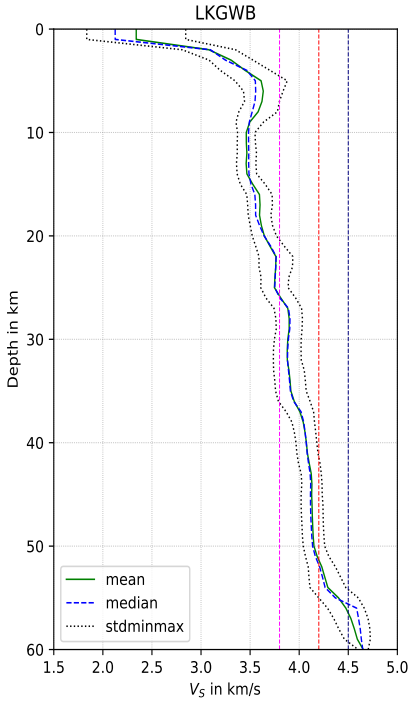


(a) Similar to figure 9a the mean and median velocity models with standard deviation for station LKGWB.

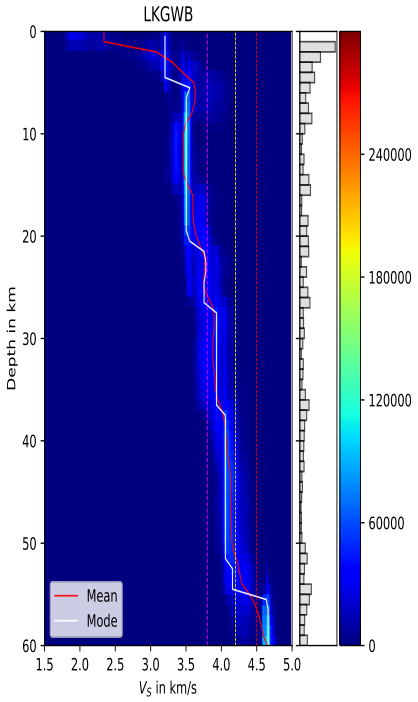


(b) Similar to figure 9b the mean and mode velocity models within the posterior Vs distribution for station LKGWB.

Figure 29: 1D velocity models of the inversions for station LKGWB. The vertical lines in both panels give the 3.8 km/s, 4.2 km/s and 4.5 km/s thresholds. The used events are given in tables 28, 29 and 30 (4 events)

The models from station LKGWB are surprisingly consistent given the limited amount of receiver functions and the relatively low quality of the receiver functions, which results in a relatively small standard deviation for the combined model. The model in figure 29 contain a low velocity upper layer and all of the models contain a discontinuity at approximately 20 kilometers.

The lower part of the model domain contains one larger discontinuity at around 55 kilometers, however, neither of the discontinuities for this station are very well resolved (except for the shallowest one) as can be seen in the histogram in figure 29b.

I have found a crustal thickness of around 52 kilometers. This is significantly thicker than the 39 kilometers found by Fadel et al. (2018). However, many models also show a discontinuity around 37 kilometers.

### 5.7.2 KOOLE

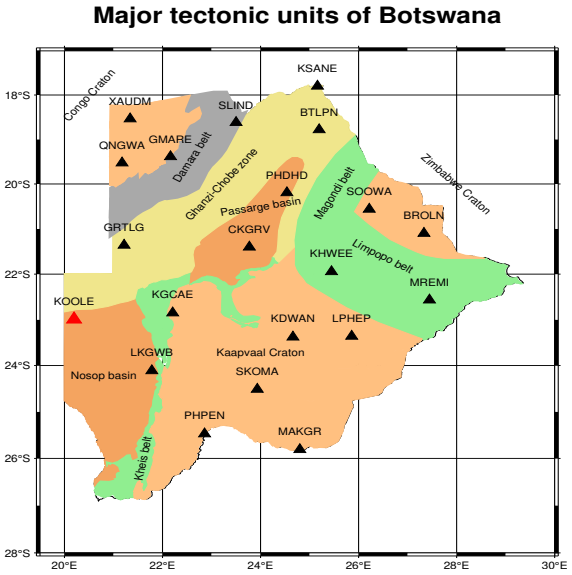


Figure 30: Tectonic map indicating station KOOLE in red.

Station KOOLE is located in the western part of the Nosop basin close to the border with Namibia. The receiver functions for this station were of good quality. Two different inversions were carried out for this station, one with a receiver functions with an average slowness of 6.7 s/° with back azimuth ranging between 16.5° and 36.4° (table 31), and one with an average slowness of 7.7 s/° with back azimuth ranging between 51.1° and 216° (table 32). The combined inversion results are shown in figure 31.

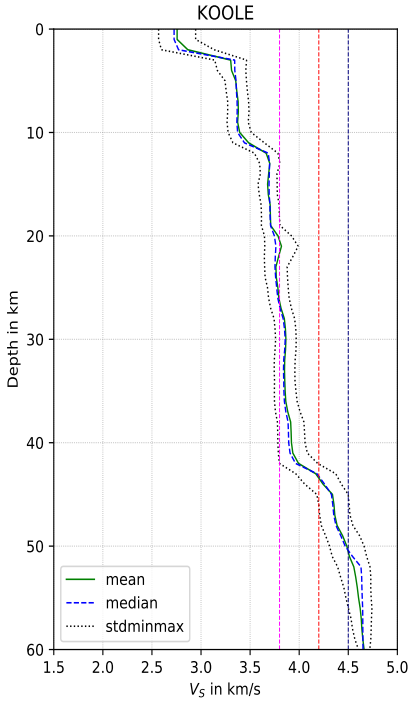


(a) Similar to figure 9a the mean and median velocity models with standard deviation for station KOOLE.

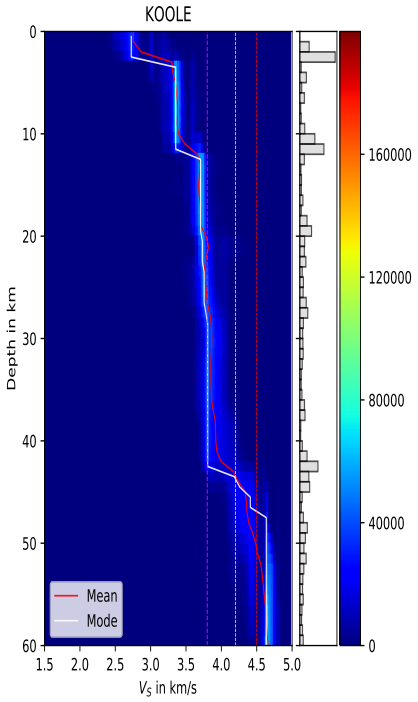


(b) Similar to figure 9b the mean and mode velocity models within the posterior Vs distribution for station KOOLE.

Figure 31: 1D velocity models of the inversions for station KOOLE. The vertical lines in both panels give the 3.8 km/s, 4.2 km/s and 4.5 km/s thresholds. The used events are given in tables 31 and 32 (8 events)

The model for station KOOLE in figure 31 is fairly well resolved. The model contains a low velocity upper layer, a discontinuity at approximately 11 kilometers, and a discontinuity at approximately 42 kilometers.

For this station, I found a crustal thickness of around 43 kilometers, which is slightly thicker than (but still comparable to) the 42 kilometers found by Fadel et al. (2018)

## 5.8 Discussion Nosop basin

We see that the structure varies quite strongly in this area. This is probably because station LKGWB samples the structure from the Kheis belt more than the structure from the Nosop basin. The major similarity between these stations lies in the uppermost low velocity layer found at both stations. This discontinuity is probably related to the sediments that cover the area. Station KOOLE also shows a discontinuity at approximately 11 kilometers depth. Earlier, I have interpreted this as the Conrad discontinuity. However, in the sedimentary thickness map found in Fadel et al., 2018 we see that the Nosop basin is 10-15 kilometers deep at the location of this station. It is thinkable that on this specific location, this discontinuity might be related to the bottom of the Nosop basin and not the Conrad discontinuity.

There are several theories about the nature of the basement below the Nosop basin. Some argue that it is an extension of the Kaapvaal craton while others argue that it is a buried separate cratonic unit (Begg et al., 2009; Fadel et al., 2018). My results support the latter as the double discontinuity structure that is found in the Kaapvaal craton lacks in this area. Fadel et al., 2018 found a Vp/Vs ratio of 1.76 suggesting an intermediate Archean composition further supporting the idea that the basement below the basin is cratonic.

The internal crustal structure below station LKGWB shows significant difference between different back azimuths of the receiver functions. What all the models for this station have in common is a low velocity in the uppermost layer of about 2 kilometers thick. This is probably related to the sedimentary overburden. The second thing that all of the models have in common is the large crustal thickness. The 4.2 km/s threshold is exceeded at around 51 kilometers. This is thicker than the adjacent terrains (Kaapvaal craton and Nosop basin) and is likely to be the crustal thickness of the Kheis belt. This further supports the idea that the underlying structure of this relatively thick terrain separates the Kaapvaal craton from the Mahaltohe micro-craton (Fadel et al., 2018).

## 5.9 Ghanzi-Chobe zone

### 5.9.1 KSANE

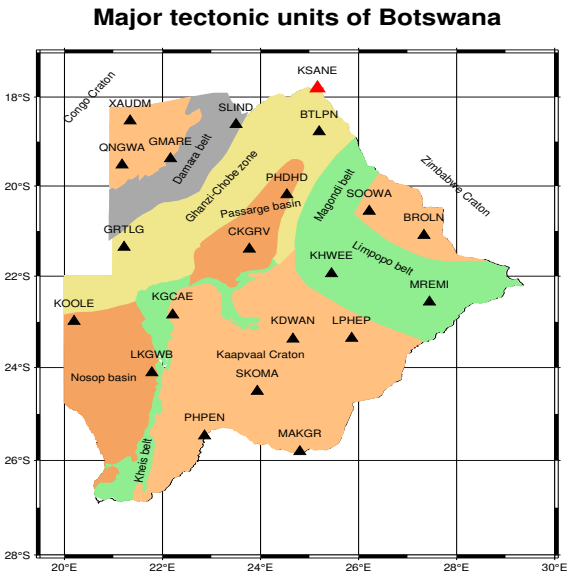


Figure 32: Tectonic map indicating station KSANE in red.

Station KSANE is located in the northern part of the Okavango delta near the border with Namibia, Zambia and Zimbabwe. The receiver functions for this station were of good quality, but did show back azimuth dependence making back azimuth binning necessary. Three different inversions were carried out for this station, Two with a receiver function stack with an average slowness of 7.1 s/°; one with back azimuth ranging between 13.0° and 20.6° (table 33) and one with a back azimuth of 214.9° (table 34). The third inversion was done with a receiver function stack with an average slowness of 7.3 s/° with back azimuth ranging between 212.1° and 213.2° (table 35). The combined inversion results are shown in figure 33.

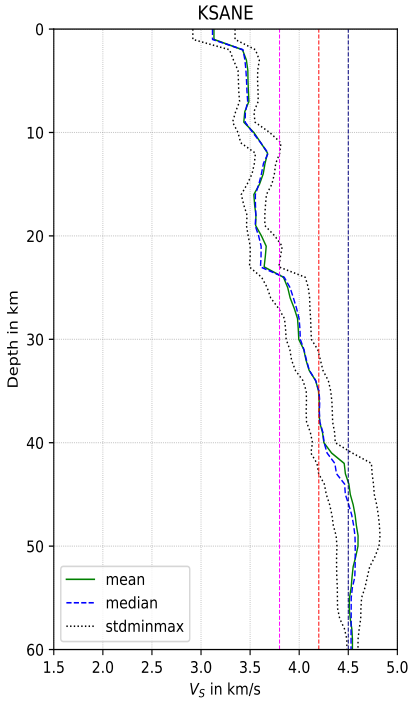


(a) Similar to figure 9a the mean and median velocity models with standard deviation for station KSANE.

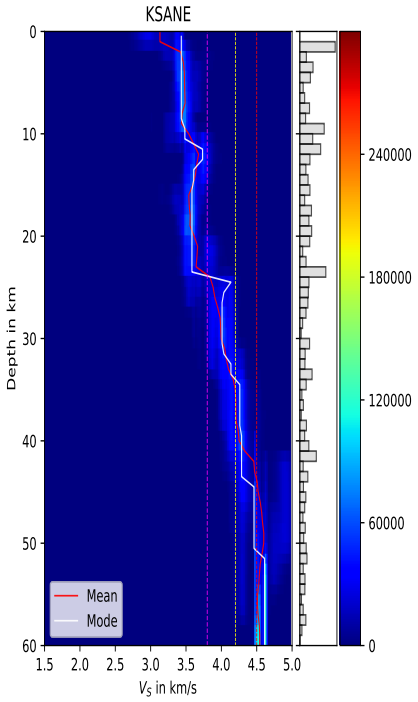


(b) Similar to figure 9b the mean and mode velocity models within the posterior Vs distribution for station KSANE.

Figure 33: 1D velocity models of the inversions for station KSANE. The vertical lines in both panels give the 3.8 km/s, 4.2 km/s and 4.5 km/s thresholds. The used events are given in tables 33, 34 and 35 (7 events)

The models of the crust below station KSANE show a few distinctive features: a discontinuity at approximately 10 kilometers, a discontinuity at approximately 24 kilometers and one at approximately 42 kilometers. Another important thing is that the uncertainty significantly increases below 40 kilometers, which is expressed in a large standard deviation in figure 33a.

For this station, I found a crustal thickness of around 36 kilometers, which is slightly thinner than the 38 kilometers found by Fadel et al. (2018).

### 5.9.2 CKGRV

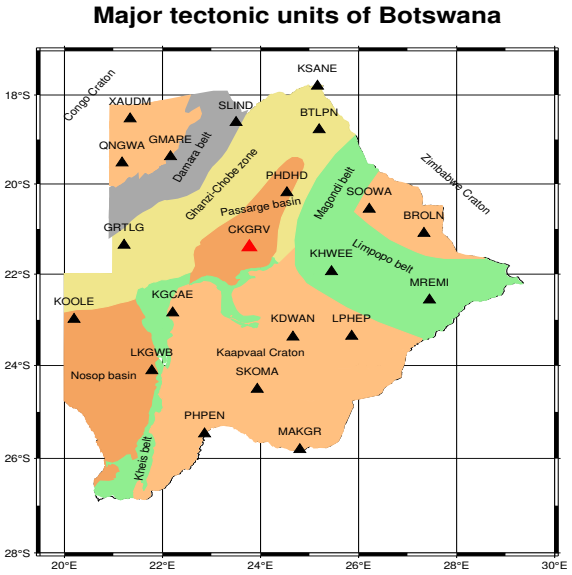


Figure 34: Tectonic map indicating station CKGRV in red.

Station CKGRV is located in the central part of Botswana in the southern part of the Passarge basin. The receiver functions for this station were of good quality, but limited in quantity. Two different inversions were carried out for this station, One with a receiver function stack with an average slowness of 5.7 s/° with back azimuth ranging between 37.9° and 53.5° (table 36) and one with an average slowness of 7.4 s/° with back azimuth of 209.0° (table 37). The combined inversion results are shown in figure 35.

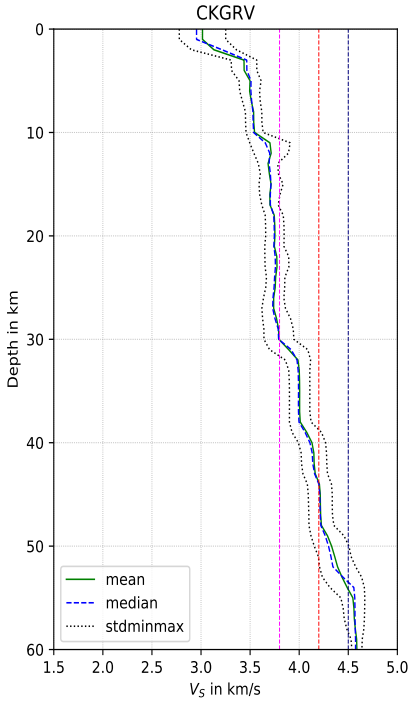


(a) Similar to figure 9a the mean and median velocity models with standard deviation for station CKGRV.

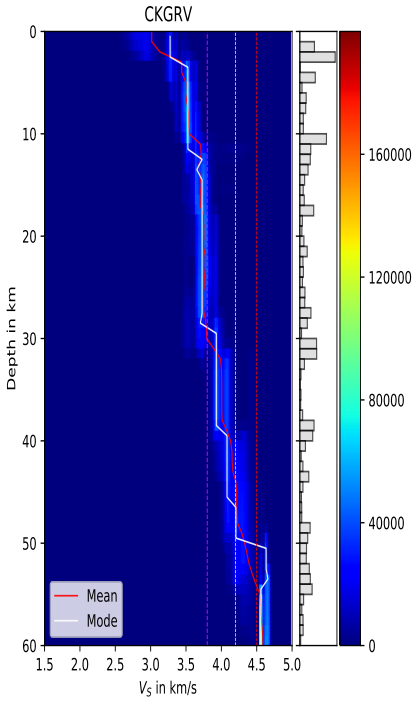


(b) Similar to figure 9b the mean and mode velocity models within the posterior Vs distribution for station CKGRV.

Figure 35: 1D velocity models of the inversions for station CKGRV. The vertical lines in both panels give the 3.8 km/s, 4.2 km/s and 4.5 km/s thresholds. The used events are given in tables 36 and 37 (4 events)

The crust below station CKGRV shows a few distinctive features. A discontinuity at approximately 3 kilometers depth that is potentially related to the sediments in the Passarge basin. A smaller discontinuity is located around 11 kilometers and 30 kilometers. Below 30 kilometers the structure becomes smoother; there appear to be discontinuities at approximately 40 kilometers and 50 kilometers but these are not as clear as the discontinuities at shallower depths.

For this station, I find a crustal thickness of around 44 kilometers which is significantly thicker than the 37 kilometers found by Fadel et al. (2018). However, they also note that their solution for this station is ambiguous. They also found a solution with a crustal thickness of more than 49 kilometers. The solution I found here is approximately the average of the two solutions found by Fadel et al. (2018).

### 5.9.3 GRTLG

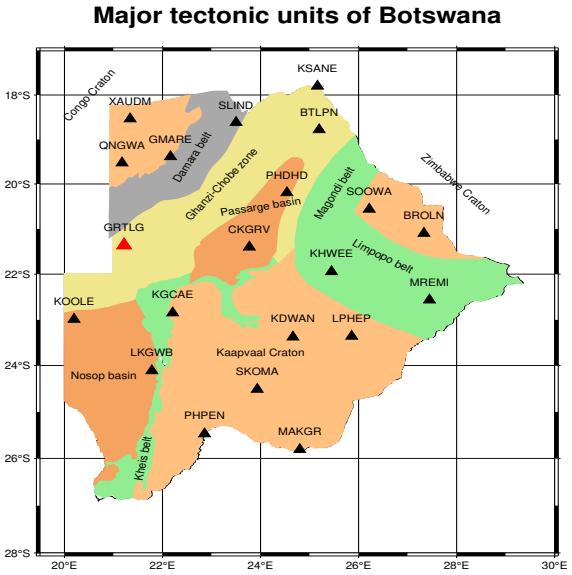


Figure 36: Tectonic map indicating station GRTLG in red.

Station GRTLG is located in the western part of the Ghanzi-Chobe zone near the border with Namibia. The receiver functions for this station were of acceptable quality, but did show back azimuth dependence making back azimuth binning necessary. Three different inversions were carried out for this station, One with a receiver function stack with an average slowness of 5.5 s/° with back azimuth ranging between 53.7° and 86.1° (table 38), one with an average slowness of 5.6 s/° with back azimuth ranging between 82.4° and 84.6 s/° (table 39) and one with an average slowness of 6.9 s/° with back azimuth ranging between 5.1° and 23.2° (table 40). The combined inversion results are shown in figure 37.

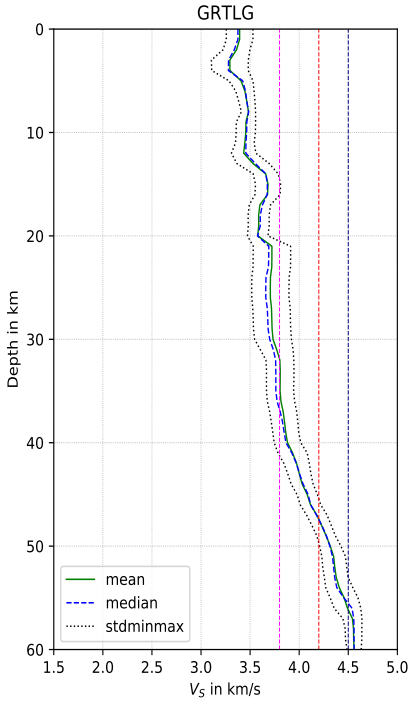


(a) Similar to figure 9a the mean and median velocity models with standard deviation for station GRTLG.

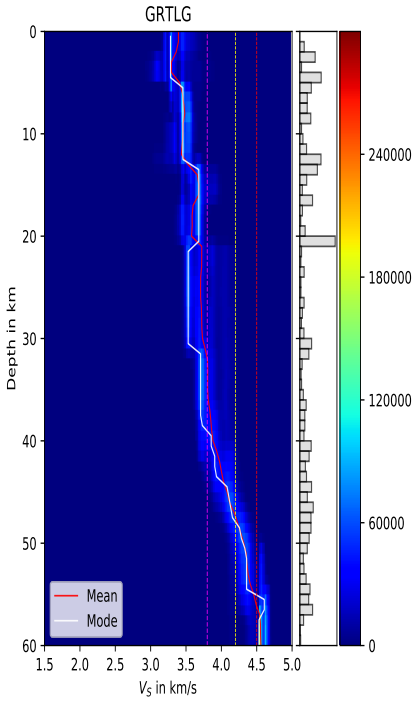


(b) Similar to figure 9b the mean and mode velocity models within the posterior Vs distribution for station GRTLG.

Figure 37: 1D velocity models of the inversions for station GRTLG. The vertical lines in both panels give the 3.8 km/s, 4.2 km/s and 4.5 km/s thresholds. The used events are given in tables 38, 39 and 40 (9 events)

What stands out the most in the models from station GRTLG is the very high degree of smoothness (especially in the lower part of the model domain). This makes interpreting this model difficult, the only discontinuity that is properly resolved is one at approximately 20 kilometers.

With the 4.2 km/s Moho threshold it is still possible to estimate the crustal thickness. With this, I found a crustal thickness of around 47 kilometers which is fairly close to the 46 kilometers found by Fadel et al. (2018).

### 5.9.4 BTLPN

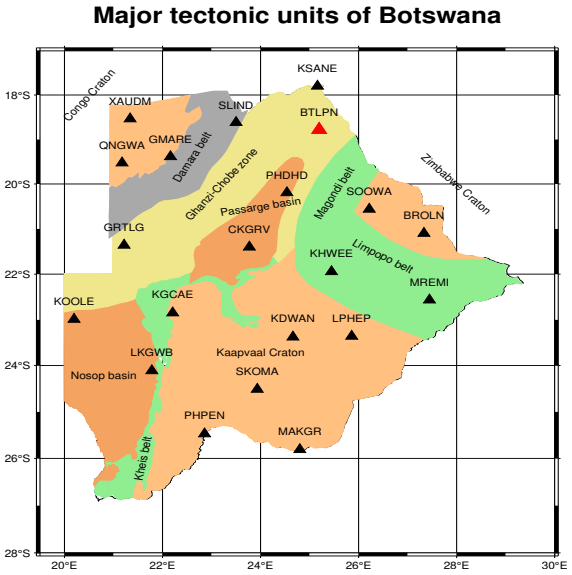


Figure 38: Tectonic map indicating station BTLPN in red.

Station BTLPN is located in the northern part of Botswana in the Okavango delta. The receiver functions for this station were of middling quality. Two different inversions were carried out for this station, One with a receiver function stack with an average slowness of 5.9 s/° with back azimuth ranging between 37.0° and 37.2° (table 41) and one with an average slowness of 7.2 s/° with back azimuth ranging between 2.2° and 215.3° (table 42). The combined inversion results are shown in figure 39.

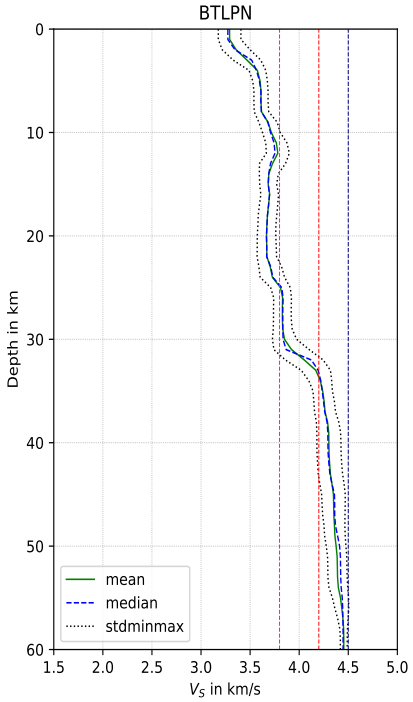


(a) Similar to figure 9a the mean and median velocity models with standard deviation for station BTLPN.

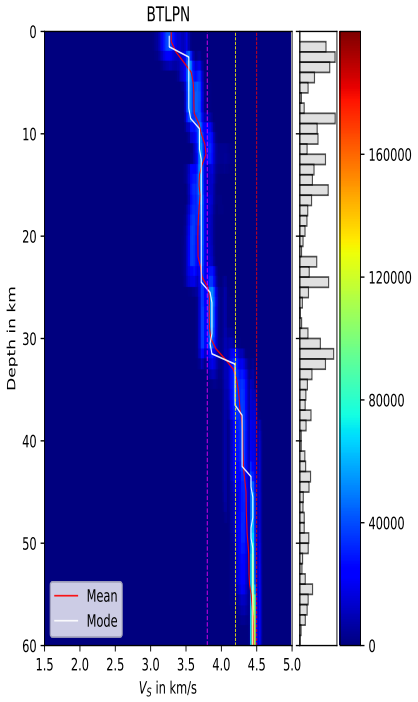


(b) Similar to figure 9b the mean and mode velocity models within the posterior Vs distribution for station BTLPN.

Figure 39: 1D velocity models of the inversions for station BTLPN. The vertical lines in both panels give the 3.8 km/s, 4.2 km/s and 4.5 km/s thresholds. The used events are given in tables 41 and 42 (5 events)

The crust below station BTLPN is quite different from the other stations in Botswana. The main feature of this model is the large discontinuity at approximately 33 kilometers depth. Other features are a discontinuity at 3 kilometers, one between 10 and 15 kilometers, the latter one is not very well resolved as can be seen from the very wide distribution in the histogram in figure 39b. Lastly, a very small discontinuity can be seen at 25 kilometers.

For this station, I found a crustal thickness of around 33 kilometers which is similar to the 34 kilometers found by Fadel et al. (2018).

### 5.9.5 PHDHD

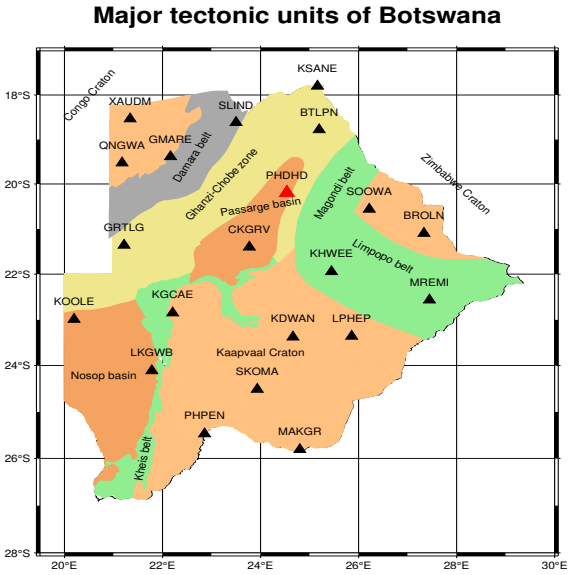


Figure 40: Tectonic map indicating station PHDHD in red.

Station PHDHD is located in the central part of the Ghanzi-Chobe zone near the boundary with the Magondi belt. The receiver functions for this station were of acceptable quality, but did show back azimuth dependence making back azimuth binning necessary. Three different inversions were carried out for this station, One with a receiver function with a slowness of 5.8 s/° with back azimuth of 78.5° (table 43) one with an average slowness of 7.0 s/° with back azimuth ranging between 2.8° and 20.6 s/° (table 44) and one with a slowness of 7.3 s/° with back azimuth of 215.7° (table 45). The combined inversion results are shown in figure 41.

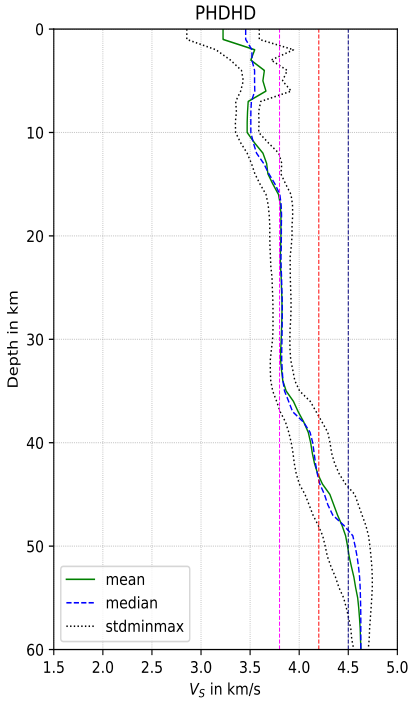


(a) Similar to figure 9a the mean and median velocity models with standard deviation for station PHDHD.

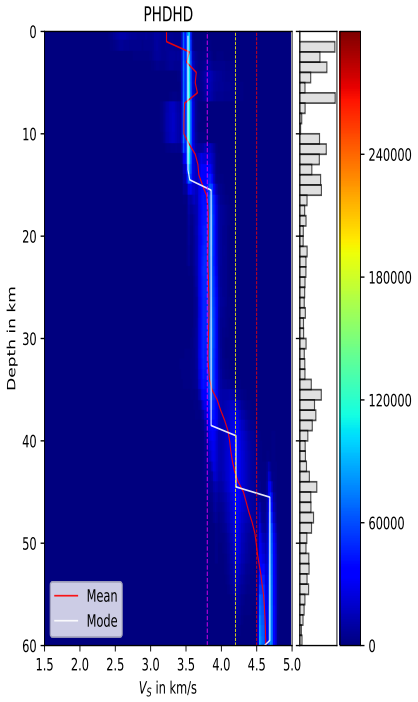


(b) Similar to figure 9b the mean and mode velocity models within the posterior Vs distribution for station PHDHD.

Figure 41: 1D velocity models of the inversions for station PHDHD. The vertical lines in both panels give the 3.8 km/s, 4.2 km/s and 4.5 km/s thresholds. The used events are given in tables 43, 44 and 45 (4 events)

The mean and median models (figure 41a) of the crust below station PHDHD are pretty smooth. On the other hand, the mode model (figure 41b) shows three distinctive discontinuities, however, the histograms in the same figure show that the exact depth of the discontinuities is uncertain as the distributions are wide. There is a discontinuity at approximately 2 kilometers, one around 10-15 kilometers, one around 35-40 kilometers and one around 45-50 kilometers.

For this station, I found a crustal thickness of around 43 kilometers which is significantly thicker than the 37 kilometers found by Fadel et al. (2018) (although the uncertainty in my result is fairly large as can be seen in figure 41). Station PHDHD is close to stations B04KH and B05MO. For these stations Yu, Liu, et al. (2015) found crustal thicknesses of 42.6 and 40.7 kilometers respectively which is closer to what I found.

## 5.10 Discussion Ghanzi-Chobe zone

The Ghanzi-Chobe zone was originally a rift basin that later deformed during the Pan-African orogeny as Gondwana assembled (Modie, 2000). The crustal structure within this zone varies significantly as is shown in the velocity models. In the north of Botswana in the Okavango delta (stations KSANE and BTLPN) we see a relatively thin crust (35 kilometers at KSANE and 33 kilometers at BTLPN). This is probably caused by recent rifting in the Okavango rift zone causing crustal thinning. This is also reflected in the relatively low velocities below the Moho. The velocities barely exceed 4.5 km/s indicating higher temperatures and/or the presence of fluids/melt. This is further supported by the results from Fadel et al. (2020); they find a low velocity zone below the Okavango delta in the upper mantle.

The stations in the Passarge basin (CKGRV and PHDHD) show a fairly similar structure to what is found in the Kaapvaal craton (aside from a discontinuity at 30 kilometers for station CKGRV). For both stations, I find a prominent discontinuity at 11 (CKGRV) and at 10-14 kilometers (PHDHD). This discontinuity is interpreted as the Conrad discontinuity in both cases. Both stations show a discontinuity at 38-39 kilometers. It is likely that this discontinuity is the same as what is found in the Kaapvaal craton and thus the result from mafic material building up from below. It is possible that this happened during the original rifting phase and the emplacement of the Kgwebe formation in the Proterozoic (Modie, 2000). Station CKGRV also has a discontinuity at around 53 kilometers. Fadel et al. (2018) also find two discontinuities. Initially, their model indicated a crustal thickness of more than 49 kilometers and a Vp/Vs ratio lower than 1.65, which would be unrealistically low. By reducing the depth range, they found a crustal thickness of 37 kilometers. Based on my

results, I think that both of these discontinuities might actually exist.

Station PHDHD appears to show the Moho discontinuity at 43 kilometers, although this discontinuity is not as well resolved. This can be seen in the smoothness of the mean model and the relatively low amplitude and wide spread of the histogram in figure 41b. Nevertheless, analysis shows that in our models, the 4.2 km/s threshold is exceeded at approximately 43 kilometers.

## 5.11 Damara belt

### 5.11.1 SLIND

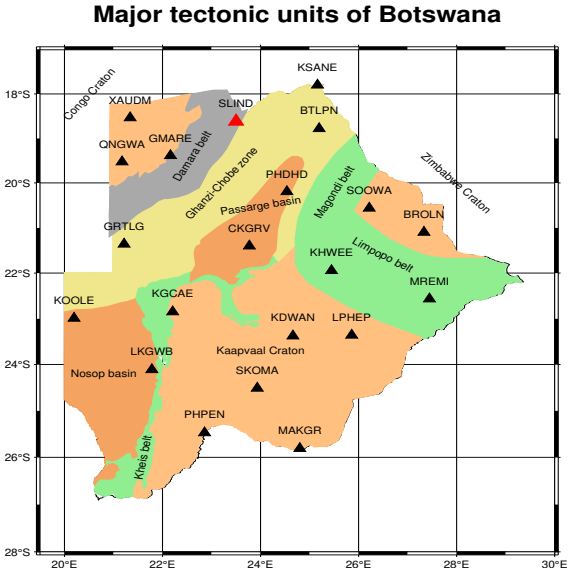


Figure 42: Tectonic map indicating station SLIND in red.

Station SLIND is located in the northwestern part of the Damara belt. The receiver functions for this station were of poor quality with very strong near surface reverberations. In order to limit the effects of these reverberations I have lowered the Gaussian width to 0.1 Hz. Making the Gaussian width smaller also allowed for a reduction of the sampling frequency, this was reduced to 2 Hz. This removed most of the near surface reverberations. However, as a side effect, this causes smoothing of the model, which is very well visible in figure 43. Two different inversions were carried out for this station, one with a receiver function with a slowness of 7.1 s/° with a back azimuth of 135.1° (table 46), and one with a slowness of 7.7 s/° with a back azimuth of 285.2° (table 47). The combined inversion results are shown in figure 43.

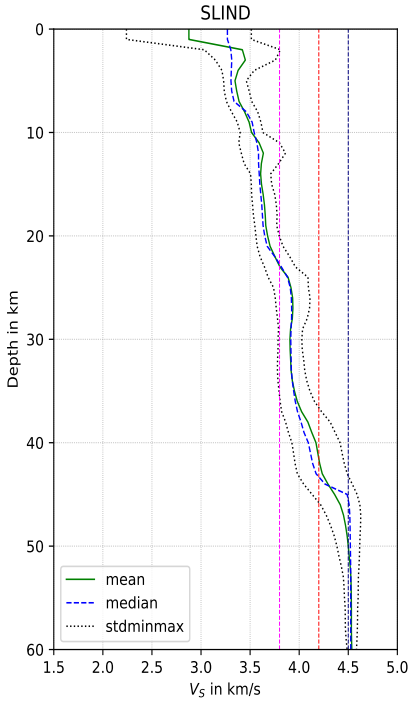


(a) Similar to figure 9a the mean and median velocity models with standard deviation for station SLIND.

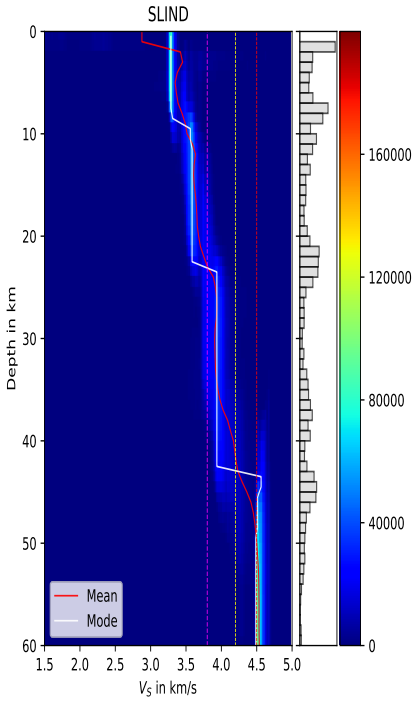


(b) Similar to figure 9b the mean and mode velocity models within the posterior Vs distribution for station SLIND.

Figure 43: 1D velocity models of the inversions for station SLIND. The vertical lines in both panels give the 3.8 km/s, 4.2 km/s and 4.5 km/s thresholds. The used events are given in tables 46 and 47 (2 events)

As said before, the velocity models for this station are very smooth and discontinuities are not well resolved. From figure 43b, we can see 4 likely discontinuities below this station. One at around 2 kilometers depth, one at around 10 kilometers depth, one at around 23 kilometers depth and one at around 43 kilometers depth.

For this station, I found a crustal thickness of around 44 kilometers. This is quite a bit thicker than the 38 kilometers found by Fadel et al. (2018).

### 5.11.2 GMARE

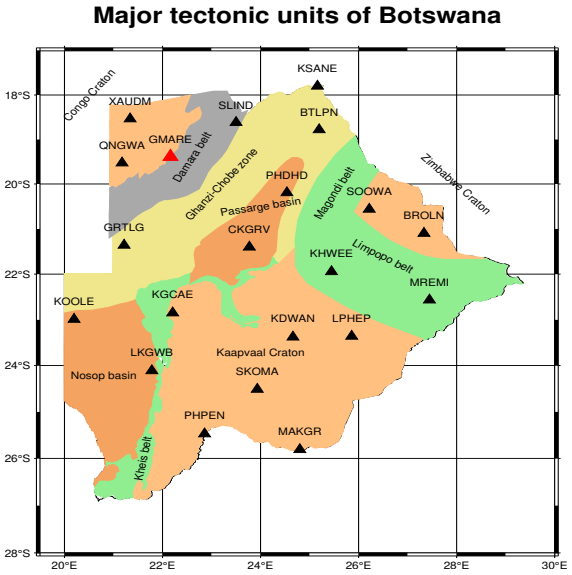


Figure 44: Tectonic map indicating station GMARE in red.

Station GMARE is located in the central part of the Damara belt. The receiver functions for this station were of poor quality.

Three different inversions were carried out for this station, one with a receiver function with a slowness of 5.7 s/° with a back azimuth of 38.5° (table 48), one with a slowness of 7.3 s/° with a back azimuth of 214.9 s/° (table 49) and one with a slowness of 7.9 s/° with a back azimuth of 51.9° (table 50). The combined inversion results are shown in figure 45.

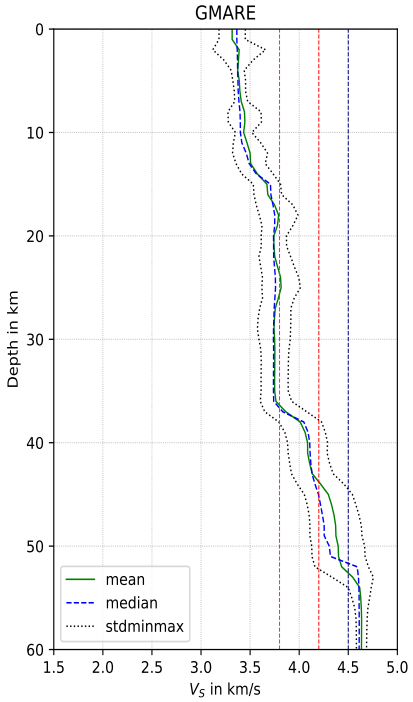


(a) Similar to figure 9a the mean and median velocity models with standard deviation for station GMARE.

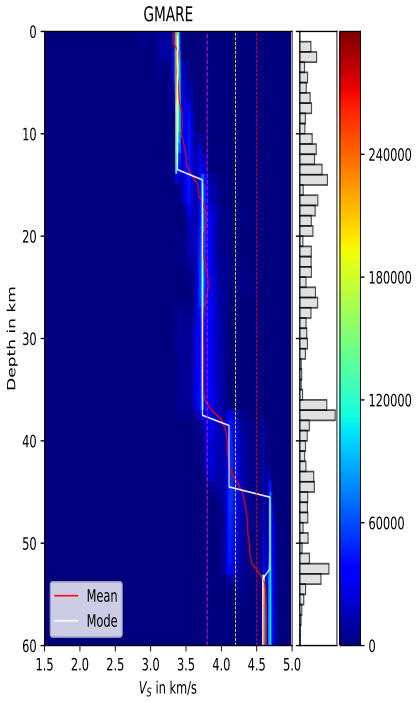


(b) Similar to figure 9b the mean and mode velocity models within the posterior Vs distribution for station GMARE.

Figure 45: 1D velocity models of the inversions for station GMARE. The vertical lines in both panels give the 3.8 km/s, 4.2 km/s and 4.5 km/s thresholds. The used events are given in tables 48, 49 and 50 (3 events)

The crust below station GMARE contains three major discontinuities. One at approximately 15 kilometers (although this one is not very well resolved), one at around 38 kilometers and one at around 53 kilometers.

For this station, I found a crustal thickness of around 45 kilometers which is comparable to the 44 kilometers found by Fadel et al. (2018). Station GMARE is close to the stations B09NK and B11ET from the SAFARI network. Yu, Liu, et al. (2015) found a crustal thickness of around 41.8 kilometers for station B09NK. Yu, Liu, et al. (2015) found 2 solutions for station B11ET, when using receiver functions with a back azimuth between 45° and 225°, they find a crustal thickness of 39.3 kilometers and a crustal thickness of 44.3 kilometers with receiver functions from all other directions. These differences are quite different from what I found which shows that this terrain is probably structurally complex.

## 5.12 Discussion Damara belt

Unfortunately, it proved to be difficult to resolve good models for this area. Station SLIND suffered from the strong shallow reverberations and receiver functions for station GMARE were not very consistent (figure 46).

For station SLIND (figure 43), I only looked at low frequency components of the signal. This station shows shows a large discontinuity at around 2 kilometers; this jump is most likely related to (possibly unconsolidated?) sediments. This model shows three more discontinuities, one at 10 kilometers, one at 23 kilometers and one at 43 kilometers. Both the 10 kilometer and 23 kilometer discontinuity could correlate to the Conrad discontinuity.

For station GMARE (figure 45) I find a fairly similar structure to what I found for station SLIND, just with the discontinuities at different depths. One discontinuity at 15 kilometers, one at 38 kilometers and one at 53 kilometers. The discontinuity at 15 kilometers is interpreted as the Conrad discontinuity. The structure in the Damara belt appears to be fairly similar to what we find in the Kaapvaal craton (section 5.1) and in the Limpopo belt for station KHWEE (figure 21). Because the age of these terrains is quite different (from Archean to Neoproterozoic) this could be an indication that the structure of two discontinuities in the lower part of the domain is younger than the tectonic terrains themselves. Therefore, the interpretation is similar as well.

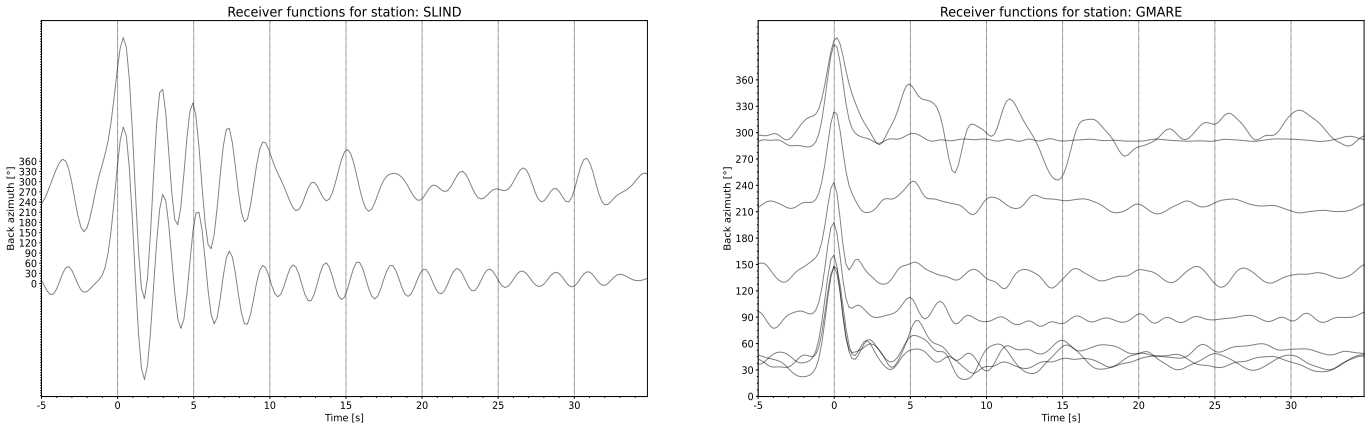


(a) Receiver functions for station SLIND, these receiver functions were calculated with a Gaussian width of 0.2 Hz illustrating the near surface reverberations.

(b) Receiver functions for station GMARE, these receiver functions were calculated with a Gaussian width of 0.2 Hz.

Figure 46: The receiver functions for the stations on the Damara belt.

## 5.13 Congo craton

### 5.13.1 XAUDM

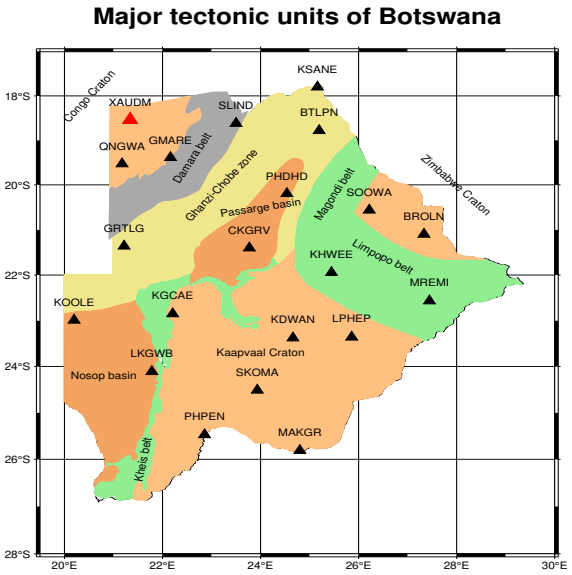


Figure 47: Tectonic map indicating station XAUDM in red.

Station XAUDM is located in the northwestern corner of Botswana on the Congo craton. The receiver functions for this station were of good quality but with a very strong back azimuth dependence. Therefore, the receiver functions for this station were binned based on back azimuth as well as slowness. Two different inversions were carried out for this station, one with a receiver function stack with an average slowness of 5.8 s/° with a back azimuth ranging between 39.1° and 54.2° (table 51), and one with an average slowness of 7.4 s/° with a back azimuth of 214.3° (table 52). The combined inversion results are shown in figure 48.

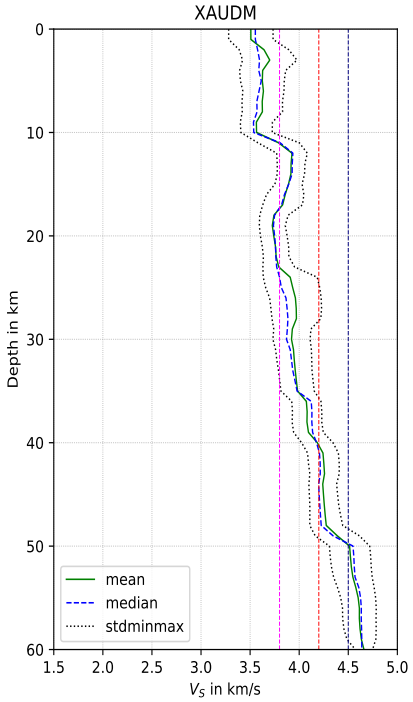


(a) Similar to figure 9a the mean and median velocity models with standard deviation for station XAUDM.

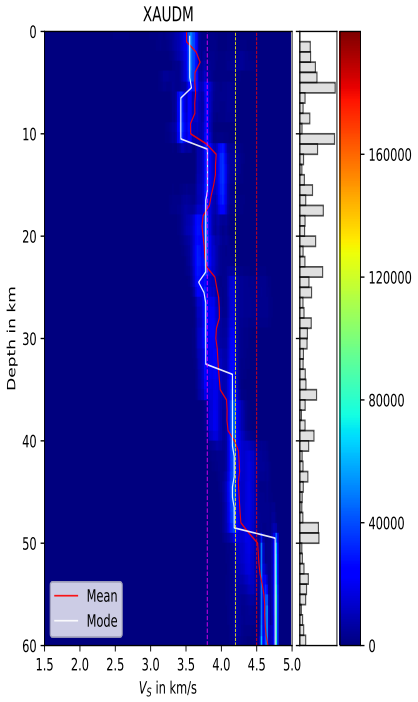


(b) Similar to figure 9b the mean and mode velocity models within the posterior Vs distribution for station XAUDM.

Figure 48: 1D velocity models of the inversions for station XAUDM. The vertical lines in both panels give the 3.8 km/s, 4.2 km/s and 4.5 km/s thresholds. The used events are given in tables 51 and 52 (7 events)

The back azimuth dependence of the receiver functions for this station expresses itself as a large uncertainty in the upper and mid crust as can be seen in the large standard deviation in figure 48a and the messy histogram in figure 48b. Consistent features are a pronounced discontinuity at approximately 11 kilometers and a discontinuity at approximately 49 kilometers. There also appears to be some discontinuity at around 40 kilometers. The 11 kilometer discontinuity is probably related to the Conrad discontinuity, similar to my interpretation for other stations.

For this station, I find a crustal thickness of around 40 kilometers which is somewhat thicker than the 38 kilometers found by Fadel et al. (2018). This station is relatively close to station B14MH. For this station, Yu, Liu, et al. (2015) found a crustal thickness of around 45.8 kilometers, which is significantly thicker than what Fadel et al. (2018) and I found. This difference can be explained by the fact that this station is very close to the Damara belt and might actually be on that terrain (Fadel et al., 2018).

### 5.13.2 QNGWA

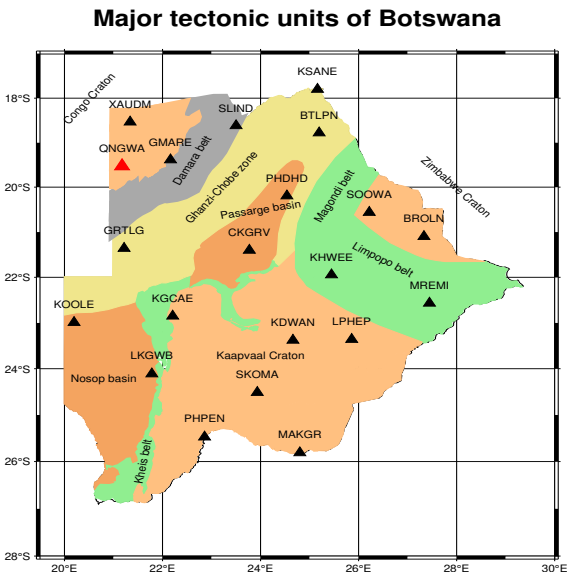


Figure 49: Tectonic map indicating station QNGWA in red.

Station QNGWA is located in the northwestern corner of Botswana on the Congo craton. The receiver functions for this station were of good quality. Two different inversions were carried out for this station, one with a receiver function stack with an average slowness of 5.8 s/° with a back azimuth ranging between 39.0° and 89.2° (table 53), and one with an average slowness of 7.5 s/° with a back azimuth ranging between 209.0° and 212.9° (table 54). The combined inversion results are shown in figure 50.

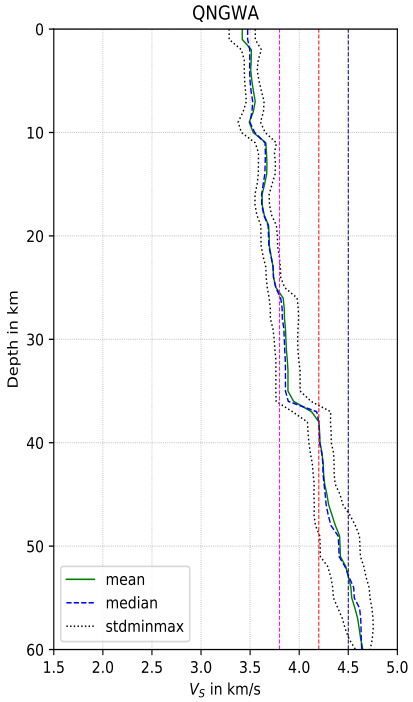


(a) Similar to figure 9a the mean and median velocity models with standard deviation for station QNGWA.

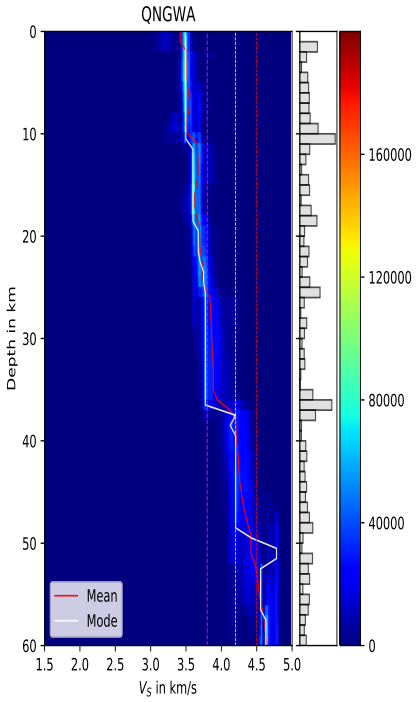


(b) Similar to figure 9b the mean and mode velocity models within the posterior Vs distribution for station QNGWA.

Figure 50: 1D velocity models of the inversions for station QNGWA. The vertical lines in both panels give the 3.8 km/s, 4.2 km/s and 4.5 km/s thresholds. The used events are given in tables 53 and 54 (8 events)

The models for this station are fairly well resolved and show two main discontinuities; one at 11 kilometers and one at approximately 37 kilometers. The mode in figure 50b also shows a pronounced discontinuity at 50 kilometers but the mean and median models do not show this feature, but the standard deviation becomes larger at these depths in figure 50a.

For this station, I found a crustal thickness of around 39 kilometers which is close to the 38 kilometers found by Fadel et al. (2018).

## 5.14 Discussion Congo craton

Compared to the neighbouring Damara belt, the data quality in the Congo craton was much higher. For station QNGWA, I find similar structures to what is found in the Kaapvaal craton. A discontinuity (although not as pronounced) at approximately 11 kilometers, a clear Moho discontinuity at 39 kilometers and a possible discontinuity at 50 kilometers. Similar again to what is found in the Kaapvaal craton, the deepest discontinuity is not as clear. I think the interpretation of the structure for this station is similar to the one made before, where the discontinuity at 11 kilometers depth corresponds to the Conrad discontinuity and the double discontinuity structure is caused by magmatic underplating of mafic material during the Karoo event.

The large back azimuth dependence for station XAUDM makes it hard to interpret the internal structure here. A feature that is consistently present are the discontinuities at 10 kilometers and at approximately 50 kilometers depth. The most interesting part about this station is the very strong dependence on back azimuth of the receiver functions (figure 51). Receiver functions from the north have a distinctive arrival at approximately 2.5 seconds. As back azimuth increases, this peak shifts to the left until it has completely merged with the first P-arrival at a back azimuth of 235°. This results in the large differences between the separate models (figure 75). Combining the models in figure 48 resulted in the enhancement of features that were consistent across models and in a larger standard deviation in depth ranges where this was not the case.

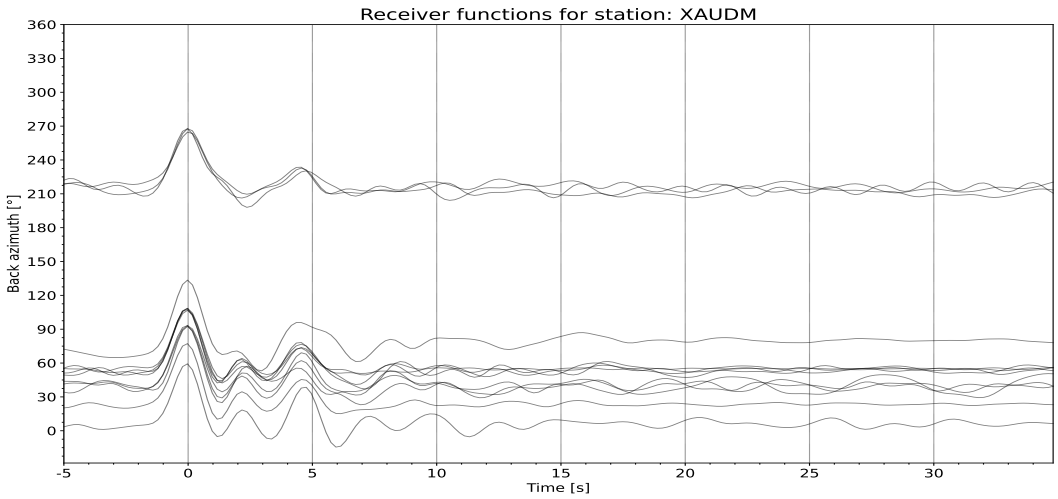


Figure 51: Receiver functions for station XAUDM to illustrate the back azimuth dependence. Not all receiver functions in this figure have been used in the inversion.

## 5.15 Discontinuity distribution

In order to visualize the spatial distribution of the three main discontinuities in this study, I have created three depth maps. These maps were made by interpolating between the stations. The Conrad discontinuity is shown in figure 52, the Moho is shown in figure 53 and the 50 kilometer discontinuity is shown in figure 54. Lastly, figure 55 shows the Vp/Vs distribution I found in Botswana.

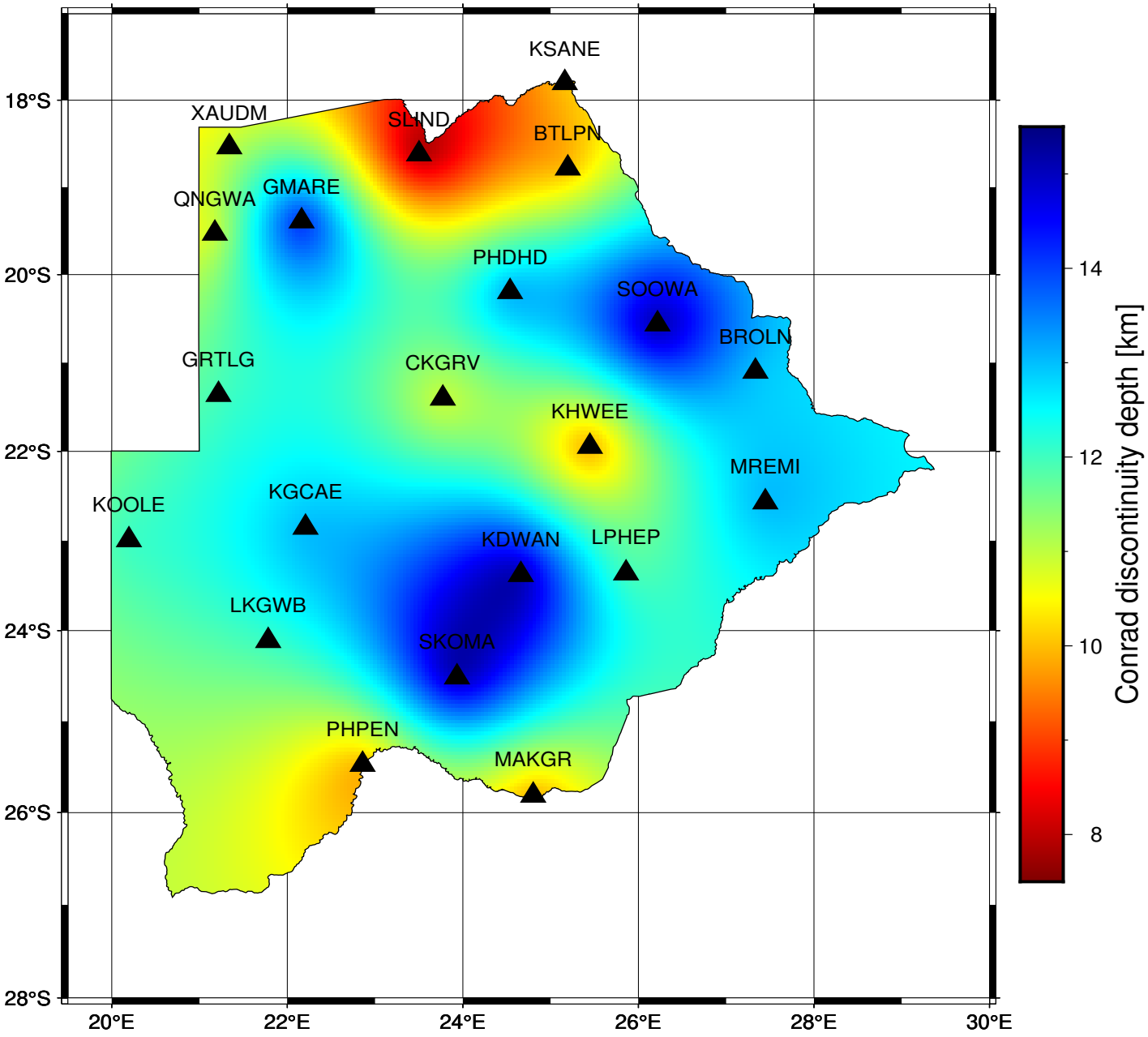


Figure 52: Interpolated Conrad discontinuity map. The used S-wave velocity threshold for this discontinuity was 3.8 km/s. This threshold was often crossed multiple times, aside from this, this threshold often remained within one standard deviation of the mean and median up to very large depths (deeper than 30 kilometers). Therefore, this discontinuity was picked by hand by inspecting the velocity models in section 5. The map was made by interpolating between the stations. Stations LKGWB and GRTLG were left out because no realistic estimate of the depth of the Conrad discontinuity could be made.

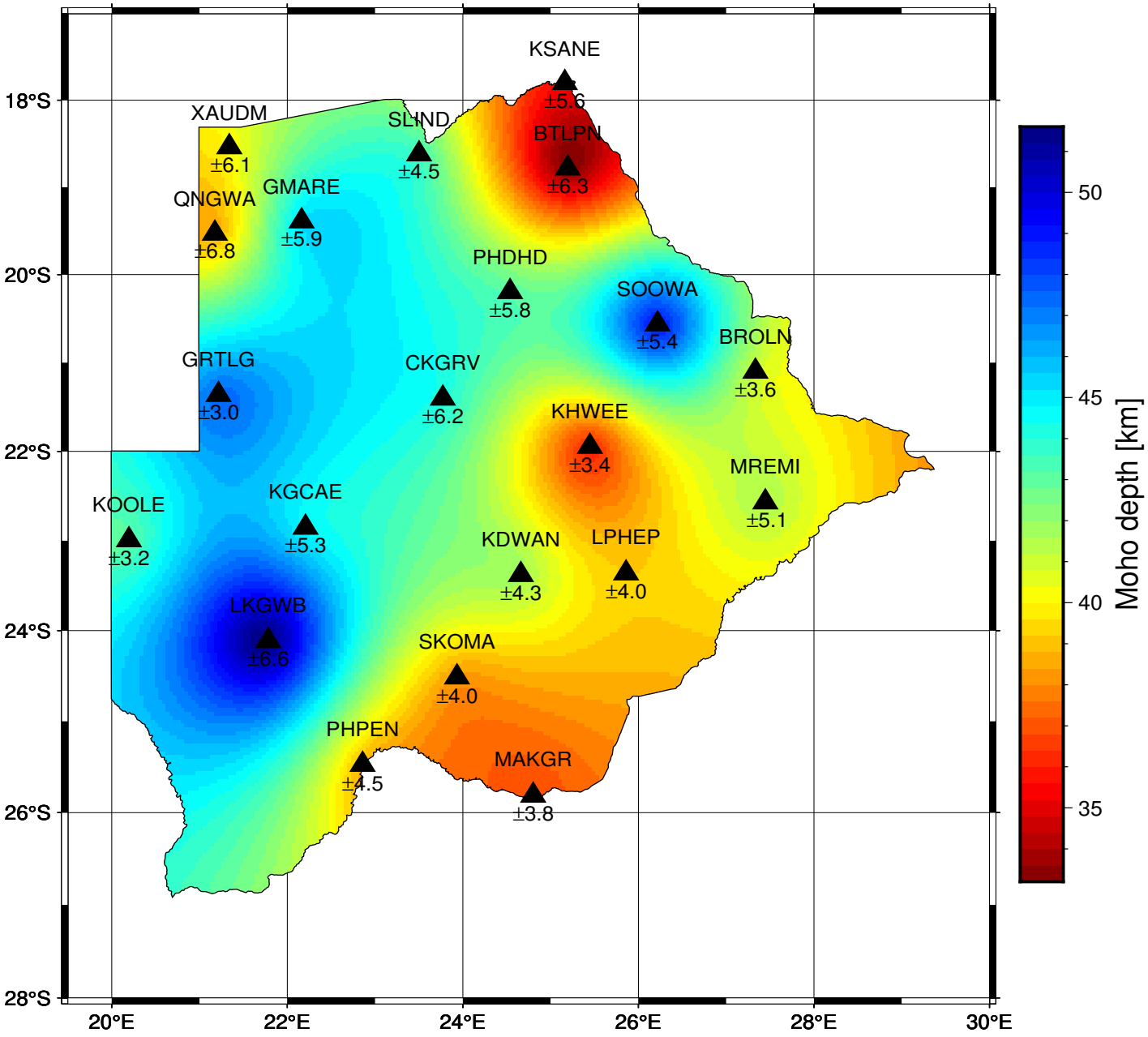


Figure 53: Interpolated crustal thickness map based on analysis of the combined posterior probability distribution. As a velocity threshold, a shear wave velocity of 4.2 km/s was used. The map was made by interpolating between all of the stations. Below the receiver positions, the uncertainty is plotted.

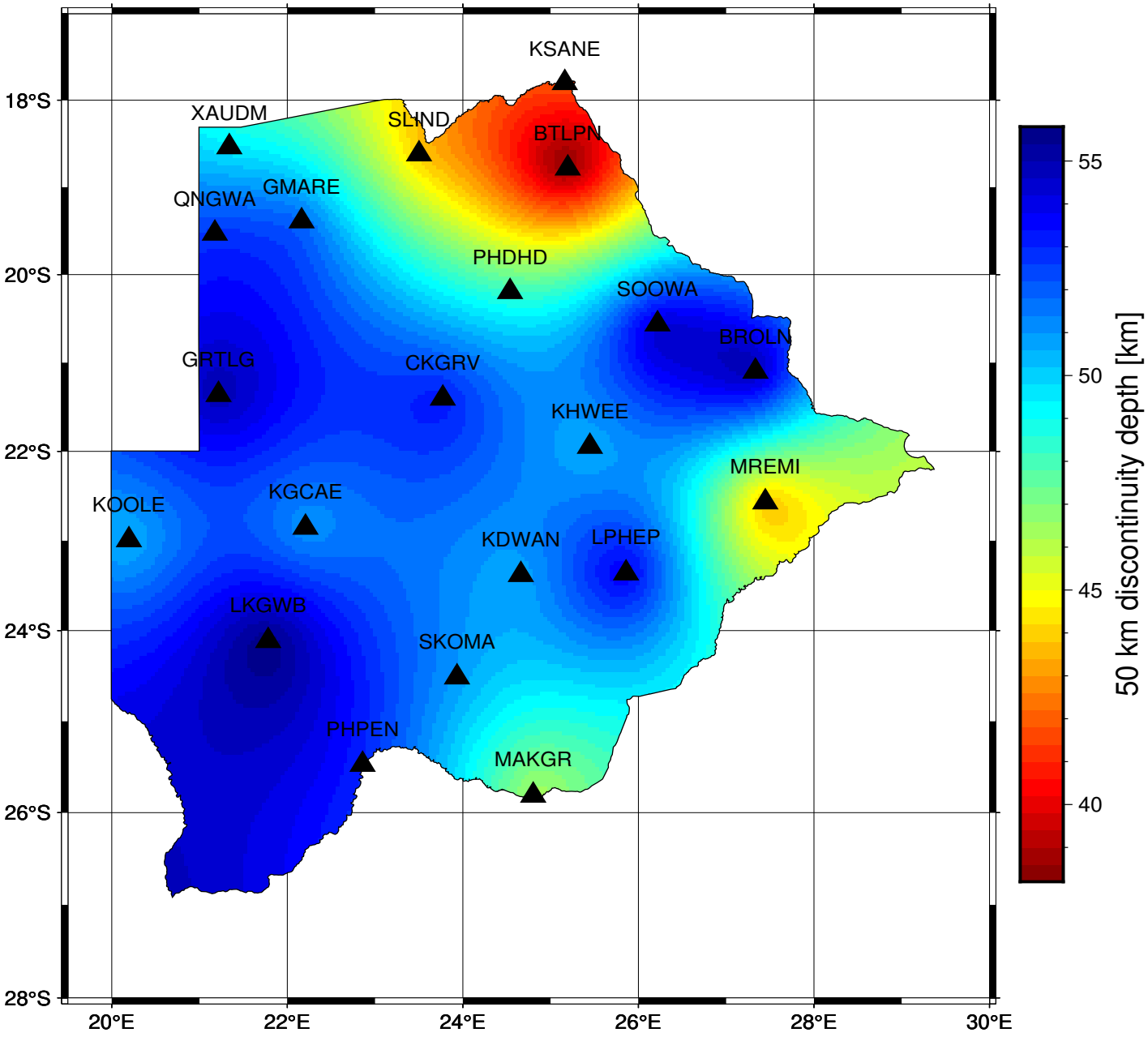


Figure 54: Interpolated 50 kilometer discontinuity map based on analysis of the combined posterior probability distribution. As a velocity threshold, a shear wave velocity of 4.5 km/s was used. The map was made by interpolating between all of the stations. The velocity models show that this boundary is often not a true discontinuity. Instead, it is a more gradual increase from a (nearly) constant velocity in the overlying layer.

First, the map in figure 52 shows a deepened Conrad discontinuity in the northern Kaapvaal craton and in the southwestern part of the Zimbabwe craton. It also shows a shallower Conrad discontinuity in the Okavango delta.

Second, the crust in northeast Botswana is relatively thin. In this region, the lower crustal discontinuity shown in figure 53 approximately coincides with the 50 kilometer discontinuity in figure 54. Slightly more to the southeast, we see the thickened crust in the Zimbabwe craton, this is also visible in both the thickness maps.

## 5.16 Vp/Vs ratio

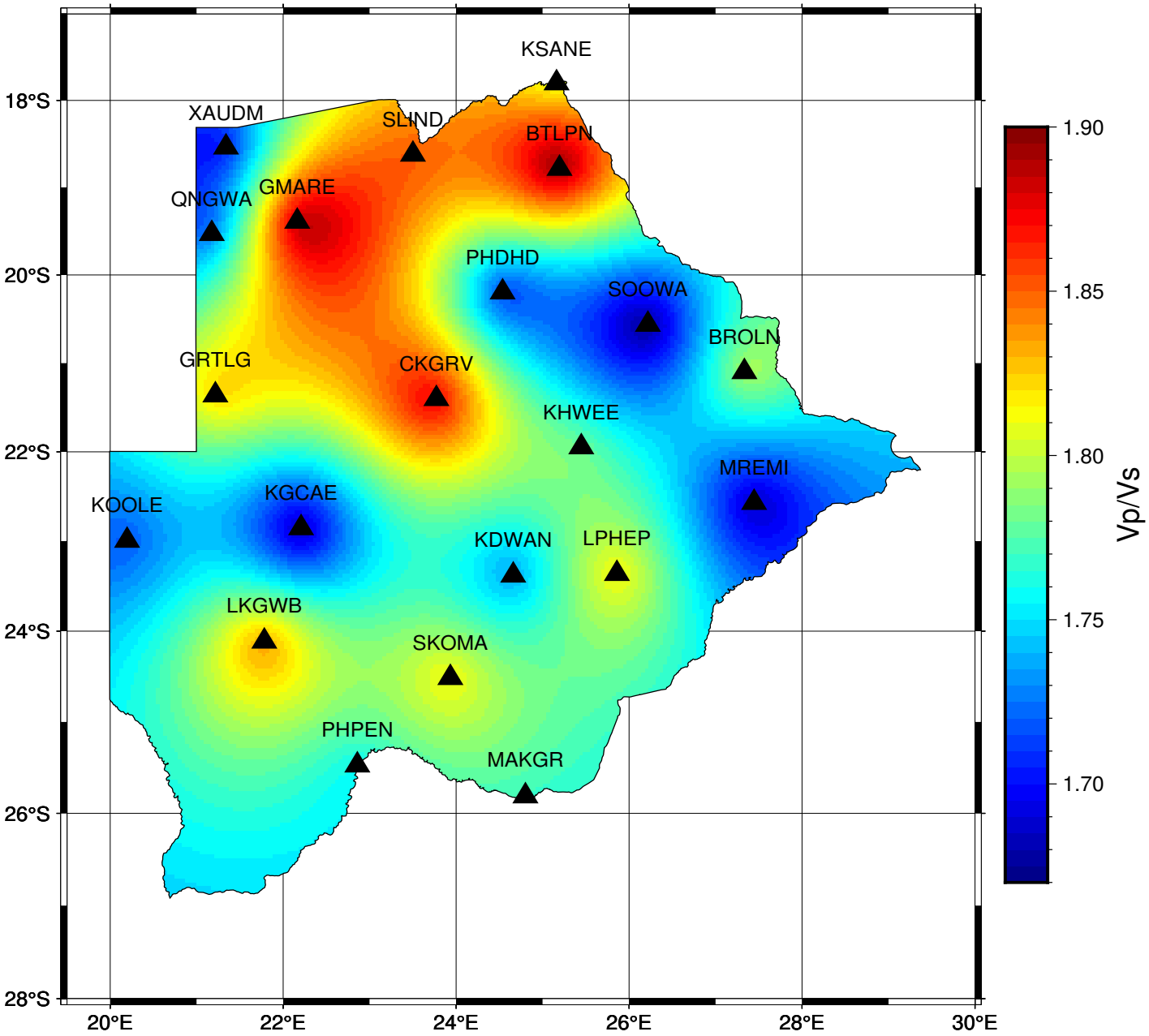


Figure 55: Interpolated map of the Vp/Vs ratio in Botswana. This map was made by analysing the combined posterior distribution and picking the median value as measurement at the station. The rest of the map was made by interpolating between the stations.

The Vp/Vs ratios solved for in this study are an average value for the entire model domain (surface to 60 kilometers depth). For this reason, it is not very insightful to compare these results to the results from Fadel et al. (2018), Youssof et al. (2013), and Yu, Gao, et al. (2015) as their Vp/Vs ratios are crustal averages and do not take the material below the Moho into account.

Vp/Vs ratios are relatively poorly resolved in this study. Nevertheless, I have tried to make a sensible interpretation. This is done by looking at the combined models presented in this section. The map in figure 55 shows a general division of high Vp/Vs ratios in northern Botswana, medium Vp/Vs ratios in the south and lower Vp/Vs ratios in the east and west. For some stations, there appears to be some correlation between the crustal thickness in figure 53 and the Vp/Vs ratio (although it is not a one to one correlation).

### 5.17 Summary and conclusions

I have shown that by jointly inverting receiver functions with phase velocity curves we are able to retrieve velocity depth models below the seismic stations of the Botswana Seismic Network. The most remarkable feature that we have found was the widespread 'double discontinuity' structure in the lower model domain with high (≈4.4 km/s) shear wave velocities in between. Because I find this structure in so many different terrains with varying age I think that this structure must be (significantly?) younger than the Precambrian basement. I think that this layer is a layer of mafic material that has underplated the crust after stabilization, potentially during the Karoo event (Jourdan et al., 2007). Thybo and Artemieva (2013) show how this process can occur in a variety of different tectonic settings. That means that, while cratonic areas have not undergone any significant deformation since the start of the Phanerozoic, they are not invulnerable to alteration from tectonothermal events like the Karoo volcanism event.

In general, the crustal thickness found in this study is similar to the one that Fadel et al. (2018) found (with only a few stations that are significantly different). The major difference between our studies is in the method. I jointly inverted receiver functions with phase velocity curves whereas they used the H-k method. The H-k method used by Fadel et al. (2018) relies on the assumption of a single layer crust and the picking of arrival times of different phases. The method I used relies on waveform modelling in which a model is proposed and a synthetic receiver function is calculated. The latter method is capable of modelling multiple layers while the first one is capable of modelling only the strongest discontinuity.

Furthermore, I have found a relatively thin crust in the northeast of the country in the Okavango delta, similar to what Fadel et al. (2018) and Fadel et al. (2020) found. This is probably caused by relatively recent rifting causing crustal thinning due to extension. We have also seen a widespread discontinuity at approximately 10 kilometers depth; this discontinuity is interpreted as the Conrad discontinuity and probably marks a transition from a felsic upper crust to a more intermediate middle crust. In general, the upper part of the model domain is better resolved than the lower part. This is likely caused by complexities hidden in the receiver functions which makes discontinuities hard to resolve. This is visible in the general lower amplitude of the histograms that describe the discontinuity distribution with depth in the lower part of the model domain.

Even though Vp/Vs ratios are poorly resolved in this study, the range of values that I found for this parameter were comparable to what Fadel et al. (2018) found. Unfortunately, there appears to be no correlation between my results and those of Fadel et al. (2018) for Vp/Vs. This could be caused by the fact that Fadel et al. (2018) only have crustal Vp/Vs ratios while in our study, part of the mantle is included. This makes using my Vp/Vs ratios harder to use for inferring crustal composition.

The disadvantage of the specific method that I have used is that it only allows for the inversion of a single receiver function. This approach neglects potential azimuthal variations and it does not include multiple slownesses. In order to do this it is desired to implement the possibility of inverting multiple receiver functions at once. In an attempt to address this problem, I have generated a single posterior from all of the different inversions for a single station. This is similar to averaging the inversions; which is, since the problem is non-linear, not the same as simultaneous inversion but instead produces an averaged structure. Dipping layers also pose a problem as is illustrated by the models for station XAUDM (figure 75). This arises from the assumptions we make about the angle of incidence; it is assumed that all the layers are horizontal. If this is not the case, the angle of incidence used for the modelling is wrong and this mostly affects the timing of the reverberations.

We can draw a few conclusions from my study:

1. The prominent double discontinuity structure in the lower part of the model domain is probably caused by mafic underplating during one of the numerous magmatic events that southern Africa has experienced.

2. The thin crust in the Okavango delta is probably a consequence of incipient rifting in the area.

3. Overprinting from several tectonothermal events probably has masked a lot of the structure from the Archean and Proterozoic.

## 6 Acknowledgments

I would like to thank my first supervisor Dr. Hanneke Paulssen for numerous fruitful discussions, providing extensive feedback and the evaluation of this work. I also want to thank my second supervisor Prof. Dr. Jeannot Trampert for evaluating my work. I also would like to thank Dr. Islam Fadel for providing the dispersion data that were used in the inversions and for providing the shapefiles that were used to create the tectonic map. Lastly, I want to thank Saskia Vos for proof reading this work. All the figures were made with Matplotlib and maps were made with GMT (Wessel et al., 2019).

# References


Abdelwahed, M. F., El-Khrepy, S., & Qaddah, A. (2013). Three-dimensional structure of Conrad and Moho discontinuities in Egypt. *Journal of African Earth Sciences*, *85*, 87–102. https://doi.org/10.1016/j.jafrearsci.2013.04.007

Adams, A., & Nyblade, A. (2011). Shear wave velocity structure of the southern African upper mantle with implications for the uplift of southern Africa. *Geophysical Journal International*, *186*(2), 808–824. https://doi.org/10.1111/j.1365-246X.2011.05072.x

Begg, G. C., Griffin, W. L., Natapov, L. M., O'Reilly, S. Y., Grand, S. P., O'Neill, C. J., Hronsky, J. M. A., Djomani, Y. P., Swain, C. J., Deen, T., & Bowden, P. (2009). The lithospheric architecture of africa: Seismic tomography, mantle petrology, and tectonic evolution. *Geosphere*, *5*(1), 23–50. https://doi.org/10.1130/GES00179.1

Beyreuther, M., Barsch, R., Krischer, L., Megies, T., Behr, Y., & Wassermann, J. (2010). Obspy: A python toolbox for seismology. *Seismological research letters*, *81*(3), 530–533. https://doi.org/10.1785/gssrl.81.3.530

Bodin, T., Sambridge, M., Gallagher, K., & Rawlinson, N. (2012). Transdimensional inversion of receiver functions and surface wave dispersion. *Journal of Geophysical Research: Solid Earth*, *117*(B2). https://doi.org/10.1029/2011JB008560

Botswana Geoscience Institute. (2001). Botswana seismological network. https://doi.org/10.7914/SN/BX

Chisenga, C., Van der Meijde, M., Yan, J., Fadel, I., Atekwana, E. A., Steffen, R., & Ramotoroko, C. (2020). Gravity derived crustal thickness model of botswana: Its implication for the m-w 6.5 april 3, 2017, botswana earthquake. *Tectonophysics*, *787*. https://doi.org/10.1016/j.tecto.2020.228479

Delph, J. R., & Porter, R. C. (2015). Crustal structure beneath southern africa: Insight into how tectonic events affect the mohorovicic discontinuity. *Geophysical Journal International*, *200*(1), 254–264. https://doi.org/10.1093/gji/ggu376

de Wit, M., Roering, C., Hart, R., Armstrong, R., de Ronde, C., Green, R., Tredoux, M., Peberdy, E., & Hart, R. (1992). Formation of an Archean continent. *Nature*, *357*(6379), 553–562. https://doi.org/10.1038/357553a0

Dreiling, J., & Tilmann, F. (2019). BayHunter - McMC transdimensional Bayesian inversion of receiver functions and surface wave dispersion. *GFZ Data Services*. https://doi.org/10.5880/GFZ.2.4.2019.001

Dreiling, J., Tilmann, F., Yuan, X., Haberland, C., & Seneviratne, S. W. M. (2020). Crustal Structure of Sri Lanka Derived From Joint Inversion of Surface Wave Dispersion and Receiver Functions Using a Bayesian Approach [e2019JB018688 10.1029/2019JB018688]. *Journal of Geophysical Research: Solid Earth*, *125*(5), e2019JB018688. https://doi.org/10.1029/2019JB018688

Durrheim, R., & Mooney, W. (1994). Evolution of the Precambrian lithosphere: Seismological and geochemical constraints. *Journal of Geophysical Research: Solid Earth*, *99*(B8), 15359–15374. https://doi.org/10.1029/94JB00138

Dziewonski, A., & Anderson, D. (1981). Preliminary reference earth model. *Physics of the Earth and Planetary Interiors*, *25*(4), 297–356. https://doi.org/10.1016/0031-9201(81)90046-7

Fadel, I., Paulssen, H., van der Meijde, M., Kwadiba, M., Ntibinyane, O., Nyblade, A., & Durrheim, R. (2020). Crustal and Upper Mantle Shear Wave Velocity Structure of Botswana: The 3 April 2017 Central Botswana Earthquake Linked to the East African Rift System [e2019GL085598 10.1029/2019GL085598]. *Geophysical Research Letters*, *47*(4), e2019GL085598. https://doi.org/10.1029/2019GL085598

Fadel, I., van der Meijde, M., & Paulssen, H. (2018). Crustal Structure and Dynamics of Botswana. *Journal of Geophysical Research: Solid Earth*, *123*(12), 10, 659–10, 671. https://doi.org/10.1029/2018JB016190

Gallagher, K., Charvin, K., Nielsen, S., Sambridge, M., & Stephenson, J. (2009). Markov chain monte carlo (mcmc) sampling methods to determine optimal models, model resolution and model choice for earth science problems [AAPG Hedberg Research Conference on Basin Modeling Perspectives - Innovative Developments and Novel Applications, The Hague, Netherlands, May, 2007]. *Marine and Petroleum Geology*, *26*(4), 525–535. https://doi.org/10.1016/j.marpetgeo.2009.01.003

Gore, J., James, D., Zengeni, T., & Gwavava, O. (2009). Crustal structure of the Zimbabwe craton and the Limpopo belt of Southern Africa: new constraints from seismic data and implications for its evolution. *South African Journal of Geology*, *112*(3-4), 213–228.

Haddon, I. G. (2005). The sub-kalahari geology and tectonic evolution of the kalahari basin, southern africa. *Unpublished Ph. D. thesis, University of the Witwatersrand, Johannesburg*.

Hatton, C. (1995). Mantle plume origin for the bushveld and ventersdorp magmatic provinces. *Journal of African Earth Sciences*, *21*(4), 571–577. https://doi.org/10.1016/0899-5362(95)00106-9

Jacobs, J., Pisarevsky, S., Thomas, R. J., & Beckere, T. (2008). The kalahari craton during the assembly and dispersal of rodinia. *Precambrian Research*, *160*(1-2), 142–158. https://doi.org/10.1016/j.precamres.2007.04.022

Jourdan, F., Bertrand, H., Schaerer, U., Blichert-Toft, J., Feraud, G., & Kampunzu, A. B. (2007). Major and trace element and sr, nd, hf and pb isotope compositions of the karoo large igneous province, botswana-zimbabwe: Lithosphere vs mantle plume contribution. *Journal of Petrology*, *48*(6), 1043–1077. https://doi.org/10.1093/petrology/egm010

Kampunzu, A., Tombale, A., Zhai, M., Bagai, Z., Majaule, T., & Modisi, M. (2003). Major and trace element geochemistry of plutonic rocks from francistown, ne botswana: Evidence for a neoarchaean continental active margin in the zimbabwe craton [Slave-Kaapvaal Workshop - Tale of Two Cratons, Merrickville, Canada, Sep 05-09, 2001]. *Lithos*, *71*(2-4), 431–460. https://doi.org/10.1016/S0024-4937(03)00125-7

Key, R., & Ayres, N. (2000). The 1998 edition of the national geological map of botswana [Conference for the 50th Anniversary of the Geological Survey of Botswana, Botswana, 1998]. *Journal of African Earth Sciences*, *30*(3), 427–451. https://doi.org/10.1016/S0899-5362(00)00030-0

Kgaswane, E. M., Nyblade, A. A., Julià, J., Dirks, P. H. G. M., Durrheim, R. J., & Pasyanos, M. E. (2009). Shear wave velocity structure of the lower crust in southern Africa: Evidence for compositional heterogeneity within Archaean and Proterozoic terrains. *Journal of Geophysical Research: Solid Earth*, *114*(B12). https://doi.org/10.1029/2008JB006217

Khoza, T. D., Jones, A. G., Muller, M. R., Evans, R. L., Miensopust, M. P., & Webb, S. J. (2013). Lithospheric structure of an archean craton and adjacent mobile belt revealed from 2-d and 3-d inversion of magnetotelluric data: Example from southern congo craton in northern namibia. *Journal of Geophysical Research: Solid Earth*, *118*(8), 4378–4397. https://doi.org/10.1002/jgrb.50258

Khoza, T. D., Jones, A. G., Muller, M. R., Evans, R. L., Webb, S. J., Miensopust, M., & Team, S. (2013). Tectonic model of the limpopo belt: Constraints from magnetotelluric data. *Precambrian Research*, *226*, 143–156. https://doi.org/10.1016/j.precamres.2012.11.016

Kroener, A., Brandl, G., Brandt, S., Klemd, R., & Xie, H. (2018). Geochronological evidence for archaean and palaeoproterozoic polymetamorphism in the central zone of the limpopo belt, south africa. *Precambrian Research*, *310*, 320–347. https://doi.org/10.1016/j.precamres.2018.03.013

Langston, C. A. (1979). Structure under Mount Rainier, Washington, inferred from teleseismic body waves. *Journal of Geophysical Research: Solid Earth*, *84*(B9), 4749–4762. https://doi.org/10.1029/JB084iB09p04749

Mahalanobis, P. C. (1936). On the generalized distance in statistics.

Majaule, T., Hanson, R., Key, R., Singletary, S., Martin, M., & Bowring, S. (2001). The Magondi belt in northeast Botswana: regional relations and new geochronological data from the Sua Pan area. *Journal of African Earth Sciences*, *32*(2), 257–267. https://doi.org/10.1016/S0899-5362(01)90006-5

Malory, A. O., Bao, X., & Chen, Z. (2022). Crustal shear wave velocity and radial anisotropy beneath southern africa from ambient noise tomography. *Tectonophysics*, *822*, 229191. https://doi.org/10.1016/j.tecto.2021.229191

Meghraoui, M., & Grp, I.-6. W. (2016). The seismotectonic map of africa. *Episodes*, *39*(1), 9–18. https://doi.org/10.18814/epiiugs/2016/v39i1/89232

Modie, B. (2000). Geology and mineralisation in the meso- to neoproterozoic ghanzi-chobe belt of northwest botswana [Conference for the 50th Anniversary of the Geological Survey of Botswana, Botswana, 1998]. *Journal of African Earth Sciences*, *30*(3), 467–474. https://doi.org/10.1016/S0899-5362(00)00032-4

Nguuri, T. K., Gore, J., James, D. E., Webb, S. J., Wright, C., Zengeni, T. G., Gwavava, O., Snoke, J. A., & Group, K. S. (2001). Crustal structure beneath southern Africa and its implications for the formation and evolution of the Kaapvaal and Zimbabwe cratons. *Geophysical Research Letters*, *28*(13), 2501–2504. https://doi.org/10.1029/2000GL012587

Owens, T. J., Zandt, G., & Taylor, S. R. (1984). Seismic evidence for an ancient rift beneath the cumberland plateau, tennessee: A detailed analysis of broadband teleseismic p waveforms. *Journal of Geophysical Research: Solid Earth*, *89*(B9), 7783–7795. https://doi.org/10.1029/JB089iB09p07783

Pastier, A.-M., Dauteuil, O., Murray-Hudson, M., Moreau, F., Walpersdorf, A., & Makati, K. (2017). Is the okavango delta the terminus of the east african rift system? towards a new geodynamic model: Geodetic study and geophysical review. *Tectonophysics*, *712*, 469–481. https://doi.org/10.1016/j.tecto.2017.05.035

Paulssen, H., Micallef, T., Bouwman, D. R., Ruigrok, E., Herman, M. W., Fadel, I., Meijde, M., Kwadiba, M., Maritinkole, J., & Ntibinyane, O. (2022). Rifting of the kalahari craton through botswana? new seismic evidence. *Journal of Geophysical Research-Solid Earth*, *127*(4). https://doi.org/10.1029/2021JB023524

Prendergast, M. D. (2012). The molopo farms complex, southern botswana - a reconsideration of structure, evolution, and the bushveld connection. *South African Journal of Geology*, *115*(1), 77–90. https://doi.org/10.2113/gssajg.115.1.77

Pretorius, D. A. (1984). *The kalahari foreland, its marginal troughs and overthrust belts, and the regional structure of botswana*. University of the Witwatersrand.

Rf: Receiver function calculation in seismology. (2020). https://doi.org/10.21105/joss.01808

Schmitz, M., & Bowring, S. (2003). Ultrahigh-temperature metamorphism in the lower crust during neoarchean ventersdorp rifting and magmatism, kaapvaal craton, southern africa. *Geological Society of America Bulletin*, *115*(5), 533–548. https://doi.org/10.1130/0016-7606(2003)115⟨0533:UMITLC⟩2.0.CO;2

Singletary, S. J., Hanson, R. E., Martin, M. W., Crowley, J. L., Bowring, S. A., Key, R. M., Ramokate, L. V., Direng, B. B., & Krol, M. A. (2003). Geochronology of basement rocks in the Kalahari Desert, Botswana, and implications for regional Proterozoic tectonics. *Precambrian Research*, *121*(1), 47–71. https://doi.org/10.1016/S0301-9268(02)00201-2

Thybo, H., & Artemieva, I. M. (2013). Moho and magmatic underplating in continental lithosphere. *Tectonophysics*, *609*(SI), 605–619. https://doi.org/10.1016/j.tecto.2013.05.032

Treloar, P. J. (1988). The geological evolution of the Magondi Mobile Belt, Zimbabwe. *Precambrian Research*, *38*(1), 55–73. https://doi.org/10.1016/0301-9268(88)90093-9

Utrecht-University. (2017). NARS Botswana (2013 – 2018). https://seismologie.sites.uu.nl/research-projects/nars/botswana/

Wessel, P., Luis, J. F., Uieda, L., Scharroo, R., Wobbe, F., Smith, W. H. F., & Tian, D. (2019). The generic mapping tools version 6. *Geochemistry, Geophysics, Geosystems*, *20*(11), 5556–5564. https://doi.org/10.1029/2019GC008515

Yang, B., Wang, Y., Zhao, L., Yang, L., & Sha, C. (2021). Depth variation of the conrad discontinuity in the qaidam basin, northwestern china, and its crustal dynamic implications. *Earth and Planetary Physics*, *5*(3), 296–304. https://doi.org/10.26464/epp2021030

Youssof, M., Thybo, H., Artemieva, I. M., & Levander, A. (2013). Moho depth and crustal composition in southern africa. *Tectonophysics*, *609*(SI), 267–287. https://doi.org/10.1016/j.tecto.2013.09.001

Yu, Y., Gao, S. S., Moidaki, M., Reed, C. A., & Liu, K. H. (2015). Seismic anisotropy beneath the incipient okavango rift: Implications for rifting initiation. *Earth and planetary science letters*, *430*, 1–8. https://doi.org/10.1016/j.epsl.2015.08.009

Yu, Y., Liu, K. H., Reed, C. A., Moidaki, M., Mickus, K., Atekwana, E. A., & Gao, S. S. (2015). A joint receiver function and gravity study of crustal structure beneath the incipient okavango rift, botswana. *Geophysical Research Letters*, *42*(20), 8398–8405. https://doi.org/10.1002/2015GL065811

Zhai, M., Kampunzu, A., Modisi, M., & Bagai, Z. (2006). Sr and nd isotope systematics of francistown plutonic rocks, botswana: Implications for neoarchaean crustal evolution of the zimbabwe craton. *International journal of Earth Sciences*, *95*(3), 355–369. https://doi.org/10.1007/s00531-005-0054-6

# A Events per inversion

Table 3: Events used for one inversion at station SKOMA. The average slowness is 5.5 s/°.

| Date | Time | Longitude [°E] | Latitude [°N] | Depth [km] | Magnitude | Baz [°] | Slowness [s/°] |
|---|---|---|---|---|---|---|---|
| 2015-04-26 | 07:09:09 | 85.98 | 27.74 | 13.4 | 6.7 | 52.9 | 5.46 |
| 2015-05-12 | 07:05:18 | 86.13 | 27.80 | 12.3 | 7.2 | 52.9 | 5.45 |

Table 4: Events used for one inversion at station SKOMA. The average slowness is 7.7 s/°.

| Date | Time | Longitude [°E] | Latitude [°N] | Depth [km] | Magnitude | Baz [°] | Slowness [s/°] |
|---|---|---|---|---|---|---|---|
| 2014-06-29 | 07:52:56 | -28.40 | -55.48 | 15.10 | 6.8 | 216.6 | 7.67 |
| 2017-05-10 | 23:23:37 | -25.78 | -56.43 | 17.39 | 6.5 | 214.8 | 7.75 |
| 2018-12-11 | 02:26:32 | -26.47 | -58.60 | 164.66 | 7.1 | 212.2 | 7.61 |

Table 5: Events used for one inversion at station KGCAE. The average slowness is 5.5 s/°.

| Date | Time | Longitude [°E] | Latitude [°N] | Depth [km] | Magnitude | Baz [°] | Slowness [s/°] |
|---|---|---|---|---|---|---|---|
| 2015-04-25 | 06:11:26 | 84.72 | 28.13 | 13.4 | 7.9 | 53.0 | 5.49 |
| 2015-05-12 | 07:05:18 | 86.13 | 27.80 | 12.3 | 7.2 | 54.0 | 5.42 |
| 2016-12-06 | 22:03:33 | 96.17 | 5.28 | 13.0 | 6.5 | 78.8 | 5.59 |
| 2016-12-25 | 14:22:27 | -73.94 | -43.41 | 38.0 | 7.6 | 227.5 | 5.48 |
| 2021-01-19 | 02:46:22 | -68.81 | -31.83 | 20.0 | 6.4 | 239.9 | 5.47 |

Table 6: Events used for one inversion at station KGCAE. The average slowness is 7.5 s/°.

| Date | Time | Longitude [°E] | Latitude [°N] | Depth [km] | Magnitude | Baz [°] | Slowness [s/°] |
|---|---|---|---|---|---|---|---|
| 2015-12-04 | 22:25:00 | 85.09 | -47.62 | 35.00 | 7.1 | 133.0 | 7.21 |
| 2016-08-19 | 07:32:22 | -31.87 | -55.28 | 10.00 | 7.4 | 216.4 | 7.51 |
| 2018-12-11 | 02:26:32 | -26.47 | -58.60 | 164.66 | 7.1 | 211.0 | 7.56 |
| 2019-08-27 | 23:55:19 | -26.58 | -60.22 | 16.00 | 6.6 | 209.1 | 7.57 |
| 2021-03-14 | 12:05:13 | -29.47 | -59.88 | 10.00 | 6.0 | 210.3 | 7.49 |
| 2021-10-04 | 03:54:06 | -27.49 | -60.41 | 10.00 | 6.3 | 209.2 | 7.54 |

Table 7: Events used for one inversion at station KDWAN. The average slowness is 5.8 s/°.

| Date | Time | Longitude [°E] | Latitude [°N] | Depth [km] | Magnitude | Baz [°] | Slowness [s/°] |
|---|---|---|---|---|---|---|---|
| 2015-04-25 | 06:11:26 | 84.72 | 28.13 | 13.4 | 7.9 | 51.7 | 5.60 |
| 2015-10-26 | 09:09:42 | 70.37 | 36.52 | 231.0 | 7.5 | 37.0 | 5.81 |
| 2021-05-14 | 06:33:07 | 96.64 | 0.14 | 11.0 | 6.7 | 82.6 | 5.88 |

Table 8: Events used for one inversion at station KDWAN. The average slowness is 7.5 s/°.

| Date | Time | Longitude [°E] | Latitude [°N] | Depth [km] | Magnitude | Baz [°] | Slowness [s/°] |
|---|---|---|---|---|---|---|---|
| 2016-05-28 | 09:46:59 | -26.94 | -56.24 | 78.00 | 7.2 | 214.9 | 7.59 |
| 2016-08-19 | 07:32:22 | -31.87 | -55.28 | 10.00 | 7.4 | 217.1 | 7.45 |
| 2018-12-11 | 02:26:32 | -26.47 | -58.60 | 164.66 | 7.1 | 211.9 | 7.51 |
| 2021-08-12 | 18:36:59 | -26.43 | -59.98 | 35.00 | 6.7 | 210.2 | 7.53 |

Table 9: Events used for one inversion at station PHPEN. The average slowness is 5.5 s/°.

| Date | Time | Longitude [°E] | Latitude [°N] | Depth [km] | Magnitude | Baz [°] | Slowness [s/°] |
|---|---|---|---|---|---|---|---|
| 2016-12-25 | 14:22:27 | -73.94 | -43.41 | 38.0 | 7.6 | 227.7 | 5.58 |
| 2020-12-27 | 21:39:14 | -74.99 | -39.34 | 10.0 | 6.7 | 231.1 | 5.41 |
| 2021-01-19 | 02:46:22 | -68.81 | -31.83 | 20.0 | 6.4 | 240.2 | 5.53 |

Table 10: Events used for one inversion at station PHPEN. The average slowness is 6.7 s/°.

| Date | Time | Longitude [°E] | Latitude [°N] | Depth [km] | Magnitude | Baz [°] | Slowness [s/°] |
|---|---|---|---|---|---|---|---|
| 2013-11-25 | 06:27:34 | -54.96 | -53.97 | 10.0 | 6.9 | 220.4 | 6.68 |
| 2021-01-23 | 23:36:50 | -55.49 | -61.81 | 9.8 | 6.9 | 211.6 | 6.70 |

Table 11: Events used for one inversion at station PHPEN. The average slowness is 7.8 s/°.

| Date | Time | Longitude [°E] | Latitude [°N] | Depth [km] | Magnitude | Baz [°] | Slowness [s/°] |
|---|---|---|---|---|---|---|---|
| 2016-08-19 | 07:32:22 | -31.87 | -55.28 | 10.00 | 7.4 | 217.8 | 7.64 |
| 2017-05-10 | 23:23:37 | -25.78 | -56.43 | 17.39 | 6.5 | 215.0 | 7.85 |
| 2021-08-12 | 18:32:52 | -25.03 | -57.57 | 47.23 | 7.5 | 213.3 | 7.83 |
| 2022-01-25 | 01:24:33 | -28.78 | -55.37 | 11.00 | 6.0 | 217.1 | 7.76 |

Table 12: Events used for one inversion at station LPHEP. The average slowness is 6.7 s/°.

| Date | Time | Longitude [°E] | Latitude [°N] | Depth [km] | Magnitude | Baz [°] | Slowness [s/°] |
|---|---|---|---|---|---|---|---|
| 2014-05-24 | 09:25:03 | 25.37 | 40.28 | 8.2 | 6.9 | 359.6 | 6.63 |
| 2017-11-12 | 18:18:17 | 45.96 | 34.91 | 19.0 | 7.3 | 18.8 | 6.80 |
| 2017-12-01 | 02:32:46 | 57.31 | 30.74 | 9.0 | 6.1 | 30.7 | 6.75 |
| 2020-01-24 | 17:55:13 | 39.09 | 38.39 | 10.0 | 6.7 | 11.7 | 6.68 |
| 2021-01-23 | 23:36:50 | -55.49 | -61.81 | 9.8 | 6.9 | 210.9 | 6.47 |

Table 13: Events used for one inversion at station LPHEP. The average slowness is 7.5 s/°.

| Date | Time | Longitude [°E] | Latitude [°N] | Depth [km] | Magnitude | Baz [°] | Slowness [s/°] |
|---|---|---|---|---|---|---|---|
| 2014-06-29 | 07:52:56 | -28.40 | -55.48 | 15.10 | 6.8 | 216.4 | 7.53 |
| 2018-12-11 | 02:26:32 | -26.47 | -58.60 | 164.66 | 7.1 | 212.2 | 7.47 |
| 2019-04-09 | 17:53:59 | -25.26 | -58.61 | 44.83 | 6.5 | 211.9 | 7.56 |
| 2019-08-27 | 23:55:19 | -26.58 | -60.22 | 16.00 | 6.6 | 210.3 | 7.49 |
| 2021-08-12 | 18:32:52 | -25.03 | -57.57 | 47.23 | 7.5 | 213.1 | 7.60 |
| 2021-08-12 | 18:36:59 | -26.43 | -59.98 | 35.00 | 6.7 | 210.5 | 7.49 |

Table 14: Events used for one inversion at station MAKGR. The average slowness is 5.5 s/°.

| Date | Time | Longitude [°E] | Latitude [°N] | Depth [km] | Magnitude | Baz [°] | Slowness [s/°] |
|---|---|---|---|---|---|---|---|
| 2015-04-26 | 07:09:09 | 85.98 | 27.74 | 13.40 | 6.7 | 52.2 | 5.45 |
| 2015-05-12 | 07:05:18 | 86.13 | 27.80 | 12.30 | 7.2 | 52.3 | 5.43 |
| 2016-12-25 | 14:22:27 | -73.94 | -43.41 | 38.00 | 7.6 | 227.1 | 5.50 |
| 2019-08-02 | 12:03:27 | 104.82 | -7.27 | 52.76 | 6.9 | 92.4 | 5.55 |

Table 15: Events used for one inversion at station MAKGR. The average slowness is 6.7 s/°.

| Date | Time | Longitude [°E] | Latitude [°N] | Depth [km] | Magnitude | Baz [°] | Slowness [s/°] |
|---|---|---|---|---|---|---|---|
| 2013-11-25 | 06:27:34 | -54.96 | -53.97 | 10.0 | 6.9 | 220.4 | 6.61 |
| 2017-07-20 | 22:31:11 | 27.41 | 36.92 | 7.0 | 6.6 | 2.4 | 6.69 |
| 2017-11-12 | 18:18:17 | 45.96 | 34.91 | 19.0 | 7.3 | 19.3 | 6.61 |
| 2017-12-01 | 02:32:46 | 57.31 | 30.74 | 9.0 | 6.1 | 30.9 | 6.56 |
| 2021-01-23 | 23:36:50 | -55.49 | -61.81 | 9.8 | 6.9 | 211.6 | 6.66 |
| 2021-11-14 | 12:07:03 | 56.07 | 27.72 | 9.0 | 6.0 | 31.7 | 6.79 |
| 2022-01-11 | 01:07:48 | 31.95 | 35.23 | 21.0 | 6.6 | 6.7 | 6.79 |

Table 16: Events used for one inversion at station MAKGR. The average slowness is 7.7 s/°.

| Date | Time | Longitude [°E] | Latitude [°N] | Depth [km] | Magnitude | Baz [°] | Slowness [s/°] |
|---|---|---|---|---|---|---|---|
| 2014-06-29 | 07:52:56 | -28.40 | -55.48 | 15.10 | 6.8 | 217.5 | 7.71 |
| 2016-05-28 | 09:46:59 | -26.94 | -56.24 | 78.00 | 7.2 | 216.2 | 7.73 |
| 2017-05-10 | 23:23:37 | -25.78 | -56.43 | 17.39 | 6.5 | 215.7 | 7.79 |
| 2019-04-09 | 17:53:59 | -25.26 | -58.61 | 44.83 | 6.5 | 212.8 | 7.75 |
| 2020-07-26 | 00:53:59 | -25.41 | -60.78 | 10.00 | 6.4 | 210.1 | 7.70 |
| 2021-08-16 | 11:10:36 | -23.36 | -58.37 | 16.61 | 6.9 | 212.6 | 7.83 |
| 2021-08-22 | 21:33:20 | -24.88 | -60.29 | 14.00 | 7.1 | 210.6 | 7.73 |

Table 17: Events used for one inversion at station KHWEE. The average slowness is 6.8 s/°.

| Date | Time | Longitude [°E] | Latitude [°N] | Depth [km] | Magnitude | Baz [°] | Slowness [s/°] |
|---|---|---|---|---|---|---|---|
| 2020-01-24 | 17:55:13 | 39.09 | 38.39 | 10.0 | 6.7 | 12.2 | 6.77 |

Table 18: Events used for one inversion at station KHWEE. The average slowness is 7.0 s/°.

| Date | Time | Longitude [°E] | Latitude [°N] | Depth [km] | Magnitude | Baz [°] | Slowness [s/°] |
|---|---|---|---|---|---|---|---|
| 2017-07-20 | 22:31:11 | 27.41 | 36.92 | 7.00 | 6.6 | 1.8 | 6.97 |
| 2017-11-12 | 18:18:17 | 45.96 | 34.91 | 19.00 | 7.3 | 19.5 | 6.88 |
| 2020-05-02 | 12:51:06 | 25.71 | 34.20 | 16.99 | 6.6 | 0.3 | 7.17 |

Table 19: Events used for one inversion at station KHWEE. The average slowness is 7.5 s/°.

| Date | Time | Longitude [°E] | Latitude [°N] | Depth [km] | Magnitude | Baz [°] | Slowness [s/°] |
|---|---|---|---|---|---|---|---|
| 2015-12-04 | 22:25:00 | 85.09 | -47.62 | 35.00 | 7.1 | 133.7 | 7.32 |
| 2016-08-19 | 07:32:22 | -31.87 | -55.28 | 10.00 | 7.4 | 216.6 | 7.33 |
| 2017-05-10 | 23:23:37 | -25.78 | -56.43 | 17.39 | 6.5 | 213.9 | 7.54 |
| 2017-09-04 | 08:07:35 | -25.58 | -57.79 | 35.00 | 6.0 | 212.2 | 7.51 |
| 2019-04-09 | 17:53:59 | -25.26 | -58.61 | 44.83 | 6.5 | 211.2 | 7.49 |
| 2021-08-16 | 11:10:36 | -23.36 | -58.37 | 16.61 | 6.9 | 210.9 | 7.57 |

Table 20: Events used for one inversion at station MREMI. The average slowness is 5.8 s/°.

| Date | Time | Longitude [°E] | Latitude [°N] | Depth [km] | Magnitude | Baz [°] | Slowness [s/°] |
|---|---|---|---|---|---|---|---|
| 2016-11-25 | 14:24:30 | 74.02 | 39.23 | 17.0 | 6.6 | 35.7 | 5.75 |
| 2016-12-06 | 22:03:33 | 96.17 | 5.28 | 13.0 | 6.5 | 76.6 | 5.95 |

Table 21: Events used for one inversion at station MREMI. The average slowness is 6.8 s/°.

| Date | Time | Longitude [°E] | Latitude [°N] | Depth [km] | Magnitude | Baz [°] | Slowness [s/°] |
|---|---|---|---|---|---|---|---|
| 2017-06-12 | 12:28:39 | 26.37 | 38.92 | 12.0 | 6.3 | 359.0 | 6.79 |
| 2020-01-24 | 17:55:13 | 39.09 | 38.39 | 10.0 | 6.7 | 10.4 | 6.75 |

Table 22: Events used for one inversion at station MREMI. The average slowness is 7.4 s/°.

| Date | Time | Longitude [°E] | Latitude [°N] | Depth [km] | Magnitude | Baz [°] | Slowness [s/°] |
|---|---|---|---|---|---|---|---|
| 2016-05-28 | 09:46:59 | -26.94 | -56.24 | 78.00 | 7.2 | 215.2 | 7.44 |
| 2016-08-19 | 07:32:22 | -31.87 | -55.28 | 10.00 | 7.4 | 217.2 | 7.29 |
| 2017-05-10 | 23:23:37 | -25.78 | -56.43 | 17.39 | 6.5 | 214.7 | 7.50 |
| 2018-12-11 | 02:26:32 | -26.47 | -58.60 | 164.66 | 7.1 | 212.2 | 7.37 |
| 2019-04-09 | 17:53:59 | -25.26 | -58.61 | 44.83 | 6.5 | 211.9 | 7.46 |

Table 23: Events used for one inversion at station BROLN. The average slowness is 6.2 s/°.

| Date | Time | Longitude [°E] | Latitude [°N] | Depth [km] | Magnitude | Baz [°] | Slowness [s/°] |
|---|---|---|---|---|---|---|---|
| 2015-10-26 | 09:09:42 | 70.37 | 36.52 | 231.0 | 7.5 | 35.7 | 6.05 |
| 2016-03-02 | 12:49:48 | 94.33 | -4.95 | 24.0 | 7.8 | 86.4 | 6.37 |
| 2020-01-07 | 06:05:19 | 96.36 | 2.35 | 17.0 | 6.3 | 80.0 | 6.04 |
| 2021-01-23 | 23:36:50 | -55.49 | -61.81 | 9.8 | 6.9 | 210.4 | 6.28 |
| 2021-05-14 | 06:33:07 | 96.64 | 0.14 | 11.0 | 6.7 | 82.2 | 6.08 |

Table 24: Events used for one inversion at station BROLN. The average slowness is 7.3 s/°.

| Date | Time | Longitude [°E] | Latitude [°N] | Depth [km] | Magnitude | Baz [°] | Slowness [s/°] |
|---|---|---|---|---|---|---|---|
| 2015-11-17 | 07:10:07 | 20.60 | 38.67 | 11.00 | 6.5 | 353.9 | 6.89 |
| 2017-02-07 | 22:03:55 | 63.26 | 25.20 | 24.05 | 6.3 | 38.9 | 7.03 |
| 2017-07-20 | 22:31:11 | 27.41 | 36.92 | 7.00 | 6.6 | 0.1 | 7.04 |
| 2017-11-12 | 18:18:17 | 45.96 | 34.91 | 19.00 | 7.3 | 17.9 | 6.98 |
| 2020-01-24 | 17:55:13 | 39.09 | 38.39 | 10.00 | 6.7 | 10.6 | 6.86 |
| 2020-09-18 | 21:43:58 | -26.84 | 0.92 | 10.00 | 6.9 | 285.4 | 7.07 |
| 2020-10-30 | 11:51:27 | 26.79 | 37.92 | 21.00 | 7.0 | 359.5 | 6.96 |
| 2022-01-11 | 01:07:48 | 31.95 | 35.23 | 21.00 | 6.6 | 4.5 | 7.14 |

Table 25: Events used for one inversion at station SOOWA. The average slowness is 5.9 s/°.

| Date | Time | Longitude [°E] | Latitude [°N] | Depth [km] | Magnitude | Baz [°] | Slowness [s/°] |
|---|---|---|---|---|---|---|---|
| 2014-03-21 | 13:41:09 | 94.23 | 7.68 | 19.3 | 6.4 | 74.6 | 5.96 |
| 2015-05-12 | 07:05:18 | 86.13 | 27.80 | 12.3 | 7.2 | 52.4 | 5.75 |
| 2015-11-08 | 16:47:02 | 94.65 | 6.84 | 10.0 | 6.6 | 75.6 | 5.96 |
| 2016-12-06 | 22:03:33 | 96.17 | 5.28 | 13.0 | 6.5 | 77.7 | 5.90 |

Table 26: Events used for one inversion at station SOOWA. The average slowness is 7.3 s/°.

| Date | Time | Longitude [°E] | Latitude [°N] | Depth [km] | Magnitude | Baz [°] | Slowness [s/°] |
|---|---|---|---|---|---|---|---|
| 2016-08-19 | 07:32:22 | -31.87 | -55.28 | 10.00 | 7.4 | 216.2 | 7.22 |
| 2021-08-12 | 18:32:52 | -25.03 | -57.57 | 47.23 | 7.5 | 212.0 | 7.41 |

Table 27: Events used for one inversion at station SOOWA. The average slowness is 7.7 s/°.

| Date | Time | Longitude [°E] | Latitude [°N] | Depth [km] | Magnitude | Baz [°] | Slowness [s/°] |
|---|---|---|---|---|---|---|---|
| 2016-08-29 | 04:29:57 | -17.83 | -0.05 | 10.0 | 7.1 | 289.8 | 7.77 |
| 2022-02-08 | 11:59:26 | -19.88 | -0.40 | 10.0 | 6.2 | 288.1 | 7.65 |

Table 28: Events used for one inversion at station LKGWB. The average slowness is 5.6 s/°.

| Date | Time | Longitude [°E] | Latitude [°N] | Depth [km] | Magnitude | Baz [°] | Slowness [s/°] |
|---|---|---|---|---|---|---|---|
| 2014-03-21 | 13:41:09 | 94.23 | 7.68 | 19.3 | 6.4 | 75.7 | 5.6 |

Table 29: Events used for one inversion at station LKGWB. The average slowness is 5.6 s/°.

| Date | Time | Longitude [°E] | Latitude [°N] | Depth [km] | Magnitude | Baz [°] | Slowness [s/°] |
|---|---|---|---|---|---|---|---|
| 2016-12-25 | 14:22:27 | -73.94 | -43.41 | 38 | 7.6 | 227.8 | 5.57 |

Table 30: Events used for one inversion at station LKGWB. The average slowness is 7.8 s/°.

| Date | Time | Longitude [°E] | Latitude [°N] | Depth [km] | Magnitude | Baz [°] | Slowness [s/°] |
|---|---|---|---|---|---|---|---|
| 2021-08-12 | 18:32:52 | -25.03 | -57.57 | 47.23 | 7.5 | 212.3 | 7.79 |
| 2021-08-16 | 11:10:36 | -23.36 | -58.37 | 16.61 | 6.9 | 210.8 | 7.83 |

Table 31: Events used for one inversion at station KOOLE. The average slowness is 6.7 s/°.

| Date | Time | Longitude [°E] | Latitude [°N] | Depth [km] | Magnitude | Baz [°] | Slowness [s/°] |
|---|---|---|---|---|---|---|---|
| 2017-11-12 | 18:18:17 | 45.96 | 34.91 | 19.0 | 7.3 | 23.7 | 6.68 |
| 2020-01-24 | 17:55:13 | 39.09 | 38.39 | 10.0 | 6.7 | 16.5 | 6.61 |
| 2021-11-14 | 12:08:38 | 56.07 | 27.73 | 10.0 | 6.3 | 36.4 | 6.78 |

Table 32: Events used for one inversion at station KOOLE. The average slowness is 7.7 s/°.

| Date | Time | Longitude [°E] | Latitude [°N] | Depth [km] | Magnitude | Baz [°] | Slowness [s/°] |
|---|---|---|---|---|---|---|---|
| 2016-08-19 | 07:32:22 | -31.87 | -55.28 | 10.00 | 7.4 | 216.0 | 7.60 |
| 2018-12-11 | 02:26:32 | -26.47 | -58.60 | 164.66 | 7.1 | 210.5 | 7.64 |
| 2019-04-29 | 14:19:52 | 57.23 | 10.86 | 10.00 | 6.3 | 51.1 | 7.64 |
| 2021-08-12 | 18:32:52 | -25.03 | -57.57 | 47.23 | 7.5 | 211.3 | 7.77 |
| 2021-08-16 | 11:10:36 | -23.36 | -58.37 | 16.61 | 6.9 | 209.7 | 7.82 |

Table 33: Events used for one inversion at station KSANE. The average slowness is 7.1 s/°.

| Date | Time | Longitude [°E] | Latitude [°N] | Depth [km] | Magnitude | Baz [°] | Slowness [s/°] |
|---|---|---|---|---|---|---|---|
| 2017-11-12 | 18:18:17 | 45.96 | 34.91 | 19 | 7.3 | 20.6 | 7.16 |
| 2020-01-24 | 17:55:13 | 39.09 | 38.39 | 10 | 6.7 | 13.0 | 7.06 |

Table 34: Events used for one inversion at station KSANE. The average slowness is 7.1 s/°.

| Date | Time | Longitude [°E] | Latitude [°N] | Depth [km] | Magnitude | Baz [°] | Slowness [s/°] |
|---|---|---|---|---|---|---|---|
| 2016-08-19 | 07:32:22 | -31.87 | -55.28 | 10.0 | 7.4 | 214.9 | 7.1 |
| 2016-08-21 | 03:45:23 | -31.75 | -55.28 | 10.0 | 6.4 | 214.9 | 7.1 |

Table 35: Events used for one inversion at station KSANE. The average slowness is 7.3 s/°.

| Date | Time | Longitude [°E] | Latitude [°N] | Depth [km] | Magnitude | Baz [°] | Slowness [s/°] |
|---|---|---|---|---|---|---|---|
| 2016-05-28 | 09:46:59 | -26.94 | -56.24 | 78.00 | 7.2 | 212.6 | 7.24 |
| 2017-05-10 | 23:23:37 | -25.78 | -56.43 | 17.39 | 6.5 | 212.1 | 7.30 |
| 2019-04-05 | 16:14:16 | -27.86 | -55.92 | 58.60 | 6.4 | 213.2 | 7.22 |

Table 36: Events used for one inversion at station CKGRV. The average slowness is 5.7 s/°.

| Date | Time | Longitude [°E] | Latitude [°N] | Depth [km] | Magnitude | Baz [°] | Slowness [s/°] |
|---|---|---|---|---|---|---|---|
| 2015-04-25 | 06:11:26 | 84.72 | 28.13 | 13.4 | 7.9 | 52.5 | 5.64 |
| 2015-05-12 | 07:05:18 | 86.13 | 27.80 | 12.3 | 7.2 | 53.5 | 5.58 |
| 2015-10-26 | 09:09:42 | 70.37 | 36.52 | 231.0 | 7.5 | 37.9 | 5.89 |

Table 37: Events used for one inversion at station CKGRV. The average slowness is 7.4 s/°.

| Date | Time | Longitude [°E] | Latitude [°N] | Depth [km] | Magnitude | Baz [°] | Slowness [s/°] |
|---|---|---|---|---|---|---|---|
| 2019-08-27 | 23:55:19 | -26.58 | -60.22 | 16.0 | 6.6 | 209.0 | 7.43 |

Table 38: Events used for one inversion at station GRTLG. The average slowness is 5.5 s/°.

| Date | Time | Longitude [°E] | Latitude [°N] | Depth [km] | Magnitude | Baz [°] | Slowness [s/°] |
|---|---|---|---|---|---|---|---|
| 2015-04-25 | 06:11:26 | 84.72 | 28.13 | 13.4 | 7.9 | 53.7 | 5.50 |
| 2015-05-12 | 07:05:18 | 86.13 | 27.80 | 12.3 | 7.2 | 54.7 | 5.43 |
| 2016-12-06 | 22:03:33 | 96.17 | 5.28 | 13.0 | 6.5 | 79.5 | 5.55 |
| 2022-03-13 | 21:09:22 | 98.63 | -0.63 | 28.0 | 6.7 | 86.1 | 5.54 |

Table 39: Events used for one inversion at station GRTLG. The average slowness is 5.6 s/°.

| Date | Time | Longitude [°E] | Latitude [°N] | Depth [km] | Magnitude | Baz [°] | Slowness [s/°] |
|---|---|---|---|---|---|---|---|
| 2020-01-07 | 06:05:19 | 96.36 | 2.35 | 17.0 | 6.3 | 82.4 | 5.62 |
| 2021-05-14 | 06:33:07 | 96.64 | 0.14 | 11.0 | 6.7 | 84.6 | 5.66 |

Table 40: Events used for one inversion at station GRTLG. The average slowness is 6.9 s/°.

| Date | Time | Longitude [°E] | Latitude [°N] | Depth [km] | Magnitude | Baz [°] | Slowness [s/°] |
|---|---|---|---|---|---|---|---|
| 2017-11-12 | 18:18:17 | 45.96 | 34.91 | 19.0 | 7.3 | 23.2 | 6.82 |
| 2020-10-30 | 11:51:27 | 26.79 | 37.92 | 21.0 | 7.0 | 5.1 | 6.93 |
| 2022-01-11 | 01:07:48 | 31.95 | 35.23 | 21.0 | 6.6 | 10.4 | 7.07 |

Table 41: Events used for one inversion at station BTLPN. The average slowness is 5.9 s/°.

| Date | Time | Longitude [°E] | Latitude [°N] | Depth [km] | Magnitude | Baz [°] | Slowness [s/°] |
|---|---|---|---|---|---|---|---|
| 2015-12-07 | 07:50:05 | 72.78 | 38.21 | 22.0 | 7.2 | 37.7 | 5.98 |
| 2016-06-26 | 11:17:11 | 73.34 | 39.48 | 13.0 | 6.4 | 37.0 | 5.90 |

Table 42: Events used for one inversion at station BTLPN. The average slowness is 7.2 s/°.

| Date | Time | Longitude [°E] | Latitude [°N] | Depth [km] | Magnitude | Baz [°] | Slowness [s/°] |
|---|---|---|---|---|---|---|---|
| 2015-12-04 | 22:25:00 | 85.09 | -47.62 | 35.0 | 7.1 | 135.3 | 7.15 |
| 2016-08-19 | 07:32:22 | -31.87 | -55.28 | 10.0 | 7.4 | 215.3 | 7.16 |
| 2017-07-20 | 22:31:11 | 27.41 | 36.92 | 7.0 | 6.6 | 2.2 | 7.20 |

Table 43: Events used for one inversion at station PHDHD. The average slowness is 5.8 s/°.

| Date | Time | Longitude [°E] | Latitude [°N] | Depth [km] | Magnitude | Baz [°] | Slowness [s/°] |
|---|---|---|---|---|---|---|---|
| 2016-12-06 | 22:03:33 | 96.17 | 5.28 | 13.0 | 6.5 | 78.5 | 5.79 |

Table 44: Events used for one inversion at station PHDHD. The average slowness is 7.0 s/°.

| Date | Time | Longitude [°E] | Latitude [°N] | Depth [km] | Magnitude | Baz [°] | Slowness [s/°] |
|---|---|---|---|---|---|---|---|
| 2017-07-20 | 22:31:11 | 27.41 | 36.92 | 7.0 | 6.6 | 2.8 | 7.10 |
| 2017-11-12 | 18:18:17 | 45.96 | 34.91 | 19.0 | 7.3 | 20.6 | 6.98 |

Table 45: Events used for one inversion at station PHDHD. The average slowness is 7.3 s/°.

| Date | Time | Longitude [°E] | Latitude [°N] | Depth [km] | Magnitude | Baz [°] | Slowness [s/°] |
|---|---|---|---|---|---|---|---|
| 2016-08-19 | 07:32:22 | -31.87 | -55.28 | 10.0 | 7.4 | 215.7 | 7.27 |

Table 46: Events used for one inversion at station SLIND. The average slowness is 7.1 s/°.

| Date | Time | Longitude [°E] | Latitude [°N] | Depth [km] | Magnitude | Baz [°] | Slowness [s/°] |
|---|---|---|---|---|---|---|---|
| 2015-12-04 | 22:25:00 | 85.09 | -47.62 | 35.0 | 7.1 | 135.1 | 7.06 |

Table 47: Events used for one inversion at station SLIND. The average slowness is 7.7 s/°.

| Date | Time | Longitude [°E] | Latitude [°N] | Depth [km] | Magnitude | Baz [°] | Slowness [s/°] |
|---|---|---|---|---|---|---|---|
| 2017-11-30 | 06:32:50 | -23.43 | -1.08 | 10.0 | 6.5 | 285.2 | 7.65 |

Table 48: Events used for one inversion at station GMARE. The average slowness is 5.7 s/°.

| Date | Time | Longitude [°E] | Latitude [°N] | Depth [km] | Magnitude | Baz [°] | Slowness [s/°] |
|---|---|---|---|---|---|---|---|
| 2016-06-26 | 11:17:11 | 73.34 | 39.48 | 13.0 | 6.4 | 38.5 | 5.73 |

Table 49: Events used for one inversion at station GMARE. The average slowness is 7.3 s/°.

| Date | Time | Longitude [°E] | Latitude [°N] | Depth [km] | Magnitude | Baz [°] | Slowness [s/°] |
|---|---|---|---|---|---|---|---|
| 2016-08-19 | 07:32:22 | -31.87 | -55.28 | 10.0 | 7.4 | 214.9 | 7.31 |

Table 50: Events used for one inversion at station GMARE. The average slowness is 7.9 s/°.

| Date | Time | Longitude [°E] | Latitude [°N] | Depth [km] | Magnitude | Baz [°] | Slowness [s/°] |
|---|---|---|---|---|---|---|---|
| 2019-04-29 | 14:19:52 | 57.23 | 10.86 | 10.0 | 6.3 | 51.9 | 7.9 |

Table 51: Events used for one inversion at station XAUDM. The average slowness is 5.8 s/°.

| Date | Time | Longitude [°E] | Latitude [°N] | Depth [km] | Magnitude | Baz [°] | Slowness [s/°] |
|---|---|---|---|---|---|---|---|
| 2015-04-25 | 06:11:26 | 84.72 | 28.13 | 13.4 | 7.9 | 54.2 | 5.63 |
| 2015-10-26 | 09:09:42 | 70.37 | 36.52 | 231.0 | 7.5 | 39.8 | 5.95 |
| 2015-12-07 | 07:50:05 | 72.78 | 38.21 | 22.0 | 7.2 | 39.8 | 5.83 |
| 2016-06-26 | 11:17:11 | 73.34 | 39.48 | 13.0 | 6.4 | 39.1 | 5.74 |

Table 52: Events used for one inversion at station XAUDM. The average slowness is 7.4 s/°.

| Date | Time | Longitude [°E] | Latitude [°N] | Depth [km] | Magnitude | Baz [°] | Slowness [s/°] |
|---|---|---|---|---|---|---|---|
| 2016-08-19 | 07:32:22 | -31.87 | -55.28 | 10.00 | 7.4 | 214.3 | 7.29 |
| 2016-08-21 | 03:45:23 | -31.75 | -55.28 | 10.00 | 6.4 | 214.3 | 7.30 |
| 2017-05-10 | 23:23:37 | -25.78 | -56.43 | 17.39 | 6.5 | 211.3 | 7.49 |

Table 53: Events used for one inversion at station QNGWA. The average slowness is 5.8 s/°.

| Date | Time | Longitude [°E] | Latitude [°N] | Depth [km] | Magnitude | Baz [°] | Slowness [s/°] |
|---|---|---|---|---|---|---|---|
| 2016-03-02 | 12:49:48 | 94.33 | -4.95 | 24.0 | 7.8 | 89.2 | 5.96 |
| 2016-06-26 | 11:17:11 | 73.34 | 39.48 | 13.0 | 6.4 | 39.0 | 5.68 |

Table 54: Events used for one inversion at station QNGWA. The average slowness is 7.5 s/°.

| Date | Time | Longitude [°E] | Latitude [°N] | Depth [km] | Magnitude | Baz [°] | Slowness [s/°] |
|---|---|---|---|---|---|---|---|
| 2016-04-19 | 05:25:39 | -27.23 | -55.73 | 14.00 | 6.2 | 212.9 | 7.52 |
| 2016-05-28 | 09:46:59 | -26.94 | -56.24 | 78.00 | 7.2 | 212.2 | 7.49 |
| 2017-05-10 | 23:23:37 | -25.78 | -56.43 | 17.39 | 6.5 | 211.6 | 7.55 |
| 2018-12-11 | 02:26:32 | -26.47 | -58.60 | 164.66 | 7.1 | 209.4 | 7.40 |
| 2019-04-05 | 16:14:16 | -27.86 | -55.92 | 58.60 | 6.4 | 212.9 | 7.48 |
| 2019-04-09 | 17:53:59 | -25.26 | -58.61 | 44.83 | 6.5 | 209.0 | 7.49 |

# B Single inversion velocity models

## B.1 SKOMA

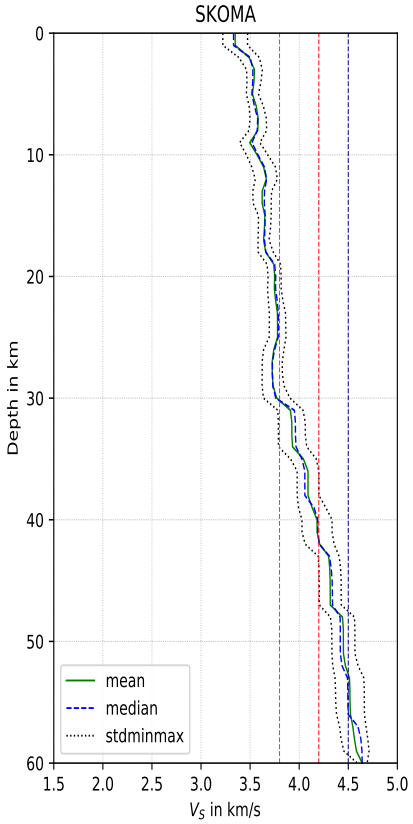


(a) Similar to figure 7b, the mean and median velocity models of inversion 1 at station SKOMA. The events for the receiver function stack are given in table 3 (2 events).

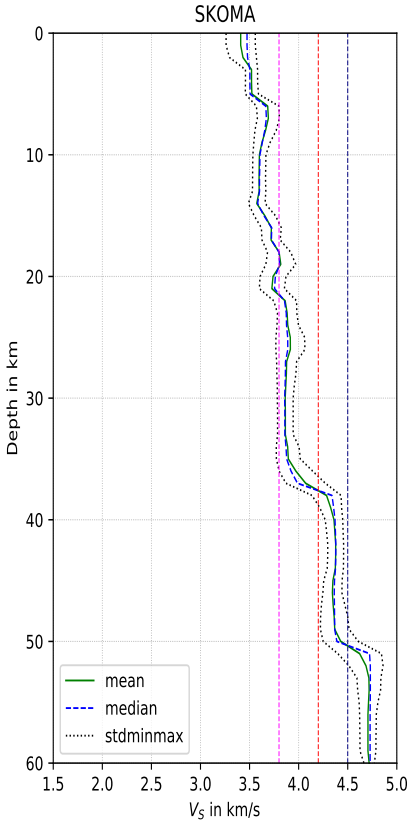


(b) Similar to figure 7b, the mean and median velocity models of inversion 1 at station SKOMA. The events for the receiver function stack are given in table 4 (3 events).

Figure 56: 1D velocity models of the inversions at station SKOMA. The left panel shows the mean and median models as well as the standard deviation of the inversion with a receiver function stack with a slowness of 5.5 s/°. The right panel shows the same for the inversion with a receiver function stack with a slowness of 7.7 s/°. The vertical lines in both panels give the 3.8 km/s, 4.2 km/s and 4.5 km/s thresholds.

## B.2 KGCAE

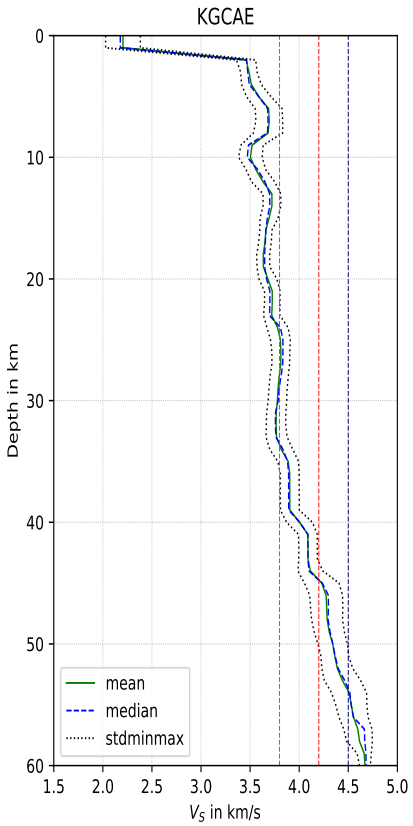


(a) Similar to figure 7b, the mean and median velocity models of inversion 1 at station KGCAE. The events for the receiver function stack are given in table 5 (5 events).

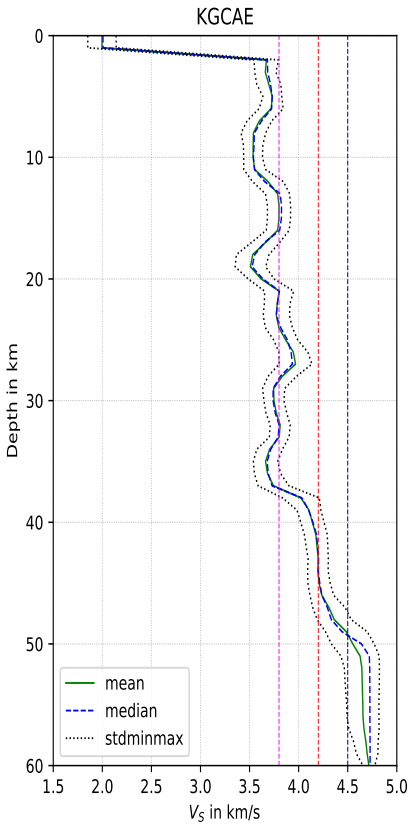


(b) Similar to figure 7b, the mean and median velocity models of inversion 1 at station KGCAE. The events for the receiver function stack are given in table 6 (6 events).

Figure 57: 1D velocity models of the inversions at station KGCAE. The left panel shows the mean and median models as well as the standard deviation of the inversion with a receiver function stack with a slowness of 5.5 s/°. The right panel shows the same for the inversion with a receiver function stack with a slowness of 7.5 s/°. The vertical lines in both panels give the 3.8 km/s, 4.2 km/s and 4.5 km/s thresholds.

## B.3 KDWAN

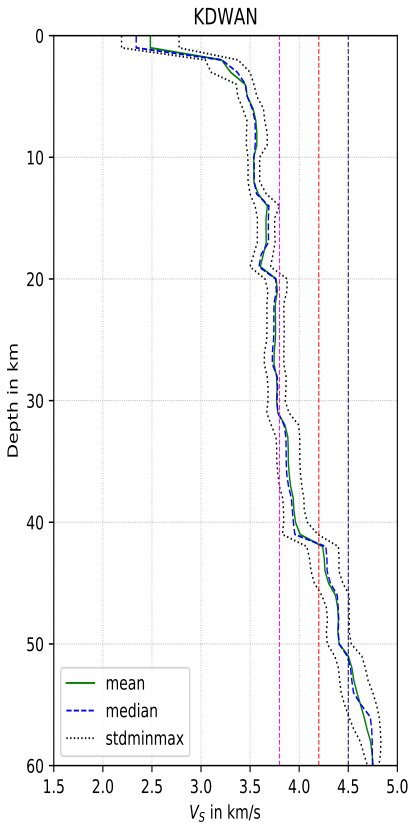


(a) Similar to figure 7b, the mean and median velocity models of inversion 1 at station KDWAN. The events for the receiver function stack are given in table 7 (3 events).

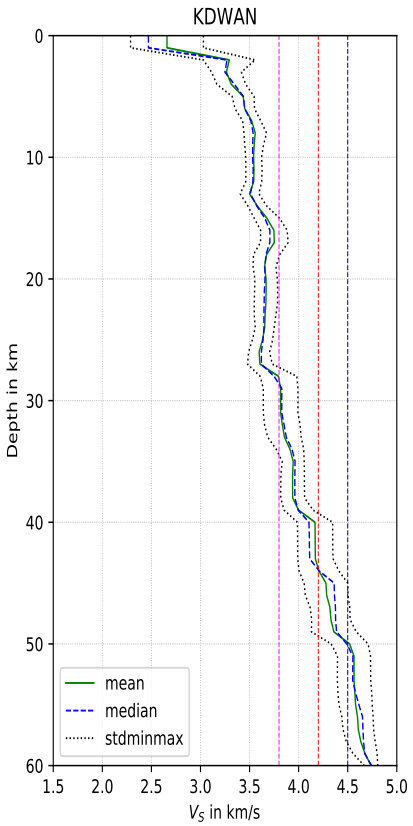


(b) Similar to figure 7b, the mean and median velocity models of inversion 1 at station KDWAN. The events for the receiver function stack are given in table 8 (4 events).

Figure 58: 1D velocity models of the inversions at station KDWAN. The left panel shows the mean and median models as well as the standard deviation of the inversion with a receiver function stack with a slowness of 5.8 s/°. The right panel shows the same for the inversion with a receiver function stack with a slowness of 7.5 s/°. The vertical lines in both panels give the 3.8 km/s, 4.2 km/s and 4.5 km/s thresholds.

## B.4 PHPEN

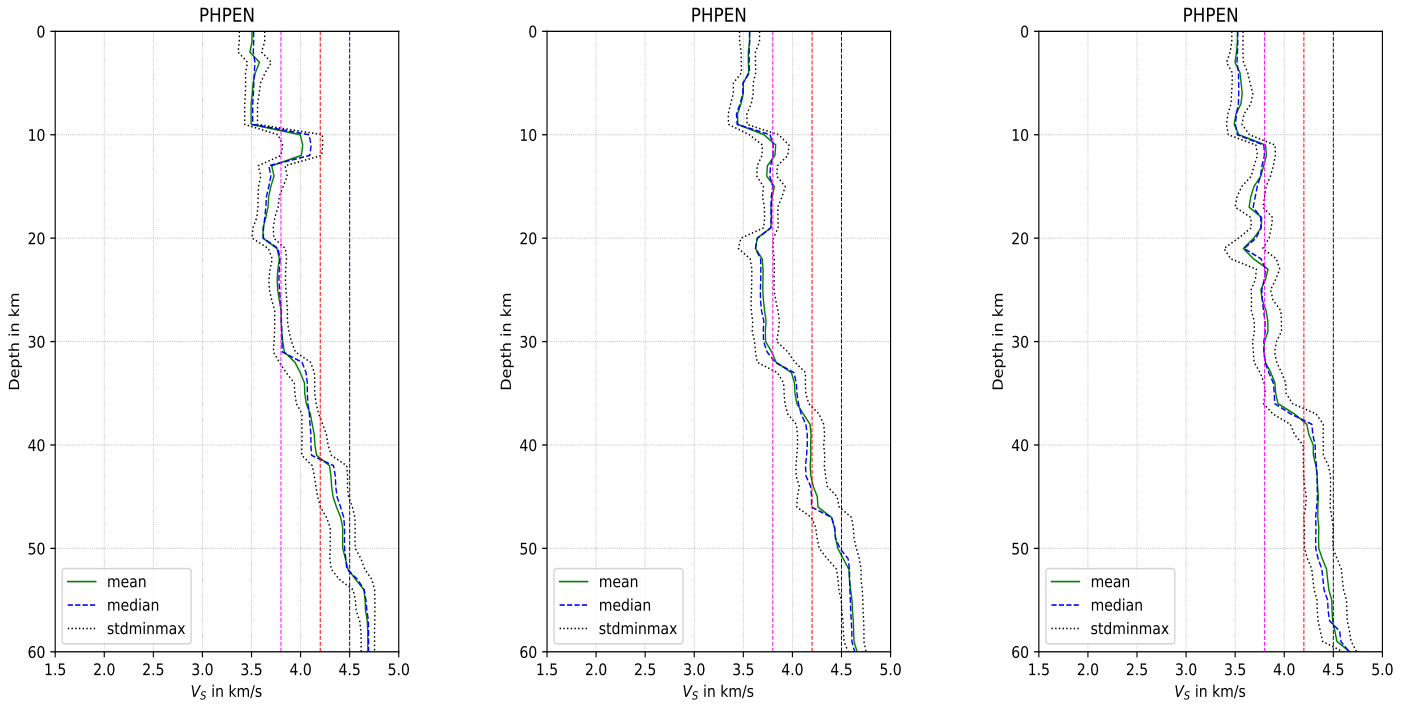


(a) Mean and median velocity models of inversion 1 at station PHPEN. The green line gives the mean velocity, the blue dashed line gives the median velocity and the dotted black lines give the standard deviation of the model. The events for the receiver function stack are given in table 9 (3 events).

(b) Mean and median velocity models of inversion 1 at station PHPEN. The green line gives the mean velocity, the blue dashed line gives the median velocity and the dotted black lines give the standard deviation of the model. The events for the receiver function stack are given in table 10 (2 events).

(c) Mean and median velocity models of inversion 1 at station PHPEN. The green line gives the mean velocity, the blue dashed line gives the median velocity and the dotted black lines give the standard deviation of the model. The events for the receiver function stack are given in table 11 (4 events).

Figure 59: 1D velocity models of the inversions at station PHPEN. The left panel shows the mean and median models as well as the standard deviation of the inversion with a receiver function stack with a slowness of 5.5 s/°. The middle panel shows the same for the inversion with a receiver function stack with a slowness of 6.7 s/°. The right panel shows the same for the inversion with a receiver function stack with a slowness of 7.8 s/°. The vertical lines in both panels give the 3.8 km/s, 4.2 km/s and 4.5 km/s thresholds.

## B.5 LPHEP

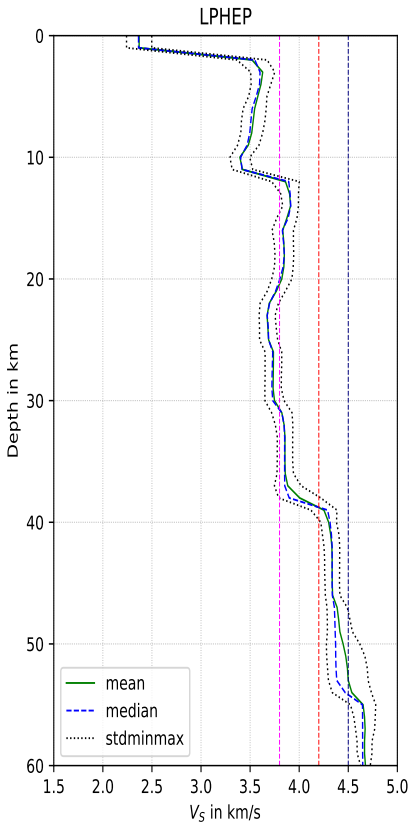


(a) Similar to figure 7b, the mean and median velocity models of inversion 1 at station LPHEP. The events for the receiver function stack are given in table 12 (5 events).

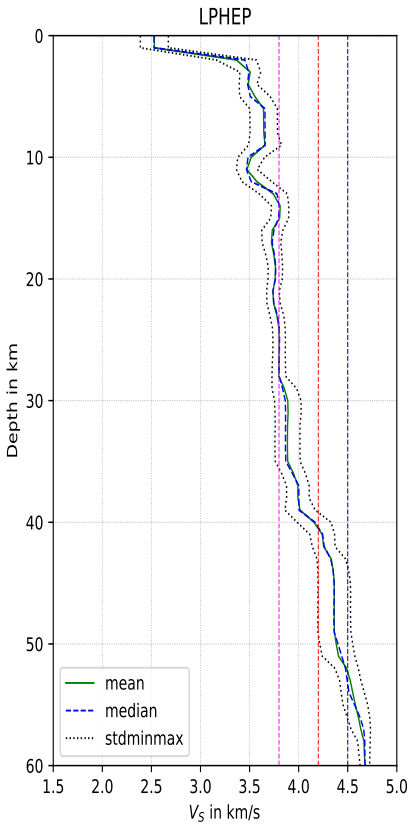


(b) Similar to figure 7b, the mean and median velocity models of inversion 1 at station KGCAE. The events for the receiver function stack are given in table 13 (6 events).

Figure 60: 1D velocity models of the inversions at station LPHEP. The left panel shows the mean and median models as well as the standard deviation of the inversion with a receiver function stack with a slowness of 6.7 s/°. The right panel shows the same for the inversion with a receiver function stack with a slowness of 7.5 s/°. The vertical lines in both panels give the 3.8 km/s, 4.2 km/s and 4.5 km/s thresholds.

## B.6 MAKGR

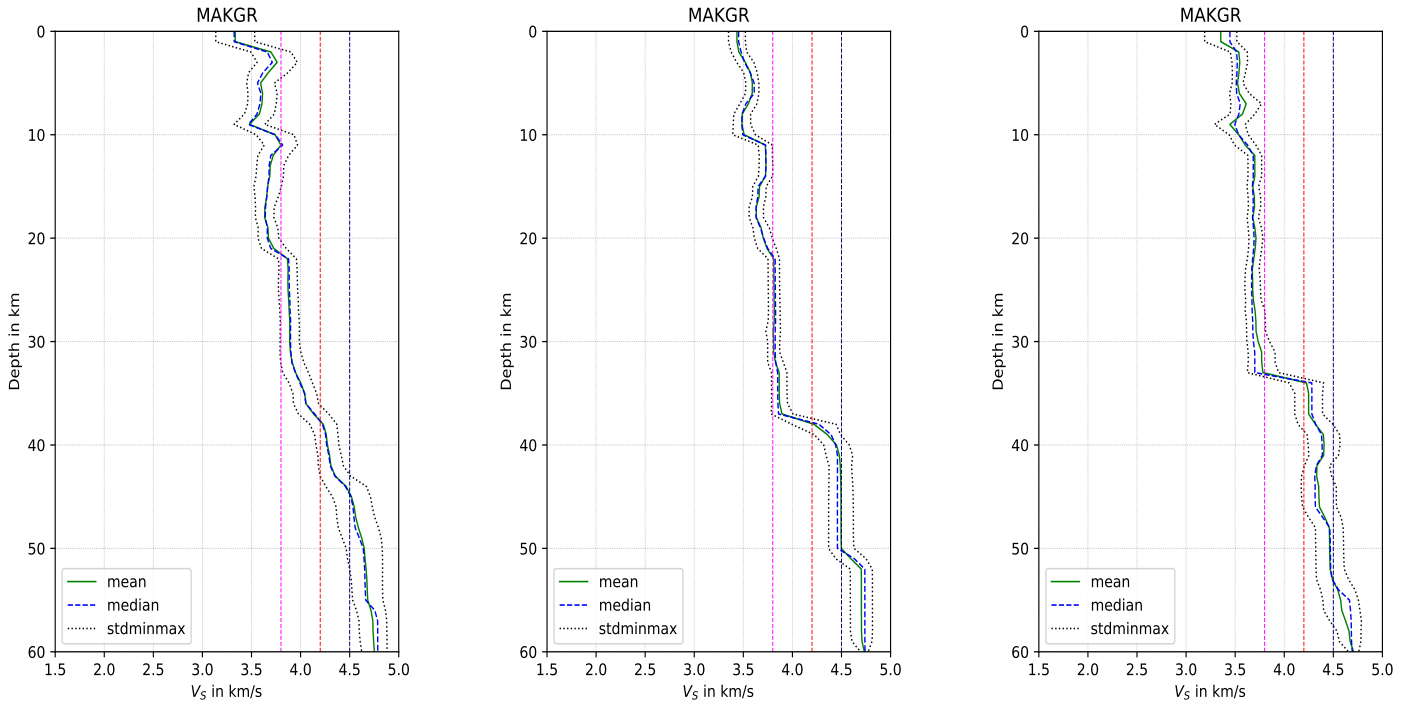


(a) Mean and median velocity models of inversion 1 at station MAKGR. The green line gives the mean velocity, the blue dashed line gives the median velocity and the dotted black lines give the standard deviation of the model. The events for the receiver function stack are given in table 14 (4 events).

(b) Mean and median velocity models of inversion 1 at station MAKGR. The green line gives the mean velocity, the blue dashed line gives the median velocity and the dotted black lines give the standard deviation of the model. The events for the receiver function stack are given in table 15 (7 events).

(c) Mean and median velocity models of inversion 1 at station MAKGR. The green line gives the mean velocity, the blue dashed line gives the median velocity and the dotted black lines give the standard deviation of the model. The events for the receiver function stack are given in table 16 (7 events).

Figure 61: 1D velocity models of the inversions at station MAKGR. The left panel shows the mean and median models as well as the standard deviation of the inversion with a receiver function stack with a slowness of 5.5 s/°. The middle panel shows the same for the inversion with a receiver function stack with a slowness of 6.7 s/°. The right panel shows the same for the inversion with a receiver function stack with a slowness of 7.7 s/°. The vertical lines in both panels give the 3.8 km/s, 4.2 km/s and 4.5 km/s thresholds.

## B.7 KHWEE

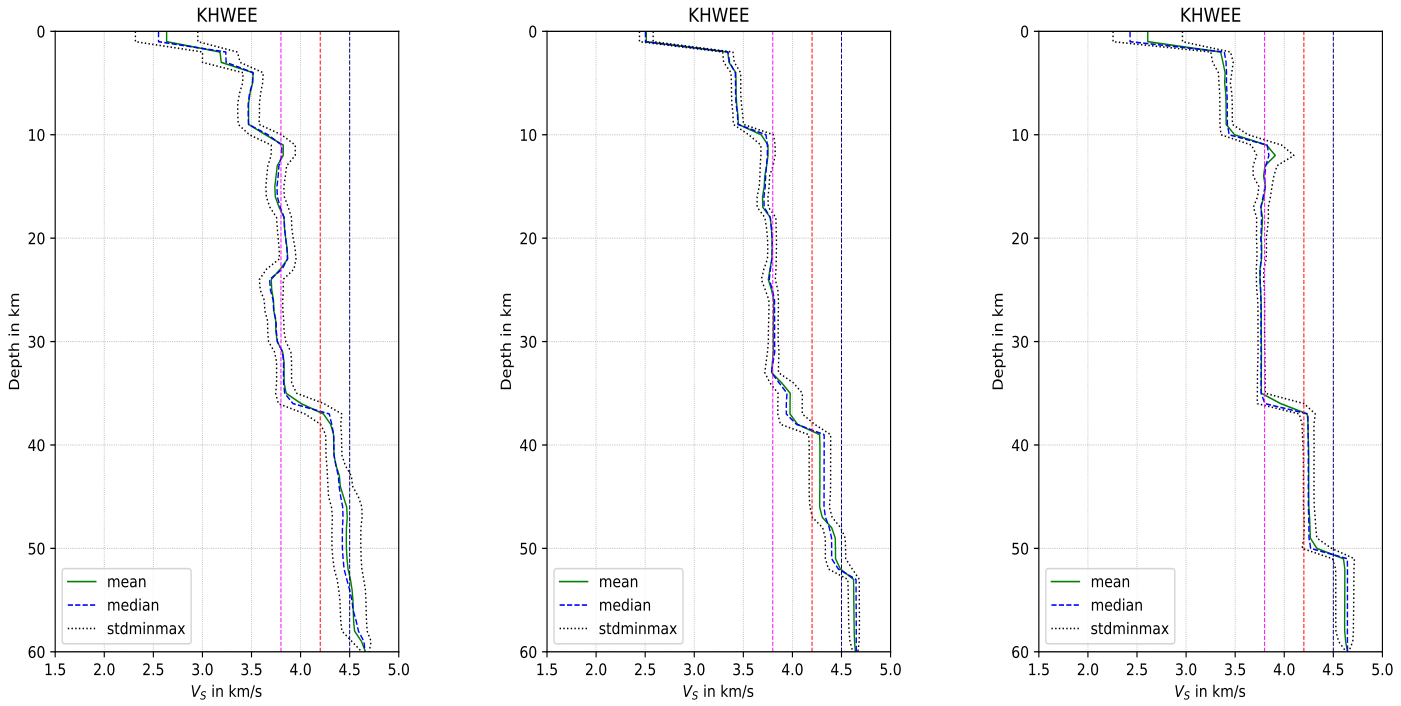


(a) Mean and median velocity models of inversion 1 at station KHWEE. The green line gives the mean velocity, the blue dashed line gives the median velocity and the dotted black lines give the standard deviation of the model. The events for the receiver function stack are given in table 17 (1 event).

(b) Mean and median velocity models of inversion 1 at station KHWEE. The green line gives the mean velocity, the blue dashed line gives the median velocity and the dotted black lines give the standard deviation of the model. The events for the receiver function stack are given in table 18 (3 events).

(c) Mean and median velocity models of inversion 1 at station KHWEE. The green line gives the mean velocity, the blue dashed line gives the median velocity and the dotted black lines give the standard deviation of the model. The events for the receiver function stack are given in table 19 (6 events).

Figure 62: 1D velocity models of the inversions at station KHWEE. The left panel shows the mean and median models as well as the standard deviation of the inversion with a receiver function stack with a slowness of 6.8 s/°. The middle panel shows the same for the inversion with a receiver function stack with a slowness of 7.0 s/°. The right panel shows the same for the inversion with a receiver function stack with a slowness of 7.5 s/°. The vertical lines in both panels give the 3.8 km/s, 4.2 km/s and 4.5 km/s thresholds.

## B.8 MREMI

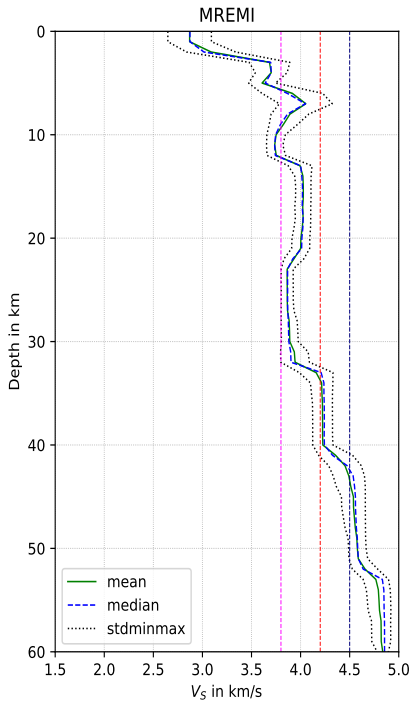


(a) Mean and median velocity models of inversion 1 at station MREMI. The green line gives the mean velocity, the blue dashed line gives the median velocity and the dotted black lines give the standard deviation of the model. The events for the receiver function stack are given in table 20 (2 events).

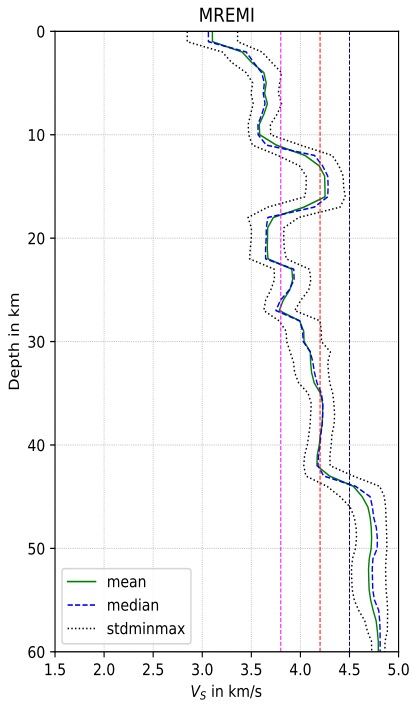


(b) Mean and median velocity models of inversion 1 at station MREMI. The green line gives the mean velocity, the blue dashed line gives the median velocity and the dotted black lines give the standard deviation of the model. The events for the receiver function stack are given in table 21 (2 events).

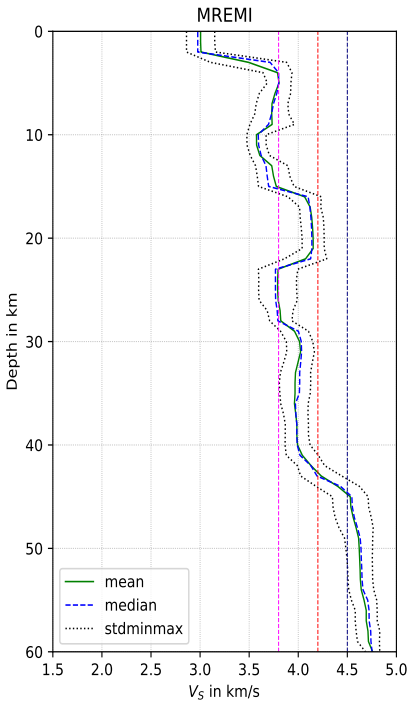


(c) Mean and median velocity models of inversion 1 at station MREMI. The green line gives the mean velocity, the blue dashed line gives the median velocity and the dotted black lines give the standard deviation of the model. The events for the receiver function stack are given in table 22 (5 events).

Figure 63: 1D velocity models of the inversions at station MREMI. The left panel shows the mean and median models as well as the standard deviation of the inversion with a receiver function stack with a slowness of 5.8 s/°. The middle panel shows the same for the inversion with a receiver function stack with a slowness of 6.8 s/°. The right panel shows the same for the inversion with a receiver function stack with a slowness of 7.4 s/°. The vertical lines in both panels give the 3.8 km/s, 4.2 km/s and 4.5 km/s thresholds.

## B.9 BROLN

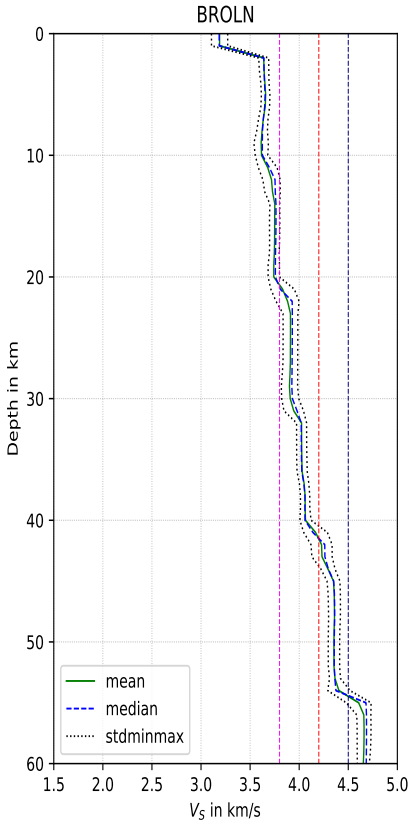


(a) Similar to figure 7b, the mean and median velocity models of inversion 1 at station BROLN. The events for the receiver function stack are given in table 23 (5 events).

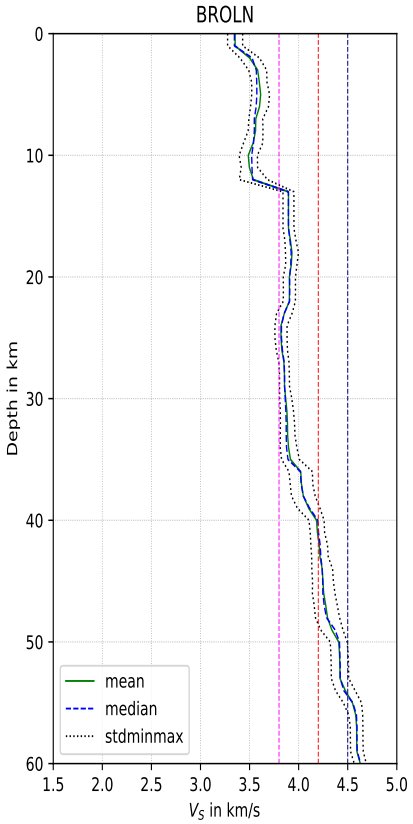


(b) Similar to figure 7b, the mean and median velocity models of inversion 1 at station BROLN. The events for the receiver function stack are given in table 24 (8 events).

Figure 64: 1D velocity models of the inversions at station BROLN. The left panel shows the mean and median models as well as the standard deviation of the inversion with a receiver function stack with a slowness of 6.2 s/°. The right panel shows the same for the inversion with a receiver function stack with a slowness of 7.3 s/°. The vertical lines in both panels give the 3.8 km/s, 4.2 km/s and 4.5 km/s thresholds.

## B.10 SOOWA

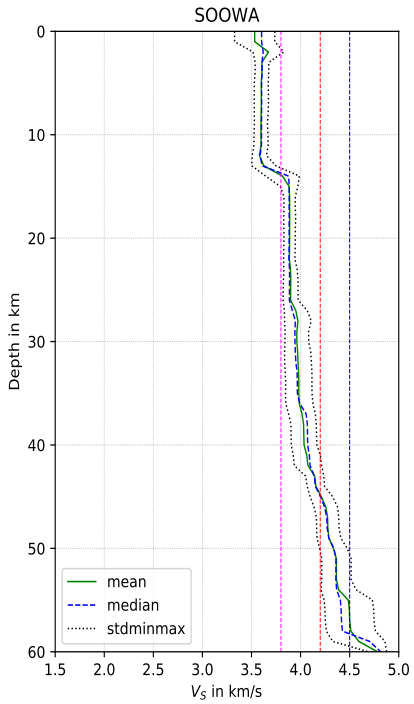


(a) Mean and median velocity models of inversion 1 at station SOOWA. The green line gives the mean velocity, the blue dashed line gives the median velocity and the dotted black lines give the standard deviation of the model. The events for the receiver function stack are given in table 25 (4 events).

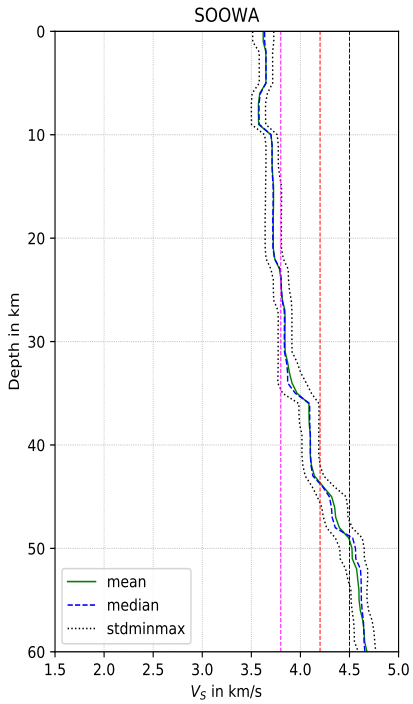


(b) Mean and median velocity models of inversion 1 at station SOOWA. The green line gives the mean velocity, the blue dashed line gives the median velocity and the dotted black lines give the standard deviation of the model. The events for the receiver function stack are given in table 26 (2 events).

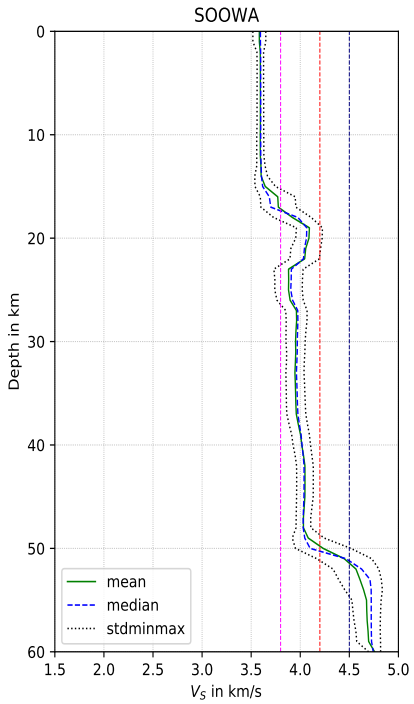


(c) Mean and median velocity models of inversion 1 at station SOOWA. The green line gives the mean velocity, the blue dashed line gives the median velocity and the dotted black lines give the standard deviation of the model. The events for the receiver function stack are given in table 27 (2 events).

Figure 65: 1D velocity models of the inversions at station SOOWA. The left panel shows the mean and median models as well as the standard deviation of the inversion with a receiver function stack with a slowness of 5.9 s/°. The middle panel shows the same for the inversion with a receiver function stack with a slowness of 7.3 s/°. The right panel shows the same for the inversion with a receiver function stack with a slowness of 7.7 s/°. The vertical lines in both panels give the 3.8 km/s, 4.2 km/s and 4.5 km/s thresholds.

## B.11 LKGWB

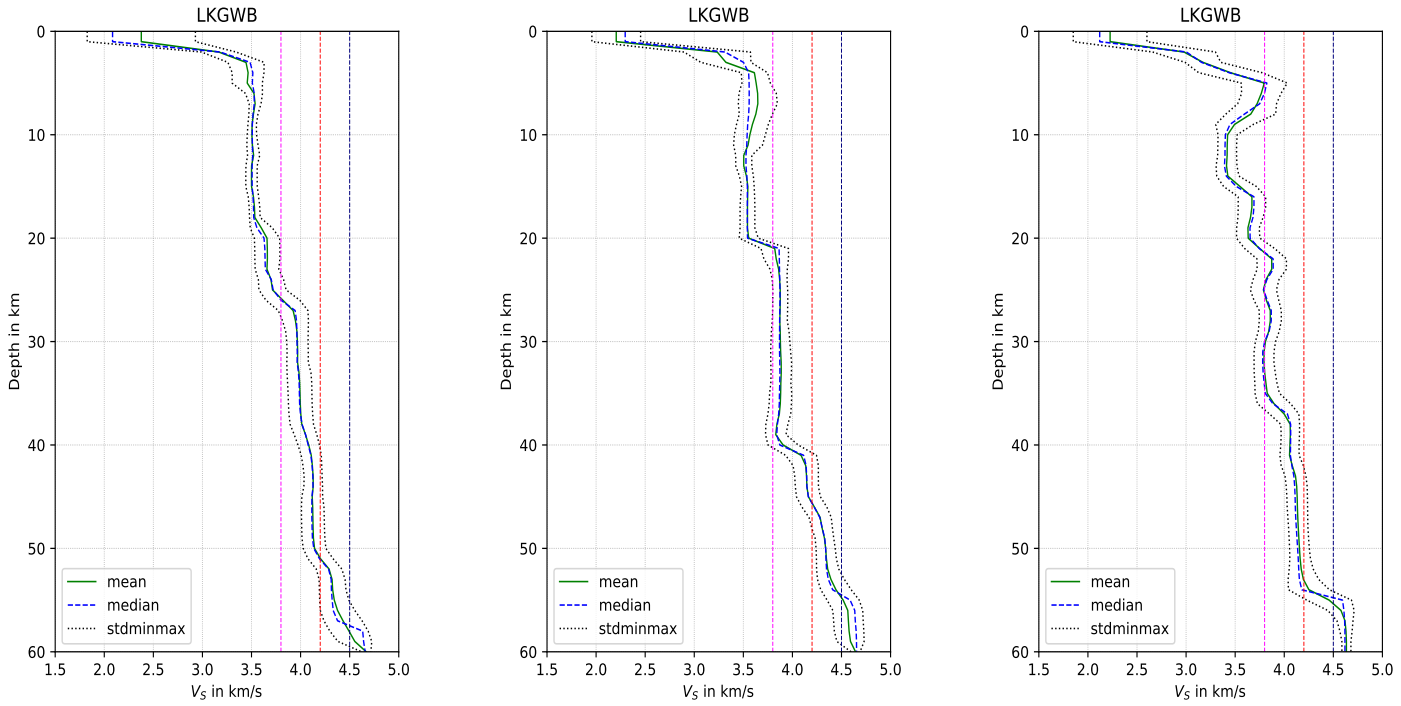


(a) Mean and median velocity models of inversion 1 at station LKGWB. The green line gives the mean velocity, the blue dashed line gives the median velocity and the dotted black lines give the standard deviation of the model. The events for the receiver function stack are given in table 28 (1 event).

(b) Mean and median velocity models of inversion 1 at station LKGWB. The green line gives the mean velocity, the blue dashed line gives the median velocity and the dotted black lines give the standard deviation of the model. The events for the receiver function stack are given in table 29 (1 event).

(c) Mean and median velocity models of inversion 1 at station LKGWB. The green line gives the mean velocity, the blue dashed line gives the median velocity and the dotted black lines give the standard deviation of the model. The events for the receiver function stack are given in table 30 (2 events).

Figure 66: 1D velocity models of the inversions at station LKGWB. The left panel shows the mean and median models as well as the standard deviation of the inversion with a receiver function stack with a slowness of 5.6 s/° with a receiver function from the east. The middle panel shows the same for the inversion with a receiver function stack with a slowness of 5.6 s/° with a receiver function from the southwest. The right panel shows the same for the inversion with a receiver function stack with a slowness of 7.8 s/°. The vertical lines in both panels give the 3.8 km/s, 4.2 km/s and 4.5 km/s thresholds.

## B.12 KOOLE

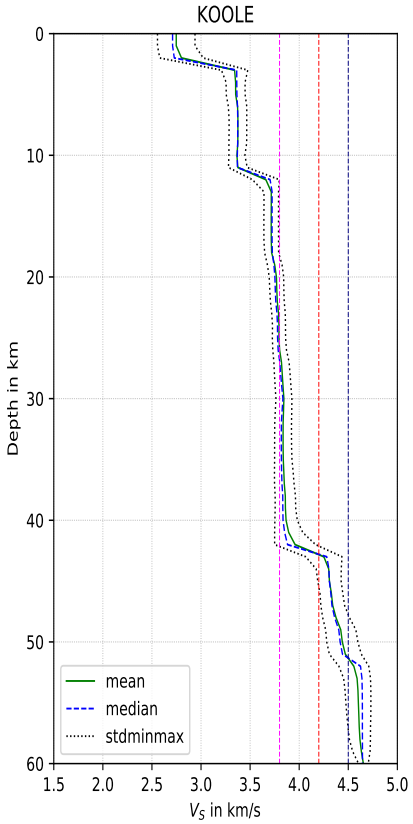


(a) Similar to figure 7b, the mean and median velocity models of inversion 1 at station KOOLE. The events for the receiver function stack are given in table 31 (3 events).

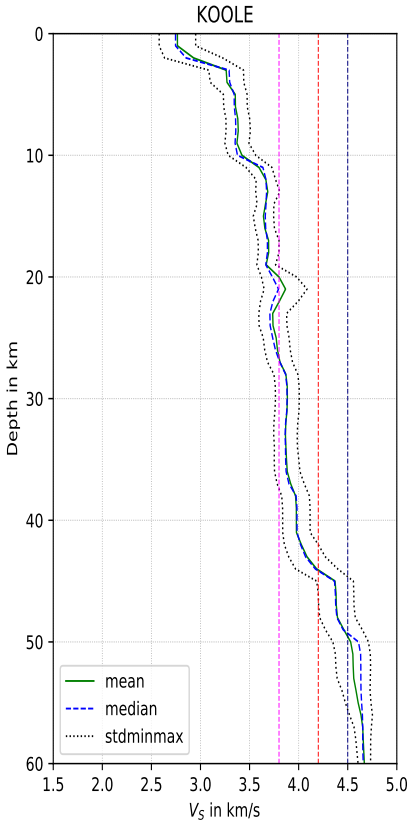


(b) Similar to figure 7b, the mean and median velocity models of inversion 1 at station KOOLE. The events for the receiver function stack are given in table 32 (5 events).

Figure 67: 1D velocity models of the inversions at station KOOLE. The left panel shows the mean and median models as well as the standard deviation of the inversion with a receiver function stack with a slowness of 6.7 s/°. The right panel shows the same for the inversion with a receiver function stack with a slowness of 7.7 s/°. The vertical lines in both panels give the 3.8 km/s, 4.2 km/s and 4.5 km/s thresholds.

## B.13 KSANE

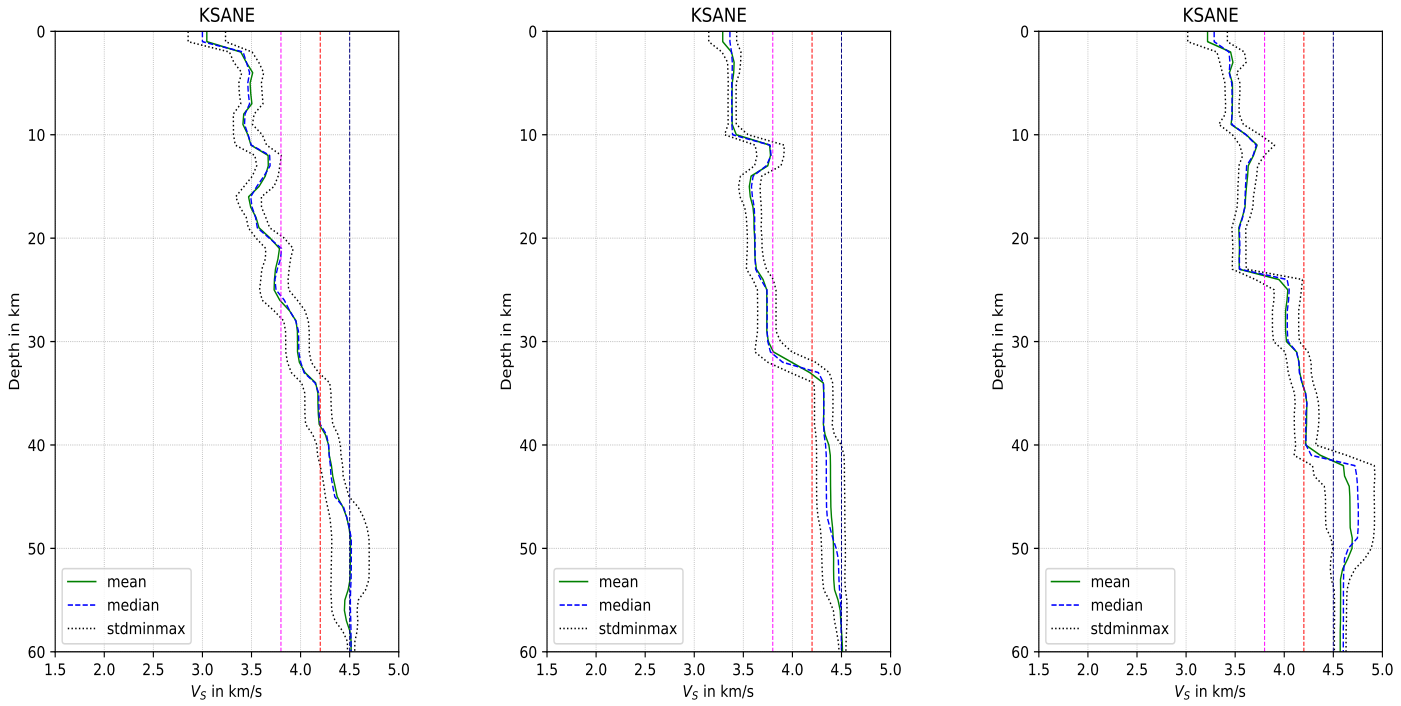


(a) Mean and median velocity models of inversion 1 at station KSANE. The green line gives the mean velocity, the blue dashed line gives the median velocity and the dotted black lines give the standard deviation of the model. The events for the receiver function stack are given in table 33 (2 events).

(b) Mean and median velocity models of inversion 1 at station KSANE. The green line gives the mean velocity, the blue dashed line gives the median velocity and the dotted black lines give the standard deviation of the model. The events for the receiver function stack are given in table 34 (2 event).

(c) Mean and median velocity models of inversion 1 at station KSANE. The green line gives the mean velocity, the blue dashed line gives the median velocity and the dotted black lines give the standard deviation of the model. The events for the receiver function stack are given in table 35 (3 events).

Figure 68: 1D velocity models of the inversions at station KSANE. The left panel shows the mean and median models as well as the standard deviation of the inversion with a receiver function stack with a slowness of 7.1 s/° with a receiver function from the east. The middle panel shows the same for the inversion with a receiver function stack with a slowness of 7.1 s/° with a receiver function from the southwest. The right panel shows the same for the inversion with a receiver function stack with a slowness of 7.3 s/°. The vertical lines in both panels give the 3.8 km/s, 4.2 km/s and 4.5 km/s thresholds.

## B.14 CKGRV

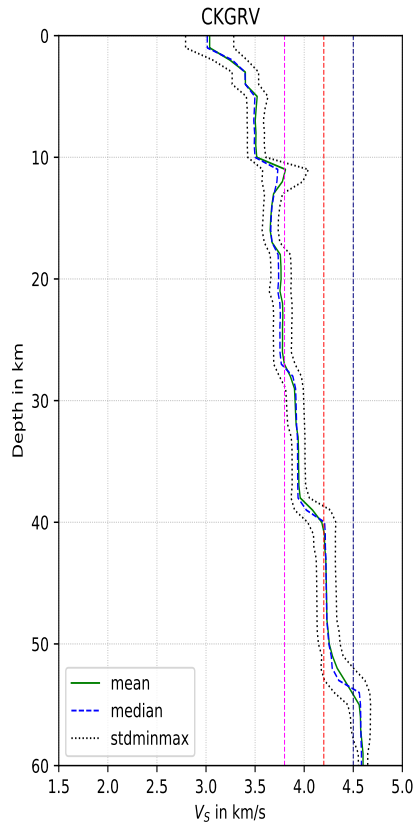


(a) Similar to figure 7b, the mean and median velocity models of inversion 1 at station CKGRV. The events for the receiver function stack are given in table 36 (3 events).

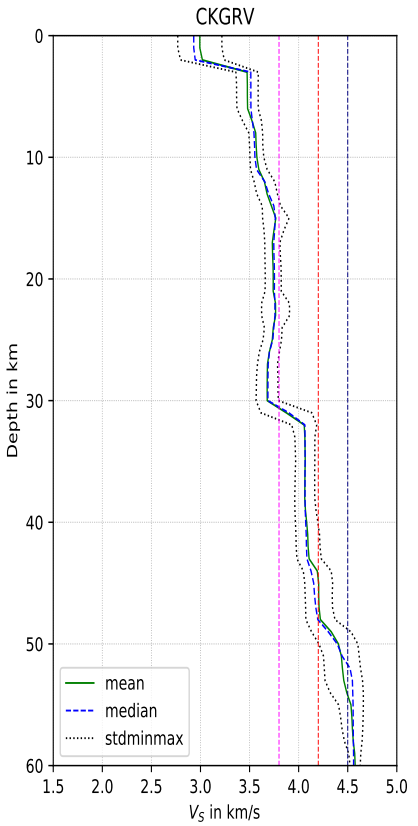


(b) Similar to figure 7b, the mean and median velocity models of inversion 1 at station CKGRV. The events for the receiver function stack are given in table 37 (5 events).

Figure 69: 1D velocity models of the inversions at station CKGRV. The left panel shows the mean and median models as well as the standard deviation of the inversion with a receiver function stack with a slowness of 5.7 s/°. The right panel shows the same for the inversion with a receiver function stack with a slowness of 7.4 s/°. The vertical lines in both panels give the 3.8 km/s, 4.2 km/s and 4.5 km/s thresholds.

## B.15 GRTLG

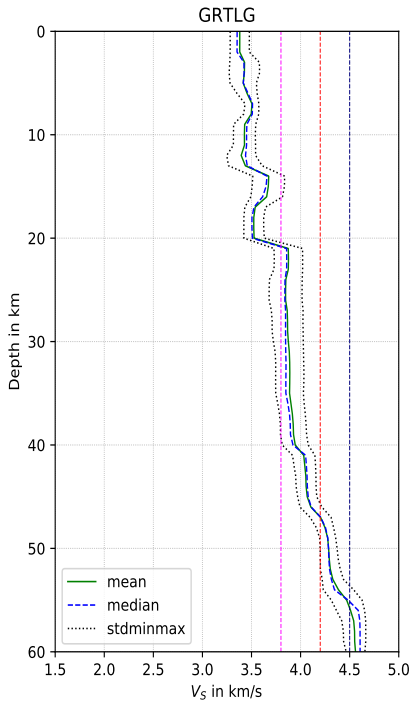


(a) Mean and median velocity models of inversion 1 at station GRTLG. The green line gives the mean velocity, the blue dashed line gives the median velocity and the dotted black lines give the standard deviation of the model. The events for the receiver function stack are given in table 38 (4 events).

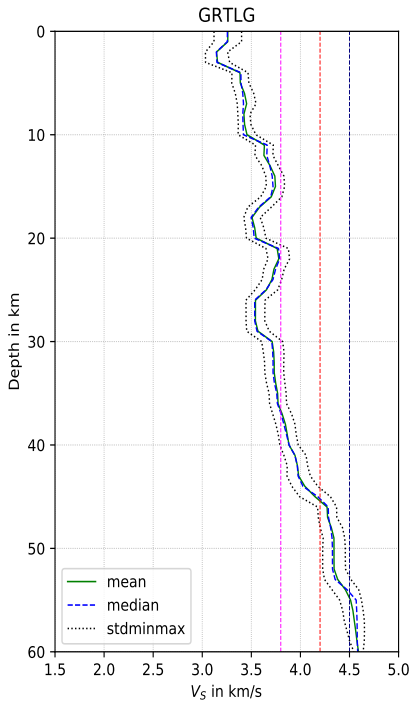


(b) Mean and median velocity models of inversion 1 at station GRTLG. The green line gives the mean velocity, the blue dashed line gives the median velocity and the dotted black lines give the standard deviation of the model. The events for the receiver function stack are given in table 39 (2 event).

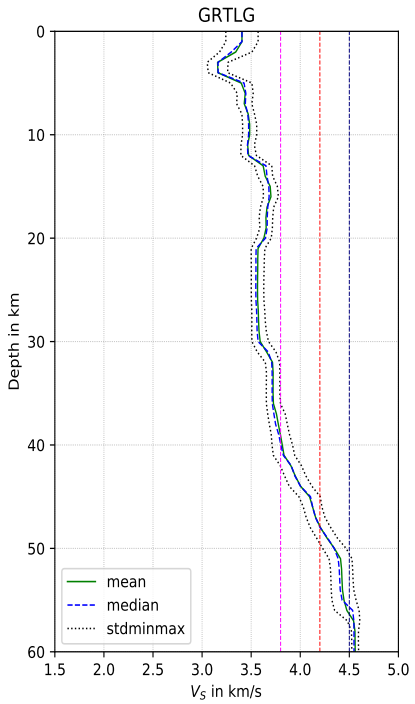


(c) Mean and median velocity models of inversion 1 at station GRTLG. The green line gives the mean velocity, the blue dashed line gives the median velocity and the dotted black lines give the standard deviation of the model. The events for the receiver function stack are given in table 40 (3 events).

Figure 70: 1D velocity models of the inversions at station GRTLG. The left panel shows the mean and median models as well as the standard deviation of the inversion with a receiver function stack with a slowness of 5.5 s/° with a receiver function from the east. The middle panel shows the same for the inversion with a receiver function stack with a slowness of 5.6 s/° with a receiver function from the southwest. The right panel shows the same for the inversion with a receiver function stack with a slowness of 6.9 s/°. The vertical lines in both panels give the 3.8 km/s, 4.2 km/s and 4.5 km/s thresholds.

## B.16 BTLPN

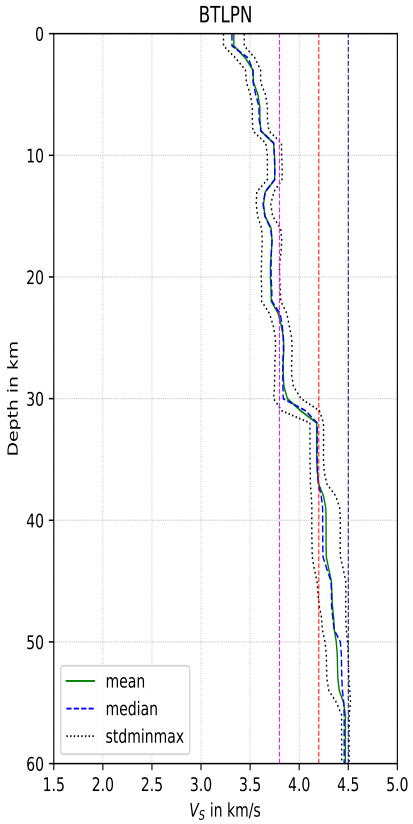


(a) Similar to figure 7b, the mean and median velocity models of inversion 1 at station BTLPN. The events for the receiver function stack are given in table 41 (2 events).

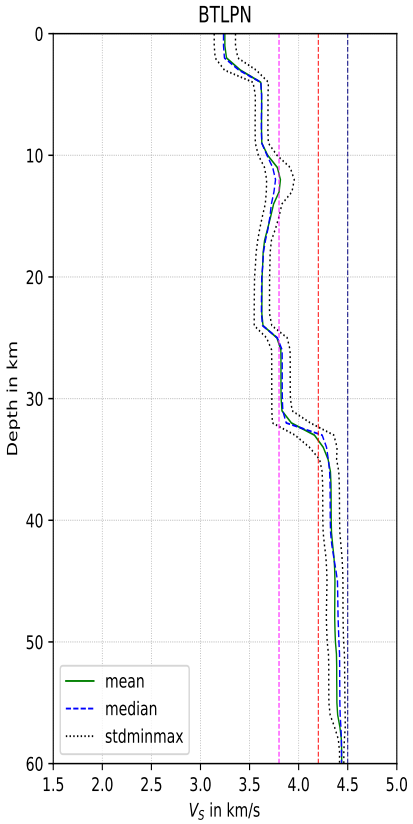


(b) Similar to figure 7b, the mean and median velocity models of inversion 1 at station BTLPN. The events for the receiver function stack are given in table 42 (3 events).

Figure 71: 1D velocity models of the inversions at station BTLPN. The left panel shows the mean and median models as well as the standard deviation of the inversion with a receiver function stack with a slowness of 5.9 s/°. The right panel shows the same for the inversion with a receiver function stack with a slowness of 7.2 s/°. The vertical lines in both panels give the 3.8 km/s, 4.2 km/s and 4.5 km/s thresholds.

## B.17 PHDHD

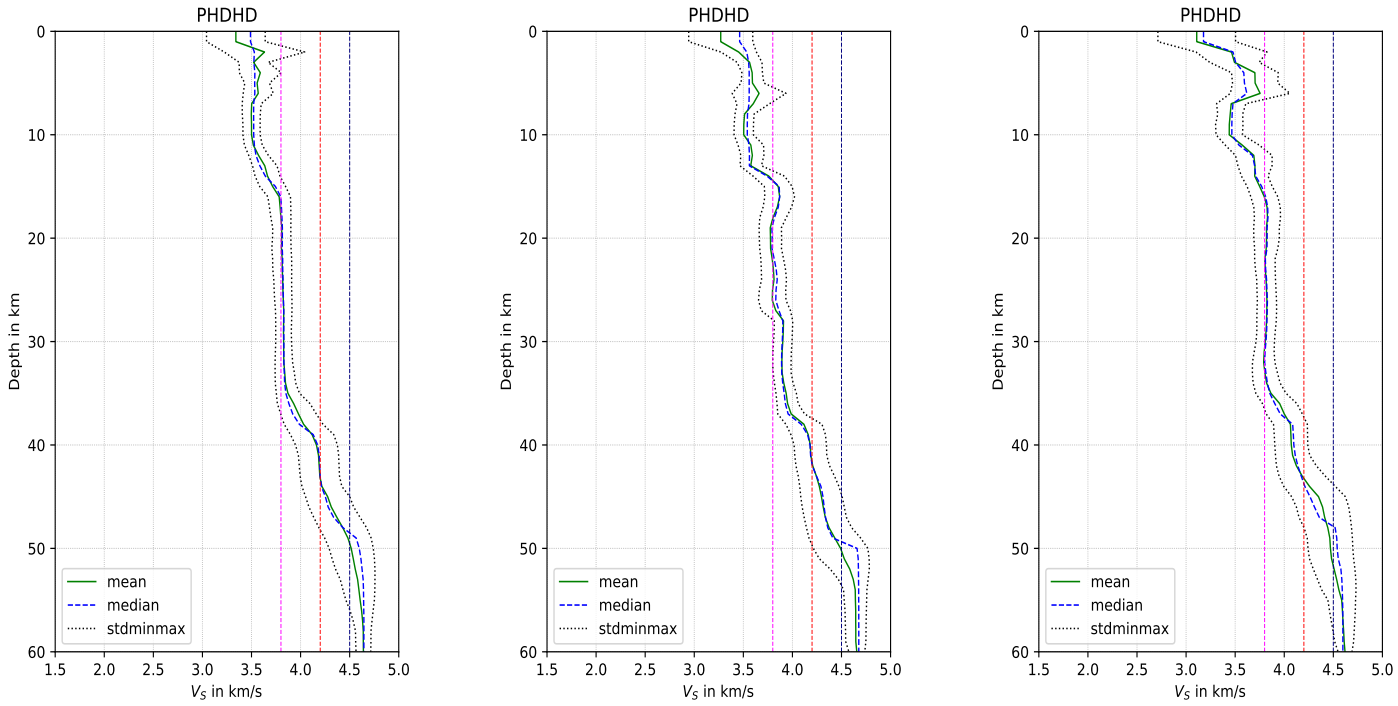


(a) Mean and median velocity models of inversion 1 at station PHDHD. The green line gives the mean velocity, the blue dashed line gives the median velocity and the dotted black lines give the standard deviation of the model. The events for the receiver function stack are given in table 43 (1 event).

(b) Mean and median velocity models of inversion 1 at station PHDHD. The green line gives the mean velocity, the blue dashed line gives the median velocity and the dotted black lines give the standard deviation of the model. The events for the receiver function stack are given in table 44 (2 events).

(c) Mean and median velocity models of inversion 1 at station PHDHD. The green line gives the mean velocity, the blue dashed line gives the median velocity and the dotted black lines give the standard deviation of the model. The events for the receiver function stack are given in table 45 (1 event).

Figure 72: 1D velocity models of the inversions at station PHDHD. The left panel shows the mean and median models as well as the standard deviation of the inversion with a receiver function stack with a slowness of 5.8s/° with a receiver function from the east. The middle panel shows the same for the inversion with a receiver function stack with a slowness of 7.0 s/° with a receiver function from the southwest. The right panel shows the same for the inversion with a receiver function stack with a slowness of 7.3 s/°. The vertical lines in both panels give the 3.8 km/s, 4.2 km/s and 4.5 km/s thresholds.

## B.18 SLIND

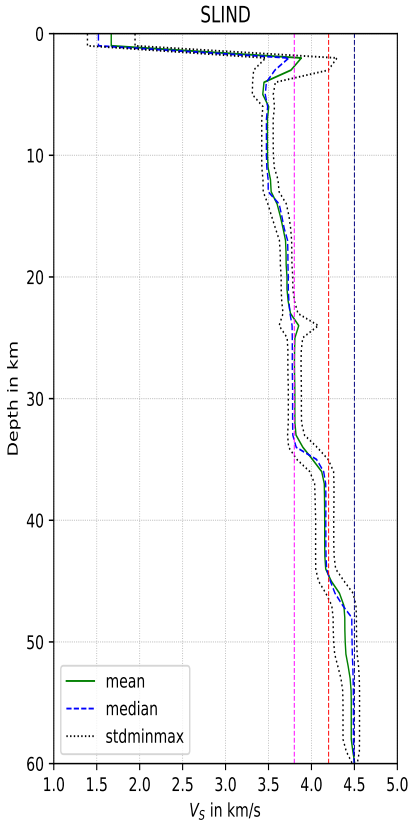


(a) Similar to figure 7b, the mean and median velocity models of inversion 1 at station SLIND. The events for the receiver function stack are given in table 46 (1 event).

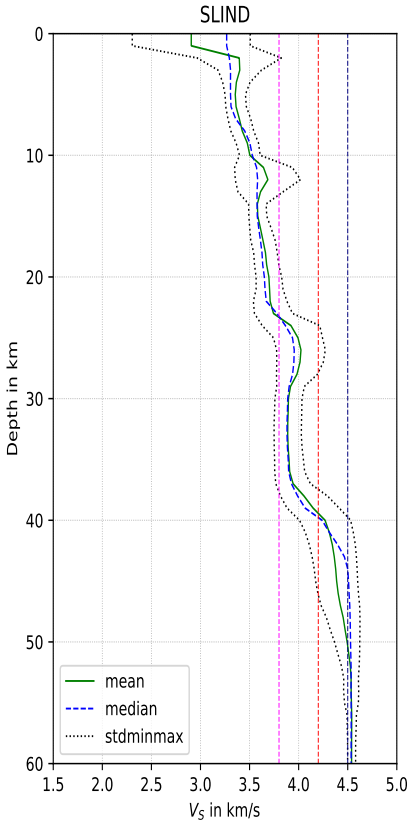


(b) Similar to figure 7b, the mean and median velocity models of inversion 1 at station SLIND. The events for the receiver function stack are given in table 47 (1 event).

Figure 73: 1D velocity models of the inversions at station SLIND. The left panel shows the mean and median models as well as the standard deviation of the inversion with a receiver function stack with a slowness of 7.1 s/°. The right panel shows the same for the inversion with a receiver function stack with a slowness of 7.7 s/°. The vertical lines in both panels give the 3.8 km/s, 4.2 km/s and 4.5 km/s thresholds.

## B.19 GMARE

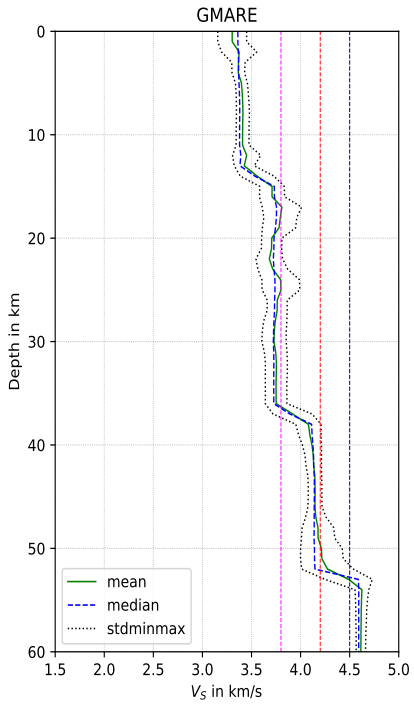


(a) Mean and median velocity models of inversion 1 at station GMARE. The green line gives the mean velocity, the blue dashed line gives the median velocity and the dotted black lines give the standard deviation of the model. The events for the receiver function stack are given in table 48 (1 event).

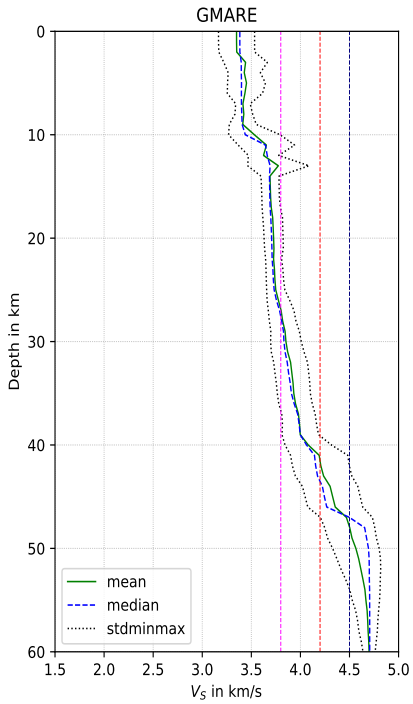


(b) Mean and median velocity models of inversion 1 at station GMARE. The green line gives the mean velocity, the blue dashed line gives the median velocity and the dotted black lines give the standard deviation of the model. The events for the receiver function stack are given in table 49 (1 event).

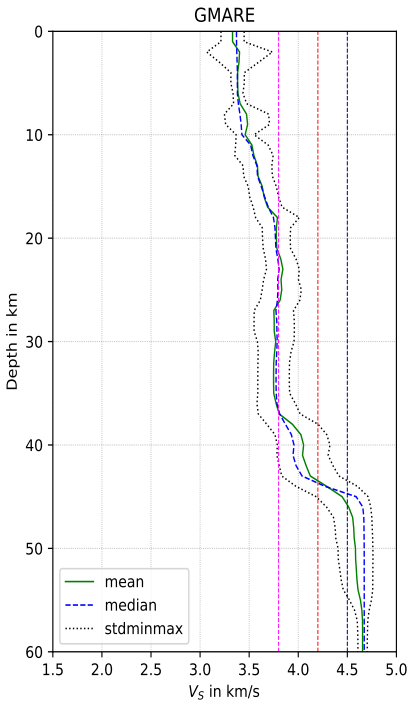


(c) Mean and median velocity models of inversion 1 at station GMARE. The green line gives the mean velocity, the blue dashed line gives the median velocity and the dotted black lines give the standard deviation of the model. The events for the receiver function stack are given in table 50 (1 event).

Figure 74: 1D velocity models of the inversions at station GMARE. The left panel shows the mean and median models as well as the standard deviation of the inversion with a receiver function stack with a slowness of 5.7s/° with a receiver function from the east. The middle panel shows the same for the inversion with a receiver function stack with a slowness of 7.3 s/° with a receiver function from the southwest. The right panel shows the same for the inversion with a receiver function stack with a slowness of 7.9 s/°. The vertical lines in both panels give the 3.8 km/s, 4.2 km/s and 4.5 km/s thresholds.

## B.20 XAUDM

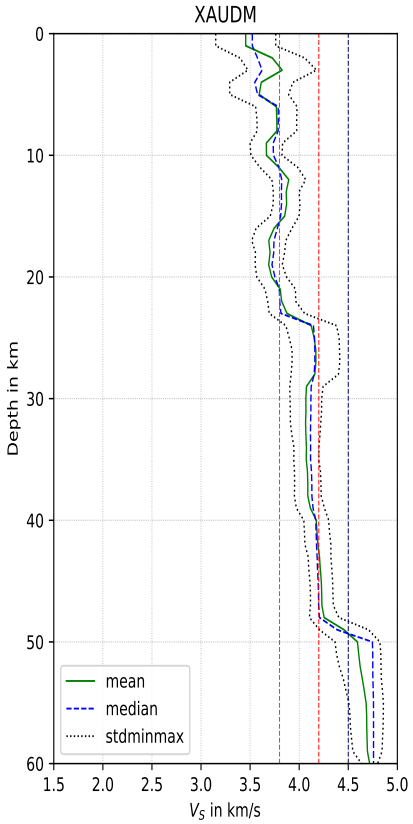


(a) Similar to figure 7b, the mean and median velocity models of inversion 1 at station XAUDM. The events for the receiver function stack are given in table 51 (4 events).

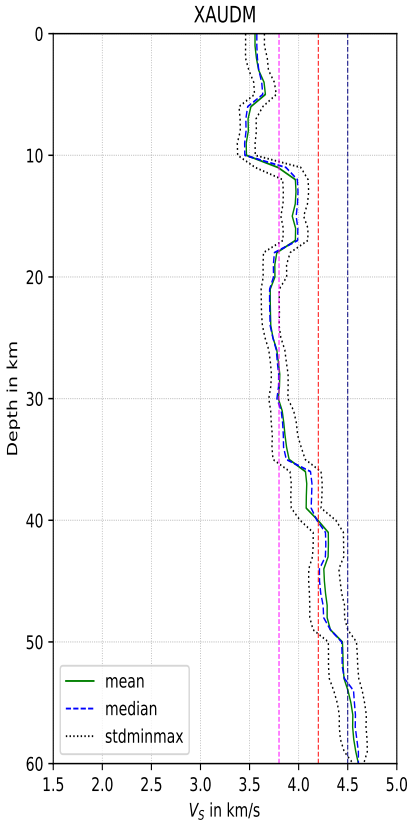


(b) Similar to figure 7b, the mean and median velocity models of inversion 1 at station XAUDM. The events for the receiver function stack are given in table 52 (3 events).

Figure 75: 1D velocity models of the inversions at station XAUDM. The left panel shows the mean and median models as well as the standard deviation of the inversion with a receiver function stack with a slowness of 5.8 s/°. The right panel shows the same for the inversion with a receiver function stack with a slowness of 7.4 s/°. The vertical lines in both panels give the 3.8 km/s, 4.2 km/s and 4.5 km/s thresholds.

## B.21 QNGWA

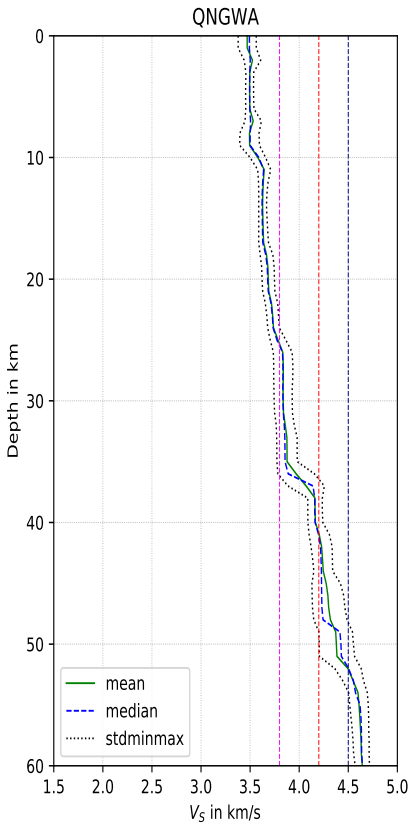


(a) Similar to figure 7b, the mean and median velocity models of inversion 1 at station QNGWA. The events for the receiver function stack are given in table 53 (2 events).

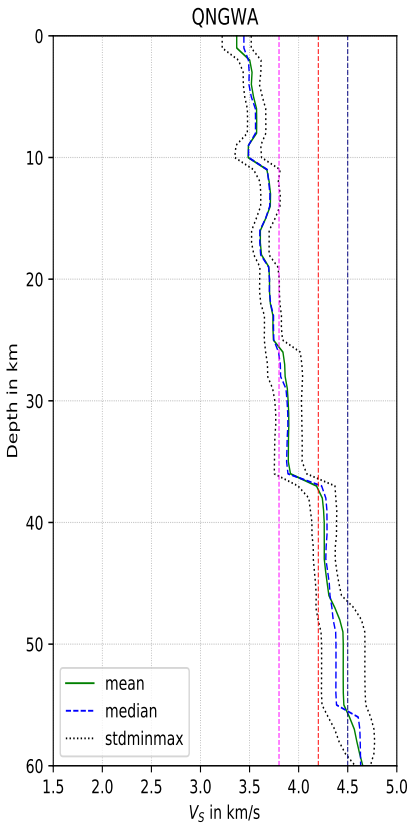


(b) Similar to figure 7b, the mean and median velocity models of inversion 1 at station QNGWA. The events for the receiver function stack are given in table 54 (6 event).

Figure 76: 1D velocity models of the inversions at station QNGWA. The left panel shows the mean and median models as well as the standard deviation of the inversion with a receiver function stack with a slowness of 5.8 s/°. The right panel shows the same for the inversion with a receiver function stack with a slowness of 7.5 s/°. The vertical lines in both panels give the 3.8 km/s, 4.2 km/s and 4.5 km/s thresholds.